NASA CR-165351
SRD-81-083

THERMAL-BARRIER-COATED TURBINE BLADE STUDY

(NASA-CR-165351) THERMAL-BARRIER-COATED TURBINE BLADE STUDY Final Report (General Electric Co.) 134 p HC A07/MF A01 CSCL 21E
N82-10040
Unclas
G3/07 27700

by P.A. Siemers and W.B. Hillig

GENERAL ELECTRIC COMPANY
Corporate Research and Development
Schenectady, New York 12301

NOV 1981
RECEIVED
NASA STI FACILITY
ACCESS DEPT.

prepared for

NATIONAL AERONAUTICS AND SPACE ADMINISTRATION

NASA-Lewis Research Center
Contract NAS3-21727

FOREWORD

This work was only possible through the able contriubtions of many individuals. At the Research and Development Center of the General Electric Company, R. L. Mehan conducted the mechanical properties, and S. F. Rutkowski carried out much of the specimen and blade coating and preparation, as well as assisting with the furnace testing. At the Company's Aircraft Engine Group, A. P. Sterman,[+] C. H. Gay, W. S. Westlake all contributed to the analysis and design efforts, and E. C. Duderstadt and S. Nunn carried out the rig and engine tests including the associated structural studies. The thermal diffusivity measurements were performed by J. Bueche and J. Hansen of the Re-entry Systems Division of the Company. In addition, the cooperation and counsel of E. Habesch, M. R. Jackson, and J. R. Rairden of this laboratory are gratefully acknowledged.

[+] Deceased

CONTENTS

PRECEDING PAGE BLANK NOT FILMED

LIST OF TABLES

LIST OF FIGURES

Figure Page

1.0 SUMMARY

Process and material development work and rig evaluations were undertaken to determine the effects of the bond coating deposition process, bond coating composition, ceramic coating composition, ceramic thickness, and substrate composition on the durability of thermal barrier coatings (TBCs). Cyclic furnace tests and rig exposure tests were used to quantify the effect of each coating variation on the lifetimes of TBCs. The relative rankings of the coating variations investigated are shown in Figure 1. The most durable combination of TBC variations investigated was an 8 w/o Y_2O_3-ZrO_2 ceramic layer deposited by an air plasma spray process over a Ni-22Cr-10Al-1Y bonding layer deposited by a low pressure plasma spray process.

Physical and mechanical properties were determined for the coated material system as well as for both free-standing NiCrAlY and ceramic. The free-standing ceramic strain-to-fail was determined to be about 0.071% which is in contrast to compressive and tensile strain-to-fail of about 0.78% and 1.4%, respectively, for a ceramic coating bonded to a metal substrate. The cohesive strength of the free standing ceramic material as determined by four point bend tests is about 33.0 MN/m^2 (4.79 ksi) which is close to the measured bond strength of 36.5 MN/m^2 (5.29 ksi) at the NiCrAlY-ceramic interface. The mechanical property determinations suggest that TBCs are not limited by mechanical stresses per se but rather by degradation of the adhesive strength by environmental interactions.

A parametric analysis was made of the effects of applying the thermal barrier coating to CF6-50 stage 2 high pressure turbine blades. The computer analysis examined the resultant changes in the mean bulk temperature, cooling air requirements, and blade rupture and low-cycle fatigue life. With a thermal barrier coating, the cooling flow to this blade could be reduced to about 50% of the original value, while maintaining the bulk metal temperature of the uncoated airfoil as shown in Figure 2. This reduced flow also maintains low-cycle fatigue and creep rupture life. However, the model predicted that local spallation of TBC from the leading and trailing edges of a fully coated blade could reduce the low-cycle fatigue life 30% below that of an uncoated blade. An advanced blade concept was developed which would derive maximum benefit of TBC in terms of reduced airfoil air cooling flow, and would limit the TBC bond coating temperature to below an assumed design temperature limit of 982°C (1800°F). This new blade design calls for an airfoil fully coated with a TBC except at the trailing edge region. The required redistribution of the cooling air assumes a reliable TBC system.

Twenty engine quality CF6-50 stage 2 high pressure turbine blades shown in Figure 3 were coated with TBC. Engine qualification testing showed that the high cycle fatigue life of the coated blades was about 13% lower than the mean value of uncoated blades. Six blades were engine tested for 626 15-minute endurance cycles. The engine tests proved that the TBC could remain adherent in an engine environment; however, the relative lack of ability of the TBC to resist foreign object damage was identified as a possible limitation to the implementation of TBCs on high pressure turbine blades.

2.0 INTRODUCTION

For the past two decades aircraft jet engine turbine inlet temperatures have been continually increased to improve engine efficiency and aircraft thrust-to-weight ratios. These higher inlet temperatures have been the driving force for the development of higher temperature blading alloys and improved environmental coating compositions and processes. One of the more recent advances in coating technology has been the development of thermal barrier coatings which can provide both thermal and oxidation protection to air cooled aircraft gas turbine hot-section components.

A thermal barrier coating (TBC) is a surface layer of a low thermal conductivity material applied to the hot side of a cooled metal structure to lower the temperature of the metal. Alternatively, the insulative coating could maintain the substrate at a desired temperature with less cooling. Oxides have generally been considered as prime thermal barrier candidates because of their chemical stability, relatively low thermal conductivity, and high temperature capability. Stabilized zirconium oxide has been identified as a successful oxide candidate. It has been demonstrated that the adhesion of the oxide layer can be substantially improved if an intermediate bonding layer is applied between the oxide and substrate. Historically, MCrAlY (where M = Ni, Co, Fe or combinations of these elements) bonding layers have been found to be most successful, primarily because of their excellent oxidation resistance at superalloy use temperatures. The ZrO_2 and MCrAlY-bond coatings have been identified as the choice for TBCs.

Plasma spray processing has historically been the most successful technique for the deposition of the coatings. Plasma spraying is a process in which a high-intensity direct current arc heats and ionizes plasma gases (N_2, Ar, He, H_2) that are expanded through a nozzle to form a high-temperature jet. Powder particles suspended in an inert carrier gas are injected into the high-temperature jet where they are entrained in the flow, melted, and propelled to a substrate where they subsequently impact and solidify. For some plasma spray systems the arc jet is expanded in air, and for other systems the jet is expanded into a low-pressure (40 torr) inert environment provided by a vacuum chamber. In the latter case, metallic deposits have been found to be more dense and more free of oxide than deposits made in air.

Past work has focused primarily on the effects of bond-coating composition and ceramic composition on the cyclic lifetimes of TBCs. Studies(1) have evaluated TBC durability with cyclic furnace tests, burner rig tests, high velocity rig tests as well as research engine tests.[2] Analytical studies have indicated the potential benefits of applying TBCs to combustors, blades, and vanes. At present the primary barrier to the implementation of TBCs in aircraft engines is inadequate confidence in the coatings, largely because of the inability to predict their failure as a function of time, temperature, and strain range.

Accordingly, the objectives of this program were to develop material compositions, process, and design guidelines to establish the technical feasibility of using thermal barrier coatings advantageously on high-pressure turbine aircraft engine blades. This feasibility would be established on the basis of materials and process screening studies, rig exposure tests, thermal and stress analyses, and parametric trade-off studies. Figure 4 is a flow diagram of the program, which consisted of three parallel efforts in materials/process development, mechanical properties evaluation, and analysis/design.

The materials/process development effort began with a series of screening studies which evaluated the effect of bond-coat composition, bond-coat processing technique, ceramic composition, substrate composition, ceramic thickness, and bond-coat pretreatment on the lifetimes of TBCs. The durability of the TBC variations investigated were evaluated with a cyclic furnace test, and the coatings were characterized using a microstructural evaluation, x-ray diffraction, and electron microprobe. The three best combinations of TBC variations were further evaluated in hot-corrosion and oxidation rig tests to determine the single best coating combination. Finally, techniques for the coating of blades were developed and evaluated.

The physical and mechanical property measurements constituted another major block of work. Measurements included Young's modulus, compressive/tensile strain-to-fail, adhesive strength, thermal conductivity, and thermal expansivity measurements of the various constituent coating systems. The physical/mechanical property determinations provided a starting point for the analysis/design efforts.

The analytical design study was performed on a CF6-50 stage 2 high-pressure turbine blade even though stage 1 blades would probably benefit more from a TBC because they are subjected to higher heat fluxes. The stage 2 blade has the advantage of a larger size (~4 in. airfoil length versus ~2 in. airfoil length), and a less complex cooling geometry (stage 2 blades do not have film cooling holes on the airfoil surface). By introducing the best available values for the physical and mechanical properties, heat transfer and stress analyses of the blade with and without a TBC were performed. From these analyses life predictions were made. These data provided the basis for evaluating the payoffs of TBCs and for designing a modified blade which incorporates the new data on mechanical properties and composition/process development.

The three parallel program efforts culminated with the coating of blades, and finally with the engine testing of the coated blades.

3.0 MATERIALS DEVELOPMENT AND CHARACTERIZATION

At the start of this materials study it was known that a NiCrAlY bonding layer applied over the structural metal substrate is a key factor to the success of the TBC system, and that its composition and method of application are important variables. Similarly, the composition and structure of the thermally insulating ZrO_2 solid solutions are also important. There was concern over the magnitude of the thermal expansion mismatches and expected resultant stresses. Consequently, additional physical and mechanical property information was required by designers, especially with respect to strength, failure criteria and thermal properties.

Accordingly the efforts described in detail below were undertaken to identify effective plasma spray procedures for the metal and ceramic layers. Several oxide and NiCrAlY compositions, previously identified to be promising, were systematically compared, along with the procedures for their application. Laboratory furnace cycling to 1000°C and 1100°C followed by microstructural examination were used to identify the most promising combinations. These selected combinations were then further studied in rigs that more closely simulated aircraft engine oxidation conditions, and that could provide an indication of hot corrosion performance. Representative mechanical and physical properties were determined to provide engineering and design information.

3.1 Plasma Spray Process

Two plasma spray processing techniques were evaluated in these studies. One process was performed in air, and the low pressure high velocity (LP/HV) process was performed in a reduced-pressure inert environment.

A Metco 3MB plasma spray gun was used for depositing ceramics and metal-bond coatings in air. However, prior to coating by either plasma spray process, metal substrates were routinely grit-blasted with 60 mesh pure white Al_2O_3 at a pressure of 40 psi. The substrates were then degreased and ultrasonically cleaned in a freon solvent to remove any embedded grit. The air process utilized argon as a primary gas and hydrogen as a secondary gas. Typical gun operating conditions for depositing ceramic and NiCrAlY coatings were:

Volts-52
Amperes-550
Primary Gas-Argon 150 SCFH at 95 psi

Secondary Gas-H_2 15 SCFH at 55 psi
Powder Carrier Gas-Argon 25 SCFH
NiCrAlY Feed Rate-700 g/h
Ceramic Feed Rate-1,250 g/h

Gun-to-substrate distances during coating deposition were maintained at about 7 to 10 cm for Y_2O_3-ZrO_2 coatings, 11 to 14 cm for MgO-ZrO_2 coatings, and 11 to 14 cm for NiCrAlY coatings. A plasma spray powder size of -200 + 325 mesh sizing (44-74 µm diameter) was used for the air process.

The LP/HV plasma spray system was obtained from Electro Plasma, Inc, (EPI) and used argon as a primary gas and helium as a secondary gas. Only NiCrAlY coatings could be successfully applied with the LP/HV process; ceramic coatings were found to have poor adhesion. Typically, the plasma gun was operated at 1300 amperes and 55 volts at a residual pressure of 50 torr and a gun-to-substrate distance of about 32 cm. Prior to coating, the substrate was preheated to about 800-900 °C by passing the arc over the substrate repeatedly. Reverse transfer arc treatment was used to remove possible residual oxides on the substrate surface. Plasma spray powders used in the LP/HV system had a sizing of -400 mesh.

3.2 Physical Property Determination

Mechanical and thermal measurements were made on the oxide layer, the NiCrAlY bond-coat layer, and on TBC material combinations primarily to provide input information for the analytical studies. Accordingly, the intent was to obtain representative information, rather than comprehensive data, early in the program which would include the property dependence on temperature, composition, geometry, and processing variables.

The mechanical measurements consisted of bend-strength measurements on free-standing plasma-sprayed 24 w/o MgO-ZrO_2 material, and on the same oxide when applied to a NiCrAlY-coated Hastelloy X base. In the latter case acoustic emission observations were also made. The thermal expansivity of each of two bond-coat alloys was determined over the range from room temperature to 1100 °C. (Other data for the structural alloys and for the oxide coating materials was available from previous work.) Finally, the thermal diffusivity and the derived thermal conductivity of plasma-sprayed 8 w/o Y_2O_3-ZrO_2 and 12 w/o Y_2O_3-ZrO_2 oxide layers were measured to 1100 °C. Adhesive strength of 12 w/o Y_2O_3-ZrO_2, plasma-sprayed onto the bond-coat/base metal combination was determined by a direct pulloff method. The Young's moduli of Ni-16Cr-6Al-0.5Y and of Ni-22Cr-10Al-1Y were measured at 20 °C. In the case of the latter alloy, these modulus measurements were extended up to 800 °C, and tensile strength determinations were performed over the range of 500 to 1100 °C in vacuum. The details of this work follow.

3.2.1 Flexural Strength of Oxide Coatings

These tests were all performed at 20 °C using a four-point bend configuration, having an inner span of 2.54 cm and an outer span of 5.08 cm. The oxide in all cases was 24 w/o $MgO-ZrO_2$ and was applied by the usual air process. However, in one test the oxide was free-standing and was built up on a copper substrate to a thickness of about 1.5 mm at which value the ceramic spalled as an intact sheet. For most tests the oxide was applied onto a Hastelloy X substrate which, in turn, had been coated previously with Ni-22Cr-10Al-1Y by the air plasma spray method. The thickness of the adherent oxide layers was of the order of 0.041 cm. The specimens were all about 2.54 cm wide. Most bend tests were monitored acoustically with an Enclevo 223C accelerometer at an 80 dB gain setting. In some tests strain gages were affixed to the TBC surface for monitoring the low-strain region of the deformation. Tests performed were of three types: (1) free-standing TBC (no substrate), (2) TBC on substrate in tension, and (3) TBC on substrate in compression.

(1) Free-standing $MgO-ZrO_2$. The average bend strength of free-standing 24 w/o $MgO-ZrO_2$ is 33.0 MN/m^2 (4.79 ksi) (average of two tests) and the elastic modulus is about 46.2 (6.70×10^6 psi) GN/m^2. Poisson's ratio has an extraordinarily low value of 0.076. There is also pseudo ductility present, as manifested by a nonlinear stress-strain curve as shown in Figure 5. It is believed these latter two phenomena are related; the TBC material can be considered a collection of weakly bonded cracked "tiles." The pseudo ductility is due to the cracks opening up, and the low Poisson's ratio is a manifestation of the material's difficulty in deforming laterally because the cracks can accommodate the deformation.

One further item of information can be gained from these free-standing tests (Figure 6). An appreciable amount of acoustic activity attributable to large scale crack growth indicates failure. As will be seen below, this is not the case when a substrate is present.

(2) $MgO-ZrO_2$ on substrate in tension. The most striking difference between the TBC on a substrate relative to the free-standing is that complete failure is not observed in tension. Rather, cracking is initiated in the

coating soon after the onset of plastic flow in the metal substrate. Several tests were conducted by unloading the specimen after acoustic emissions were detected. Generally, cracks were not visible when examined under a microscope until extensive cracking was measured by the acoustic emission system (Figure 7). Acoustic emissions were not detected in any appreciable amounts until the previous unloading point was reached. This is known as the Kaiser effect and is common to most materials loaded in a similar manner.

Strain values in the coating were estimated by measuring the radius of curvature. Because we are dealing with a composite beam composed of two materials with differing moduli, the simple equation, $\varepsilon = t/2p$, where ε is the strain, t the thickness, and p the radius of curvature, is not strictly applicable because the neutral axis is no longer at the center of the beam. A correction(3) can be made, and with typical material properties and dimensions the neutral axis differed by 15% from that obtained from a t/2 calculation.

Several low-strain regime tests were also conducted with strain gages affixed to the 24 w/o $MgO-ZrO_2$ (Poisson's ratio was not measured). One such test is shown in Figure 8; this specimen had been furnace cycled 50 times (5 min heat up to 1000 °C, 40 min hold at 1000°C, air blast cooled to 140 °C in 14 min). No difference in mechanical behavior was noted before and after thermal cycling. The stress was calculated as described in the above reference. This involved treating the material as a "T" beam, consisting of a lower (tension side) section 2.57 cm wide (the original specimen width) and 0.041 cm deep, and an upper section 12.9 cm wide and 0.173 cm deep. [The ratio of the two widths is the ratio of the respective moduli of the $MgO-ZrO_2$ and metal, taken as 41.3 and 207 GN/m^2 (6.0×10^6 and 30×10^6 psi), respectively.] The modulus calculated in this manner, 30.3 GN/m^2 (4.39×10^6 psi), is not considered unreasonable when material and dimensional uncertainties are considered. Two load-unload cycles were performed, and as in Figure 8 elastic behavior was observed up to the previous unloading point. This, of course, is expected for a system mechanically dominated by the metal. The measured strain to fail for the ceramic in tension was 1.4%. Failure occurs by pronounced open crack formation, but even then the TBC remains adherent.

(3) MgO-ZrO_2 on substrate in compression. When the TBC on the substrate was in compression, a strain on the order of 0.78% was required to cause failure in the TBC. As in the tension case, acoustic emission activity was detected prior to visually detecting a crack by load-unload tests. Failure, when it did occur, was catastrophic, with the TBC material shattering into small fragments.

The stress-strain behavior in compression, obtained in a similar manner to the tensile case and shown in Figure 9, showed the composite beam was stronger when the coating was in compression than when in tension. Moduli values were similar and within the limits of the accuracy of the calculation.

3.2.2 Ceramic/NiCrAlY Adhesion Strength

Tests to determine the adhesive strength of the bond between the ceramic and NiCrAlY bond coat were performed with aligned pull rods in an Instron machine. Small discs (earlier, small plates were used) 1.22 cm (0.480 in.) in diameter and 1.91 mm (0.075 in.) thick with a 0.38 mm (0.015 in.) layer of 12 w/o Y_2O_3-ZrO_2 were placed between the pull rods and bonded to them with a filled epoxy. The assembly was cured in place with a heat gun to accelerate the cure. After curing, the specimen was pulled to failure in tension.

Mixed-mode fractures occurred (part adhesive and cohesive). These types of fractures prevent a reliable estimate of the ceramic/bond coat adhesive strength. However, the results provide an estimate of the lower-limit strength of this interface, which is 36.5 MN/m^2 (5290 psi).

3.2.3 Mechanical Properties of NiCrAlY Bond Coat

A brief investigation of the mechanical properties of the NiCrAlY bond coat was conducted because of its importance in transferring load from the ceramic TBC to the metal substrate. About 3.2 mm of Ni-22Cr-10Al-1Y and Ni-16Cr-6Al-0.5Y alloys were deposited on 304L stainless steel by the LP/HV process. Mechanical test specimens were machined from the center of the NiCrAlY layers in the form of 3.2 mm x 3.2 mm x 38.1 mm bars for modulus determination. The room temperature elastic modulus was determined for both materials with an ultrasonic pulse echo technique, and the effect of temperature on the elastic modulus was studied for the Ni-22Cr-10Al-1Y bond coat. (The temperature-dependence of the Ni-16Cr-6Al-0.5Y bond coat is expected to be similiar.)

At room temperature the measured values of the elastic moduli were 198 GN/m^2 (28.7 x 10^6 psi) for the Ni-22Cr-10Al-1Y and 164 GN/m^2 (23.7 x 10^6 psi) for the Ni-16Cr-6Al-0.5Y materials. The elastic modulus as a function of temperature for the Ni-22Cr-10Al-1Y composition is shown in Figure 10. The inflection in the curve in the vicinity of 600 °C may be due to the formation of $CrNi_3$ which has been reported in the Cr-Ni-Al system.(4) Whatever the cause, a structural change, not detectable in the expansion data, apparently occurs in this alloy in the vicinity of 600 °C. Tests were terminated at 800 °C because of the excessive attenuation of the ultrasonic signal at higher temperature.

For the tensile strength measurements a relatively thick coating of NiCrAlY with the composition Ni-22Cr-10Al-1Y was sprayed onto a 304L stainless-steel substrate. Sub-size, pin-loaded, flat specimens were machined from the center of this coating. The specimens were 2.86 cm long, 1.59 mm thick, and had a gage length of 6.35 mm. A total of eight specimens were machined; two broke during grinding, and one broke during setup, so only five were finally tested. The specimens were vacuum annealed at 1100 °C, and tested in vacuum at a cross-head rate of 0.25 mm/min (0.01 in/min.), corresponding to an approximate strain rate of 4%/min.

Table I shows the data, and Figure 11 shows the yield strength and ductility plotted as a function of temperature. The rapid drop in strength and the increase in ductility may be related to the increased compositional range of the γ' NiAl phase which begins to occur at about 600 °C. At the use temperature of approximately 1000 °C, the coating in the as-deposited state is exceedingly ductile. These data, however, must be interpreted with caution because the interdiffusion of substrate, bond coat, and TBC constituents which have been shown to occur during long-time heat treatment at elevated temperature. This interdiffusion may affect the bond-coat properties, but it still is expected to behave in a very ductile manner. In any case, modeling its behavior in terms of a simple elastic stress analysis is inappropriate.

3.2.4 Thermal Expansivity of NiCrAlY

Thermal expansion measurements were made on Ni-22Cr-10Al-1Y bars deposited with the LP/HV process as described in section 3.2.3. The expansion was measured with a dilatometer between room temperature and 1100 °C fitted with alumina fixturing. A heating and cooling rate of 7 °C/min was used with a 10 min hold at 1100 °C. The NiCrAlY sample was a rectangular bar with

TABLE I

TENSILE TEST RESULTS AT ELEVATED TEMPERATURE ON Ni-22CR-10Al-1Y PLASMA SPRAYED BOND COAT AT A CROSS-HEAD SPEED OF 0.01 IN/MIN

Test Temperature (°C)	0.2% Yield Strength MPa (ksi)	Ultimate Tensile Strength MPa (ksi)	% Elongation 6.35 mm gage span	% Reduction in Area
500	1140 (165)	1160 (168)	0	0
600	915 (133)	960 (139)	0	0
750	270(39.3)	365(52.8)	34	51
900	49(7.13)	69(10.0)	275	∿100
1100*	16(2.35)	19(2.78)	252	∿100

*Inadvertently tested at 0.1 in/min for most of test.

nominal dimensions of 3.2 mm x 3.2 mm x 38.1 mm and was maintained at a constant compressive stress of 1.5×10^4 N/m^2. Figures 12 and 13 show the expansion behavior of the NiCrAlY samples studied during two successive runs. In the first run a net contraction of 0.4% of the sample length, attributable to sintering in the sample, was observed. This result is in agreement with the observation that porosity in the NiCrAlY decreased after furnace tests. In the second run additional contraction was observed. The average expansion coefficient for the alloy below 1000°C is about 13.8×10^{-6} $^oC^{-1}$ and the average expansion below 1200°C is about 18.3×10^{-6} $^oC^{-1}$. It is evident from Figure 13 that a reversible dimensional change of about 0.5% occurs in NiCrAlY about 1000°C.

If one refers to the NiCrAl phase diagram, the observed transformation in NiCrAlY probably corresponds to the transformation of a low-temperature $\gamma'+\alpha$ phase field to a $\gamma+\beta$ phase field at 1000 °C, where γ' is an ordered Ni_3Al face-centered cubic structure, α is α chromium, γ is a Ni solid solution alloyed with Cr and Al, and β is a NiAl phase alloyed with Cr.

3.2.5 Thermal Properties of Oxide Barrier Layer

Two test specimens each were prepared by air plasma-spraying 12 w/o Y_2O_3-ZrO_2 and 8 w/o Y_2O_3-ZrO_2. In the case of the former composition, samples were made both from commerical crushed and sieved material and from an experimental spray-dried material. The free standing ceramic samples had nominal dimensions of 12.7 mm diameter and 0.63 mm thickness.

Thermal diffusivities of the plasma sprayed ceramic materials were measured at GE's Thermal Physics and Chemistry Laboratory, Philadelphia, PA. The thermal conductivity is calculated from the diffusivity using the measured density and known specific heat.

The sample configuration required for these measurements is a thin disc of 12.5 mm in diameter. The thickness of the disc varied with the conductivity range of the material tested. The sample is heated at the center of a graphite tube furnace in an inert atmosphere. One side of the disc is heated with a pulse from a Nd-glass laser. The laser is an Apollo 35 which can deliver pulses up to 250 joules with pulse lengths between 0.1 and 1 ms. The temperature of the other side of the sample is monitored as a function of time with an intrinsic contact thermocouple at temperatures below 200°C and with a radiometric detector at temperatures above 200°C. This temperature versus time curve is displayed on an oscilloscope and photographed, and the diffusivity is calculated from this curve. If no corrections are necessary for radiation losses, the diffusivity α can be calculated directly from $t_{0.5}$. The latter quantity is the time required for the temperature of the backface to rise to one-half of the saturation value according to the following equation in which ΔX is the specimen thickness:

$$\alpha = 1.37\,(\Delta X)^2 / \pi^2\, t_{0.5}$$

When significant radiation loss occurs (high temperature and high emittances), additional data from the temperature versus the time curve are required for the diffusivity calculation.

To prevent transmission of the laser pulse through the material front face, that surface was opacified with a thin layer of graphite. Likewise, to prevent the radiometric backface temperature detectors from sensing radiation from the sample interior and front face, that surface was also coated with graphite.

The thermal diffusivity was obtained from two independent runs. A second run was made to confirm the validity of the measurements at the highest temperature of interest, 1100 °C. In the first run an attempt was made to obtain results at 1400 °C. However, in that run the graphite coating appeared to have been substantially lost, as if oxidation may have occurred, although the inertness of the gas should have precluded that possibility. Whatever the reason, examination of the data indicated that it occurred above 1100 °C. In the second run, which confirmed our analysis, the coating remained intact. The data at 1400 °C are not reported because they are considered to be unreliable. There is indication that densification occurred at this temperature.

Results of the thermal diffusivity and of density measurements made to compute the conductivity are summarized in Table II. In turn, the thermal conductivity λ of the ZrO_2 samples was calculated with the measured diffusivity α, the measured density ρ, and values of specific heat c_p, according to the equation:

$$\lambda = \alpha\, c_p\, \rho$$

The specific heat values were estimated with a weighted average of the specific heats of Y_2O_3 and ZrO_2 at the temperature of interest. Results are presented in Table III.

TABLE II

THERMAL DIFFUSIVITY DATA

Material	Density g/cm^3	Thermal Diffusivity (cm^2/sec)		
		400°C	800°C	1100°C
AEE 8 w/o Y_2O_3-ZrO_2	5.17	.00328	.00326	.00330
AEE 12 w/o Y_2O_3-ZrO_2	4.43	.00260	.00249	.00263
Spray Dried 12 w/o Y_2O_3-ZrO_2	4.52	.00255	.00228	.00259

TABLE III
CALCULATED THERMAL CONDUCTIVITY

TEMPERATURE (^{o}C)	400	800	1100
Thermal Conductivity (watts/cm ^{o}K):			
8 w/o Y_2O_3-ZrO_2	.00980	.01038	.01093
12 w/o Y_2O_3-ZrO_2	.00654	.00695	.00733
Spray Dried 12 w/o Y_2O_3-ZrO_2	.00660	.00706	.00744

3.3 Stability of TBC Systems Subjected to Thermal Cycling

The TBC systems are composites of alloys and metal oxides, containing two distinct interfaces (substrate/bond coating, bond coating/ceramic). The performance of such composites is strongly dependent upon the stability of the individual materials (i.e., microstructure, phase, composition) and upon the material interfaces. This section describes some of the degradation mechanisms observed in TBC systems after high-temperature exposure during the cyclic furnace testing.

3.3.1 Cyclic Furnace Tests

The thermal shock resistance of TBC systems was investigated with a cyclic furnace test. Samples were cyclically exposed in a CM1700 Rapid Temp$^{(TM)}$ furnace which is provided with a $MoSi_2$ heating element and with a microprocessor to obtain a controlled (reproducible) temperature cycle. Coated flat coupons were mounted in a slotted high-purity alumina firebrick located at the bottom of the furnace. For the first 500 cycles of testing the maximum temperature of the furnace cycle was 1000°C and for the remaining cycles was 1100°C. An hourly cycle consisted of a 5 min heat up to the maximum temperature followed by a 40 min hold. Then the power was turned off, and after a compressed air blast cooling from the top of the furnace for 14 min the substrate temperature dropped to 140 °C. Figure 14 shows the measured metal temperature response of a TBC specimen.

Figure 15 illustrates a typical coupon for cyclic furnace testing. The substrates had nominal dimensions of 3.2 cm x 2.0 cm x 0.16 cm. The substrates were coated on two sides, each side with a different TBC variation. Nominal NiCrAlY thickness was 0.13 cm, and the ceramic coating thicknesses were either 0.25 mm or 0.51 mm. The substrate edges were well-rounded but were left uncoated and exposed during the furnace testing. Table IV lists the average lifetimes of each coating variation subjected to the thermal cycling just described. Four samples of each variation were used in the computed averages (Table IV). Initiation of failure was defined as the cycle when failure, such as edge separation or cracking, was first noted. Complete failure was defined as 80% or more coating spallation. In the circumstance where one sample of a particular coating variation did not fail at the end of 658 cycles (test duration), the coating lifetime for initiation and completion of failure was arbitrarily set at 658 cycles for purposes of averaging. Table V and Figure 1 summarize the lifetime data of Table IV according to each specific type of variation.

TABLE IV

AVERAGE LIFETIMES OF TBC VARIATIONS DURING CYCLIC FURNACE TESTING

Substrate	NiCrAlY Composition	NiCrAlY Deposition Process	ZrO_2 Stabilizer Level	Ceramic Thickness (mm)	Initiation of Failure (cycles)	Complete Failure (cycles)
R80*	Ni-22Cr-10Al-1Y	Air	24 w/o MgO	0.51	357	401
R80	"	"	"	0.25	249	272
Hast-X*	"	"	"	0.51	310	352
R80	Ni-16Cr-6Al-0.5Y	"	"	0.51	143	184
R80	"	"	"	0.25	143	207
R80	Ni-22Cr-10Al-1Y	LP/HV	"	0.51	500	517
R80	"	"	"	0.25	354	394
Hast-X	"	"	"	0.51	272	316
Hast-X*	"	"	"	0.25	267	310
R80	Ni-16Cr-6Al-0.5Y	"	"	0.51	357	386
R80	"	"	"	0.25	249	386
R80	Ni-22Cr-10Al-1Y	LP/HV	12 w/o Y_2O_3	0.51	600	649
R80**	"	"	"	0.25	622	644
Hast-X*	"	"	"	0.51	489	518
Hast-X**	"	"	"	0.25	625	649
R80	Ni-16Cr-6Al-0.5Y	"	"	0.51	415	491
R80	"	"	"	0.25	494	517
R80	Ni-22Cr-10Al-1Y	LP/HV	8 w/o Y_2O_3	0.51	542	593
R80	"	"	"	0.25	593	624
Hast-X	"	"	"	0.51	293	350
Hast-X**	"	"	"	0.25	610	655
R80	Ni-16Cr-6Al-0.5Y	"	"	0.51	433	504
R80	"	"	"	0.25	505	574

*One specimen of four had a significantly shorter lifetime than the others.

**One specimen good after 658 hours.

Note: For the first 500 cycles the maximum temperature was 1000°C, and was 1100°C for the remaining 158 cycles.

Table V shows that NiCrAlY composition, NiCrAlY deposition process, and ceramic composition affected TBC lifetimes most strongly, and that substrate composition had less effect. The lifetime differences between ceramic thicknesses of 0.51 mm and 0.25 mm were almost negligible. Based on the summarized results in Table V, the two most durable coating systems were comprised of a Ni-22Cr-10Al-1Y coat applied by the LP/HV process with either an 8 or 12 w/o Y_2O_3-ZrO_2 ceramic coating. The 12 w/o Y_2O_3-ZrO_2 coatings yielded about a 4% greater lifetime that the 8 w/o Y_2O_3-ZrO_2 coatings, but the differences are not statistically significant.

3.3.2 Ceramic Coating Phase Stability

During the cyclic furnace tests samples were periodically taken for x-ray diffraction determination of the phases present in the ceramic coatings. Figure 16 shows that the relative phase content of the Y_2O_3-stabilized ZrO_2 remained constant at the temperatures investigated. In contrast, the MgO-stabilized ZrO_2 developed progressive destabilization with time at temperature. It is noteworthy that the partially stabilized plasma sprayed zirconias (8 w/o Y_2O_3-ZrO_2 and 24 w/o MgO-ZrO_2) in the as-deposited state are cubic but upon cycling become two-phase materials consisting of monoclinic and tetragonal modifications, whereas the fully stabilized 12 w/o Y_2O_3-ZrO_2 composition was single phase with a cubic structure.

3.3.3 Microscopic Evaluation

Micrographs were taken of each coating variation before and after cyclic furnace testing from which a pattern of failure emerged that involves the interdiffusion between the substrate and the NiCrAlY. Figure 17 contains micrographs before testing of 24 w/o MgO-ZrO_2 and 8 w/o Y_2O_3-ZrO_2 ceramic coatings applied over LP/HV-applied Ni-22Cr-10Al-1Y coatings. Some residual porosity was observed in the NiCrAlY coating, and at this stage little apparent interdiffusion was seen between the bond-coat and the substrate. Figure 18 shows micrographs of these same coating systems after 658 (furnace test) cycles. The 24 w/o MgO-ZrO_2 coating (Figure 18a) completely spalled from the NiCrAlY after 517 cycles, but the 8 w/o Y_2O_3-ZrO_2 ceramic was still adherent after 658 cycles (Figure 18b). In Figure 18(a) there is now substantial interdiffusion of the substrate and bond coating as evidenced by the precipitates formed in the Rene'80 base alloy. However, in Figure 18(b), there is less

TABLE V

SUMMARY OF TBC LIFETIME AVERAGES

Variation	Lifetime Differences
NiCrAlY Composition	Ni-22Cr-10Al-1Y lasted 33% longer before failure initiation and 21% longer for complete failure than Ni 16Cr 6Al 0.5Y
Ceramic Composition	8 w/o Y_2O_3-ZrO_2 lasted 33% longer before failure initiation, 33% longer before failure completion than 24 w/o MgO-ZrO_2 12 w/o Y_2O_3-ZrO_2 lasted 37% longer before failure initiation, 36% longer for failure completion than 24 w/o MgO-ZrO_2
Deposition Process	NiCrAlY coatings applied using the LP/HV deposition process lasted 31% longer before failure initiation and 25% longer before failure completion than air applied coating
Substrate Compostion	Coatings applied to René 80 substrates lasted 19% longer before failure initiation and 17% longer before failure completion than Hastelloy-X substrates
Ceramic Thickness	0.25 mm thick ceramic coatings lasted 5% longer before failure initiation and 5% longer before failure completion than 0.51 mm thick coatings

Note: The severity of the cyclic furnace test was markedly increased by increasing the maximum temperature from 1000° to 1100°C after 500 cycles.

interdiffusion, presumably because of the oxides at the bond coat substrate interface. In general, the TBC variations in which the ceramic coating had not failed after 658 cycles did not exhibit as great a degree of interdiffusion between the NiCrAlY and the substrate as the shorter-lived variations. In each case the interdiffusion appeared to be blocked by an oxide at the NiCrAlY/ substrate interface. Thus, interdiffusion of the bond coat layer with the substrate may be a life-determining degradation mechanism.

3.3.4 Microprobe Analysis

In an effort to understand any degradation which might occur in TBC systems during high-temperature exposure, microprobe analyses were performed on coated Rene'80 specimens before and after cyclic furnace testing described earlier in 3.3.1.

3.3.4.1 Pre-Exposure Characterization

Electron microprobe measurements on Rene'80 coated with LP/HV-applied Ni-22Cr-10Al-1Y were made prior to cyclic furnace exposure. On some samples, the high Al and Ti concentrations at the Rene'80 NiCrAlY interface suggest that some oxidation (TiO_2,Al_2O_3) may have occurred during the deposition of the NiCrAlY onto the Rene'80 substrate (Figure 19). Varying amounts of NiCrAlY oxidation occurred during the air deposition of the ceramic. In some cases the NiCrAlY/ceramic interface had no detectable excess concentration of Al, (Figure 19). In contrast at other areas of the same sample an Al_2O_3 scale (Figure 20) formed on the NiCrAlY. Thus, under some circumstances the ceramic is adhering to an Al_2O_3 layer and not metallic NiCrAlY.

3.3.4.2 Characterization after 67 cycles at 1100 °C

Microprobe measurements of LP/HV-applied coatings of NiCrAlY and air-sprayed 12 w/o Y_2O_3-ZrO_2 on Rene'80 substrates after oxidation testing show that the Rene'80 and NiCrAlY have interdiffused and become compositionally very similar. Except for compositional fluctuations at precipitate inclusions, the uniformity of the Cr, Ti and Al content of the substrate and the NiCrAlY coating in the vicinity of their original separating interface is shown in Figure 21. This is also apparent in Table VI. However, Y shows no evidence of interdiffusing into the Rene'80,

TABLE VI

AVERAGE COMPOSITION OF RENÉ 80 AND NiCrAlY BEFORE AND AFTER 67 ONE-HOUR CYCLES OF OXIDATION

	René 80		NiCrAlY	
	Before	After	Before	After
Ni	62.0 ± 0.4	64.2 ± 1.0	66.0 ± 1.0	65.2 ± 1.0
Cr	14.1 ± 0.3	17.4 ± 0.75	21.9 ± 0.5	19.6 ± 0.4
Al	3.5 ± 0.2	4.7 ± 0.4	10.3 ± 0.2	4.4 ± 0.2
Y	0	0	1.3 ± 0.3	0.8 ± 0.6
Ti	4.5 ± 0.1	2.9 ± 0.7	0	2.3 ± 0.6

although it does seem to concentrate at the Al_2O_3 scale on the NiCrAlY. Diffusion of Ti, Cr and Ni into the ZrO_2 from the NiCrAlY is also evident.

Microprobe analyses were also performed on failed air-sprayed Ni-22Cr-10Al-1Y and air sprayed 12 w/o Y_2O_3-ZrO_2 coatings on Rene'80 substrates. In contrast to the preceding LP/HV case step-scan analyses of this coating system indicated there was almost no interdiffusion of NiCrAlY and Rene'80 (Figure 22), probably due to the oxide layer.

3.3.4.3 Characterization After 658 Furnace Cycles.

Optical micrography as well as microprobe measurements were made on Rene'80 substrates coated on two sides with different TBC variations, and exposed to the furnace cycle described in 3.3.1. Figure 18 shows optical micrographs after cyclic oxidation of two sides of a representative specimen. Side No. 1 (upper micrograph) had an LP/HV-applied Ni-22Cr-10Al-1Y bond coating with a 24 w/o MgO-ZrO_2 ceramic coating that had spalled during testing. Side No. 2 (lower micrograph) had the same NiCrAlY coating as Side No. 1 but had an 8 w/o Y_2O_3-ZrO_2 ceramic top coat. There were more platelet precipitates in the Rene'80 on Side No. 1 after cyclic oxidation than occurred on Side No. 2. The precipitates are a result of Al diffusion from the NiCrAlY into the Rene'80. The lack of precipitates in the Rene'80 of Side No. 2 suggests that less Al diffusion had occurred, presumably because of the greater amount of oxides seen at the NiCrAlY/Rene'80 interface. Since interdiffusion of Rene'80 and NiCrAlY may be life-limiting for TBC systems, the composition of the oxides at the Rene'80/NiCrAlY interface was investigated.

Figures 23 and 24 show elemental x-ray density maps of Al, Ti, Co, Ni, and Cr for Sides No. 1 and No. 2, respectively. According to Figure 23, the precipitates in the Rene'80 of Side No. 1 are rich in Cr and deficient in Ni. More detailed elemental step-scan analyses showed that the Cr-rich platelet precipitates are surrounded by an Al-rich layer. The Al x-ray density maps of Figures 23 and 24 clearly show in both cases that the phase at the Rene'80/NiCrAlY interface is rich in Al, presumably as Al_2O_3 and/or a $NiAl_2O_4$ solid solution. The elemental x-ray density maps also suggest that a Ti-rich phase, probably TiO_2, had formed at the Rene'80/NiCrAlY interface for Side No. 1, but not for Side No. 2. The Al_2O_3 would slow the Al diffusion into the Rene'80.

An elemental step-scan can analysis was performed on Side No. 2 to examine in greater detail the interdiffusion of Rene'80, NiCrAlY and 8 w/o Y_2O_3-ZrO_2 ceramic. Figure 25 shows that there are six distinct compositional regions for the Rene'80/TBC system after long-time exposure to an oxidizing environment. Region No. 1 was originally Rene'80 but after exposure has interdiffused with NiCrAlY to form phases richer in Cr and Al. The second region is an Al_2O_3 phase at the Rene'80/NiCrAlY interface. At the NiCrAlY side of the Al_2O_3 layer, there appears to be an enrichment of Y. Region No. 3 was originally the NiCrAlY phase but after exposure now has about 3 w/o Ti and 5 w/o Co. Its original Cr and Al concentrations of 22 and 10 weight %, respectively, have fallen to about 10 and 4.5 weight % respectively. Region No. 4 is a second Al_2O_3 layer with some Y_2O_3 about 10 to 15 μm thick. This layer provides oxidation protection to the underlying metallic layers. Region No. 5 is rich in Y and contains some Zr. Its existence near the Al_2O_3 layer suggests that Y has a high affinity for oxygen and subsequently diffuses "compositionally uphill." The sixth region is the ceramic coating containing mainly Zr and about 6 weight % Y. This is the only region which compositionally is unaltered after exposure to cyclic oxidation tests.

3.3.4.4 Summary of Microprobe Results

The microprobe measurements have shown that elevated temperature LP/HV-applied NiCrAlY coatings interdiffuse readily with the Rene'80 substrates, but that little subsequent oxidation of these coatings occurs. In contrast, air sprayed NiCrAlY coatings do not readily interdiffuse with the Rene'80 substrate, but subsequent oxidation is quite severe. At the reduced pressure conditions of the LP/HV process, little oxidation of Rene'80 to produce Al_2O_3 and TiO_2 at the Rene'80/NiCrAlY interface was observed; but the oxidizing conditions of the air process allows the formation of these oxides during NiCrAlY coating. Therefore, for both air sprayed and LP/HV-applied NiCrAlY coatings, the 12 w/ Y_2O_3-ZrO_2 coating adheres to an Al_2O_3 scale on the NiCrAlY, but not metallic NiCrAlY. After long-term exposure the Al_2O_3 scale appears to be alloying with the oxidation of the Y in the NiCrAlY.

3.4 Exposure Testing

3.4.1 Hot Corrosion

The hot-corrosion test was intended to evaluate the durability of thermal-barrier-coated (TBC) specimens in a hot-gas-stream environment containing sodium and sulphur.

The test specimens were 0.318 cm (0.125 in.) diameter Rene'80 pins approximately 5 cm (2 in.) long which had been rounded on one end. The TBC covered the rounded end and extended to within 6 mm (0.25 in.) of the opposite end. The coating had a nominal thickness of 0.13 mm (0.005 in.) NiCrAlY bond coat and 0.25 mm (0.010 in.) Y_2O_3-ZrO_2 ceramic top coat. The four coating system variations investigated are listed in Table VII.

One of the BUSHIPS hot corrosion rigs at the Aircraft Engine Group's Thomson Laboratory in Lynn, Mass. was used to expose the test specimens. The rig consists of a jet-fuel-fired burner, a specimen chamber and a rotating specimen turntable which can be inserted into and withdrawn from the chamber. Pin specimens are cemented into a porous ceramic support which is placed on the turntable. The pins stand vertically as they are rotated in the Mach 0.05 hot-gas stream.

The coated pins were tested at a hot zone specimen temperature of 927°C (1700°F) as measured by an optical pyrometer. An atomized, synthetic sea salt solution was mixed with the burner inlet air in an amount to produce 5 ppm sea salt in the hot-gas stream. In addition, the JPS fuel was doped with 0.1% sulphur and burned with a high (30:1) air-to-fuel ratio to insure complete combustion of the fuel and volatilization of the sulphur. The specimens were withdrawn from the rig, cooled to room temperature, and examined once each working day. Specimens were tested for varying lengths of time in order to observe the progression of any corrosive attack which may have occurred.

A total of nineteen specimens were tested. The results are summarized in Table VIII. The specimens after testing are shown in Figures 26a-d. Although formation of visible cracks in the ceramic layer was considered failure, the specimens were not necessarily removed from the test at that time. All specimens with coating B (12 w/o Y_2O_3-ZrO_2, LP/HV) developed cracks and some delamination in the ceramic layer during testing. Only two with coating A (8 w/o Y_2O_3-ZrO_2, LP/HV), one with coating C (8 w/o Y_2O_3-ZrO_2, Air) and none with coating D (8 w/o Y_2O_3-ZrO_2, Air, NASA) cracked. No cracking or other damage was observed in the bond-coat layer.

TABLE VII

COATING VARIATIONS INVESTIGATED FOR EXPOSURE TESTING

Designation	Compositions	
A	8 w/o Y_2O_3-ZrO_2 (air-sprayed)	Ni-22Cr-10Al-1Y (LP/HV process)
B	12 w/o Y_2O_3-ZrO_2 (air process)	Ni-22Cr-10Al-1Y (LP/HV process)
C	8 w/o Y_2O_3-ZrO_2 (air-sprayed)	Ni-22Cr-10Al-1Y (air-sprayed)
D	12 w/o Y_2O_3-ZrO_2 (NASA air-sprayed)	Ni-18Cr-12Al-0.3Y (NASA air-sprayed)

TABLE VIII

HOT CORROSION TEST DATA

AEG #	First Cracks Observed (hours)	Total Test Hours
A1	-	596
A2	-	362
A3	526	526
A4	226	292
A5	-	168
A6	-	0
B1	154	511
B2	296	362
B3	83	207
B4	148	526
B5	83	168
B6	-	0
C1	514	514
C2	-	362
C3	-	525
C4	-	526
D1	-	362
D2	-	511
D3	-	526
D4	-	526
D5	-	168
D6	-	0

A - 8 w/o Y_2O_3 - ZrO_2, LP/HV-applied Ni-22Cr-10Al-1Y

B - 12 w/o Y_2O_3 - ZrO_2, LP/HV-applied Ni-22Cr-10Al-1Y

C - 8 w/o Y_2O_3 - ZrO_2, air-sprayed Ni-22Cr-10Al-1Y

D - 8 w/o Y_2O_3 - ZrO_2, air-sprayed Ni-18Cr-12Al-0.3Y (NASA)

Control specimens which were present in the test rig showed "typical" corrosive attack indicating that the test conditions were normal. For bare Rene'80, the depth of corrosive attack is typically about 0.25 mm (.010") in 500 hours under these test conditions.

Visual examination showed some corrosive attack of the uncoated Rene'80 and some damage to the ceramic near the uncoated end of the pins. This damage may have been due to a reaction between the Y_2O_3-ZrO_2 and the cement used to hold the specimens in the ceramic support or to excessive condensation of corrosive salts near the base of the specimens. Many of the cracks which developed in the ceramic coating appear to have originated in this region.

The corrosion test pins were embedded in epoxy, sectioned, and mounted for metallographic polishing. Typical microstructures of specimens in the as-coated condition and after testing are shown in Figure 27. Readily apparent in the tested specimens are the formation of a distinct layer at the oxide/bond coat interface and a diffusion zone extending into the Rene'80 substrate. Microprobe analysis helped determine the compositional makeup of the microstructure.

Figures 28 through 31 show secondary electron images and elemental x-ray density maps of specimens as-coated and after testing. The specimens in Figures 28 and 29 have a bond coat applied by the LP/HV process, while the specimens in Figures 30 and 31 have an air process sprayed bond coat. The layer formed at the oxide/bond coat interface is shown to have a high Al content and is believed to be Al_2O_3. Aluminum oxide also appears to be present between NiCrAlY particles in the air sprayed bond coats. This is the case even for the specimen in the as-coated condition and indicates that there was some oxidation of the bond coat particles during the plasma spray application. In both of the tested specimens, Al has diffused into the substrate while particles of high Cr content were precipitated near the bond coat/substrate interface. This effect is less noticeable in the specimen with the air process bond coat, probably because of an Al_2O_3 film around the metal particles acting as a diffusion inhibitor.

A schematic diagram identifies the various phases present in a typical specimen with LP/HV applied bond coat after testing (Figure 32). The Rene'80 substrate, which has a fine γ-γ' structure after the normal alloy heat treatment, forms a coarsened structure after time at temperature. Near the bond coat/substrate interface, the diffusion of Al results in the formation of additional γ' $Ni_3(Al,Ti)$ and lowers the solubility of Cr which precipitates as α Cr.

The bond coat also forms a coarse γ-γ' structure with occasional α Cr precipitates. The bond coat is primarily γ(Ni solid solution) near the Y_2O_3-ZrO_2 oxide coat due to loss of Al to the Al_2O_3 layer which forms at the interface. The effect of the structural and compositional changes taking place in the bond coat and substrate (near the interface) on the durability of the TBC was not apparent in the hot corrosion testing results.

Two specimens were ground and polished under kerosene to retain any salts or sulphates which may have deposited on the specimens in the corrosive test atmosphere. Subsequent examination on the microprobe revealed no concentrations of Na or S in the specimens. This suggests that the test conditions may not have been sufficient to cause measurable deposits of reactants to form on the ceramic surface or in the surface-connected pores of the ceramic layer.

A failed specimen with coating system B (12 w/o Y_2O_3-ZrO_2, LP/HV) is shown in Figure 33a. All of the specimens with this coating failed during the test, yet there is nothing in the microstructure to distinguish it from the 8 w/o Y_2O_3-ZrO_2 coatings. Perhaps the most significant finding with regard to the 12 w/o Y_2O_3-ZrO_2 specimens was that the as-coated specimen showed a circumferential crack (see Figure 33b) near the ceramic/bond coat interface which indicates that there may have been a problem in the coating process.

Although there was a significant difference in the number of cycles to failure for each coating system variation, there was no evidence that corrosion led to the failures since no evidence of corrosive attack or penetration into the ceramic was detected. The difference in lives may be related more to the ability to apply the coating satisfactorily to the small radius of curvature pin specimens than to the test conditions.

3.4.2 Cyclic Oxidation

The Simulated Engine Thermal Shock (SETS II) test rig located at the Materials and Process Technology Laboratory in Evendale, Ohio was used to impose two "engine simulative" conditions on thermal barrier coated specimens: 1) thermal cycling with rapid heatup and cooldown and 2) internal specimen cooling to enhance the thermal gradient across the coating and substrate thicknesses.

The test specimens were Rene'80 tubes 8.9 cm (3.5 in.) long with an inside diameter of 1.3 cm (0.5 in.) and a wall thickness of 0.13 cm (0.050 in.). The specimens were coated with nominal thickness of 0.13 mm (0.005 in.) NiCrAlY-bond coat and 0.25 mm (0.010 in.) Y_2O_3-ZrO_2 ceramic top coat. The four coating system variations investigated are listed in Table VII.

The SETS II rig (Figure 34) has a circular array of eight fixed specimen stations. Six burner pairs and two air-blast jets are located on a rotating platform inside the ring of specimen stations, and they are automatically indexed to each specimen in a clockwise direction. Air and gas are fed to the burners and air jets through slip seals in the central column. The tube specimens were supported by welding a stainless-steel tube to one end of the coated tube and then attaching stiff rods which were clamped in a support post. Cooling air was fed to the stainless steel tube and up through the specimen. A small hole was drilled through the back side of the specimens to sight a radiation pyrometer on the inside wall on the hot side of the tube. The ceramic surface temperature was read by sighting a pyrometer on a Pyromark^R spot painted on the surface on one of the specimens. The two temperature readings gave a measure of the ΔT. A plot of ΔT versus tube inside wall temperature is shown in Figure 35.

The SETS II test was run with an indexing interval of 7.5 min. Thus, a test cycle consisted of a rapid heatup and hold at high temperature for 45 min followed by a forced-air quench and hold near room temperature for 15 min. (At the start of the test, one of the burner stations was not operating properly and so, the cycles were 37.5 min heating, 22.5 min cooling. The burner was changed after 107 cycles when the test was stopped to replace a failed specimen.) Temperature measurements during the test showed the ceramic surface temperature to be 1093 ^oC (2000 ^oF) with an inside wall temperature of 1050 ^oC (1920 ^oF), giving a ΔT of 44 ^oC (80 ^oF). A total of fourteen specimens were tested. The results are summarized in Table IX and show that coating systems A (8 w/o Y_2O_3-ZrO_2, LP/HV) and C (8 w/o Y_2O_3-ZrO_2, air) to be comparable in performance. These two systems are far superior to coating systems B (12 w/o Y_2O_3-ZrO_2, LP/HV) and D (8 w/o Y_2O_3-ZrO_2, air). Figure 36 presents the results in chart form. All of the coatings spalled in a similar manner. Typical failed specimens are shown in Figure 37.

The tube specimens were embedded in epoxy, sectioned, and mounted for metallographic polishing. Visual examination of the sectioned tubes showed a

TABLE IX

SETS II CYCLIC TEST DATA

Specimen *	Cycles To Fail	Total Cycles in Test	Time at Temperature to Fail	Total Time at Temperature in Test	Average ** Cycles to Fail	Average Time** at Temperature to Fail
A1	242	250	168	174		
A2	184	197	138	148	216±30	156±15
A3	242	250	168	174		
A4	197	197	148	148		
B1	107	178	67	120		
B2	172	178	116	120	102±51	70±32
B3	64	72	48	54		
B4	64	72	48	54		
C1	178	178	120	120		
C2	205	250	140	174	234±75	166±64
C3	319	319	239	239		
D1	85	107	53	67		
D2	123	178	79	120	121±35	83±32
D3	155	268	116	201		

*A - 8 w/o Y_2O_3-ZrO_2, Ni-22Cr-10Al-1Y (LP/HV)
B - 12 w/o Y_2O_3-ZrO_2, Ni-22Cr-10Al-1Y (LP/HV)
C - 8 w/o Y_2O_3-ZrO_2, Ni-22Cr-10Al-1Y (air)
D - 12 w/o Y_2O_3-ZrO_2, Ni-18Cr-12Al-0.3Y (air)

**Numbers given are the average ± 1σ

variation in tube wall thickness for most of the specimens. The wall thickness was maximum on the side of the tube which faced away from the burners during testing and minimum on the hot side of the tube. This variation is believed to be due to a repetitive sequence of formation and spallation of oxide scale on the hotter portions of the inside surface of Rene'80 tubes during thermal cycling.

Typical microstructures of the cyclic oxidation specimens in the region where coating spallation occurred are shown in Figure 38. The microstructure is similar to that which was observed in the corrosion pins and described earlier. Notable differences are the increased extent of bond-coat oxidation, particularly for the specimen with an air sprayed bond coat. For the same specimen, there is an absence of α Cr precipitates at the bond coat/substrate interface. Examination of all the specimens revealed a tendency for the α Cr precipitates to go back into solution when specimens remained in the test rig for an extended time (34 to 85 h) after spallation of the ceramic coating had begun.

The variation in the microstructure around the circumference at about 60° intervals is shown in Figures 39 and 40. The change in severity of the bond coat oxidation due to the circumferential temperature variation is particularly noticeable, as is the variation of the bond coat and substrate microstructures.

Examination of the test specimens did not reveal any marked differences in the microstructure between corresponding coating systems. This suggests that the differences in test performance were due to the application process variables and or compositional differences.

3.4.3 Hot Corrosion and SETS II Exposure Test Conclusion

Conclusions. While the results of the hot-corrosion test could not be said to have distinguished between the coating system variations being investigated, they did demonstrate that substantial corrosion protection of the substrate alloy was provided by the presence of the TBC. Additionally, the compositional and microstructural changes indicate that this factor should be considered in the evaluation and design of future bond coat compositions due to the strong interaction between the bond coat and the Rene'80 substrate (particularly with the LP/HV bond coat).

The SETS II cyclic testing showed the 8 w/o Y_2O_3-ZrO_2 TBC to be more durable than 12 w/o Y_2O_3-ZrO_2. For the two deposition processes used (air and

LP/HV), the LP/HV-applied bond coat resulted in a more consistent TBC life than the air-applied bond coating, but did not increase the average life of the coating. The exposure tests indicate that of the coating systems evaluated the best system is the 8 w/o Y_2O_3-ZrO_2 TBC with the LP/HV-applied bond coat.

4.0 DESIGN AND ANALYSIS

Analytical studies were performed to assess the benefit to be derived by the application of a thermal barrier coating (TBC) to CF6-50 stage 2 high-pressure turbine (HPT) blades. These studies considered the dependence of blade life, turbine efficiency requirements and blade cooling air flow on coating thickness. In addition, the effect of local spallation was assessed. This work led to recommendations of a coating configuration for subsequent application of the TBC to stage 2 blades. Finally, a refined coated airfoil concept which more fully utilized the benefits of thermal barrier coatings was designed and evaluated.

4.1 Heat Transfer Analysis

A detailed thermal analysis of thermal barrier coated (TBC) CF6-50 stage 2 HPT blades was done through General Electric's Transient Heat-Transfer Program (THT-D). The THT-D is well suited for this analysis since the user can accurately simulate radiation, free convection, contact resistance, and coolant circuit temperature changes during a transient operation.

Figure 41 summarizes for the CF6-50 stage 2 HPT blade, the standard cooling circuit, the blade cooling geometry, cooling flow distribution, and design conditions. A total of 0.9% of core flow is bled from compressor discharge for use in four circuits: leading edge radial, two mid-chord serpentines, and a trailing edge radial. The passages do not have turbulence promoters, and no surface film cooling is used.

The analysis of the stage 2 blade was conducted at the pitch section (at 50% radial span) with a finite-element computer model. The uncoated blade pitchline metal temperature distribution at the design point (Figure 42) was the base case for the heat transfer trade-off study in evaluating coating effects on blade temperatures. To account for the bond and ceramic coatings, additional nodal layers were added to the existing grid configuration. Approximately, 10 heat transfer trade-off cases were analyzed with three different cooling flows (100, 75, and 50%) and three ceramic coating thicknesses 0.25 mm (0.010 in.), 0.38 mm (0.015 in.), and 0.51 mm (0.020 in.). A constant 0.10 mm (0.004 in.) bond-coat layer was used for all cases. The thermal properties of the coatings which were available at the time of the temperature analyses are given in Figures 43 and 44.

The aerodynamics and the gas-side heat-transfer coefficient distribution were assumed to be unchanged by the presence of the TBC. The gas-side area, the base metal geometry and the coolant heat pickup were kept constant. (These assumptions lead to a slight underestimation of the bulk metal temperature, but the magnitude of the error is considered to have a minor effect on the accuracy of the present parametric studies.)

Temperature distributions at the various nodal points were determined. These were combined to provide measures of the average temperatures of the blade, bond coats and ceramic layer. The temperature distribution for a stage 2 blade with a 0.25 mm (0.010 in.) of ceramic and 100% of the base coolant flow is shown in Figure 45. For this case, the average bulk metal temperature of the blade was reduced from 951 °C (1744 °F) to 919 °C (1687 °F) because of the presence of the TBC. Figure 2 summarizes analyses of the effects of ceramic coating thickness and blade cooling flow variations on the blade bulk metal temperature. The greatest benefit from the TBC is the potential reduction of cooling flow and the associated engine performance gain.

Increasing ceramic coating thickness reduces the average temperature of the bond coat and bulk metal (Figure 46). Variations in the thermal conductivity of the ceramic can result from differences in coating composition and application methods. Figure 46 can be used to show the effect of different conductivities because at steady state the thermal resistance of the thermal barrier is proportional to thickness divided by conductivity.

4.2 Transient Thermal Response Analysis

The thermal barrier coating not only reduces the bulk metal temperature but also slows the transient response and changes the temperature distribution. The response of a stage 2 blade with TBC to a transient cycle was calculated. The transient cycle for the CF6-50 engine in Figure 47 shows that the acceleration is severe (the speed increase is from 6500 to 9400 RPM in just seven seconds) and the required short term power requirement produces a high heat flux in the blades. The temperature response of the blades was analyzed for the airfoils left uncoated, coated with 0.25 mm (.010 inch) of ceramic, and coated with .038 mm (.015 inch) of ceramic. Figure 48 shows the response of the leading and trailing edge surfaces during the acceleration portion of the cycle for coated [0.25 mm (0.010 in.)] and uncoated blades. The peak temperature gradients are significantly reduced by the presence of the TBC. The severity of the thermal stress as indicated by the temperature difference ΔT between the blade surface and the mean bulk temperature is significantly reduced at the leading edge (LE) by the TBC. Also the time to reach the maximum ΔT is slightly longer, i.e. the TBC insulating effect provides thermal inertia. In approaching steady state, both coated and uncoated blades respond in a parallel manner. Although initially the relative response of uncoated blades at the trailing edge (TE) is analogous to that at the LE, there is a cross-over of the ΔT plots as steady state is approached. This is due to the fact that the slenderness of the trailing edge portion does not allow as efficient cooling as at the LE. Thus, although the TBC results in some temperature reduction at the TE, it is not as great as for the blade as a whole. Hence ΔT actually increases over that for an uncoated airfoil.

The corresponding transient stress response of the metal substrate during the same acceleration portion of the cycle is given in Figure 49, and the detailed transient temperature distributions are found in Figures 50 and 51. In Figure 49 the edge stress of the very hot TE is seen to be compressive, whereas the similarly hot LE is tensile. This tension results from the combined centrifugal and thermal tilting or bending of the blade plus the centrifugal loading. The TBC in the TE produces sufficient temperature reduction to avoid the large excursion of the thermal compressive stress. It is interesting to note that the selected thickness of 0.25 mm results in a peak transient tensile stress at the TE, whereas an uncoated blade experiences a peak transient compressive stress. Thus, an intermediate thickness could presumably minimize the transient stress range in this region. This illustrates the kind of tailoring that must be considered in the effective use of TBCs.

4.3 Mechanical Analyses

In conducting the mechanical analyses of the various coating system configurations, the following assumptions were used:

(1) the life limiting span of the airfoil is the pitch section for both the coated and uncoated configuration;

(2) no creep or plasticity occurs in the bond or ceramic layers;

(3) application of the bond and ceramic layers leaves them in an unstrained (stress-free) condition after cooling to room temperature;

(4) material properties for the NiCrAlY bond layer and the ceramic outer layer are referenced from NASA Report CR-135359 (Figures 43 and 44).

The heat transfer results of the cases shown earlier for the various thermal barrier thicknesses and cooling flows in the stage 2 high-pressure turbine (HPT) blade were analyzed the GE computer program Bucket Creep III (BC III) to determine combined mechanical and thermal stresses. The BC III predicts time-dependent localized values of stress, strain, and creep damage of cooled gas turbine airfoils exposed to high-temperature environments.

The uncoated (base case) airfoil pitch section steady-state stresses are shown in Figure 52; the blade mechanical and combined mechanical and thermal stresses for the same airfoil with a 0.25 mm (0.010 in.)-thick thermal barrier coating are shown in Figure 53. The stresses in the metal substrate (Rene'80) material are slightly greater because of the additional weight of the bond coat and the ceramic layers. However, even though stresses increased, the rupture life in the metal blade was improved more than tenfold with the addition of the TBC. This is expected, since the bulk metal temperature was reduced 32 °C (57 °F) from 951 °C (1744 °F) to 919 °C (1687 °F).

The absolute values of the elastic stresses in the NiCrAlY bond layer are generally smaller than for the metal substrate, primarily because of the low value of the Young's modulus of the bond layer at elevated temperatures. The computed tensile stresses in the ceramic layer are greater than in the bond coat. These higher stresses are due to the greater thermal expansion of the metallic bond coat layer relative to that of the ceramic outer layer. This occurs in spite of the higher ceramic temperature because the ceramic expansion coefficient is only about two-thirds that of the bond layer. However, note that this result is conditioned by the previously stated assumption that the ceramic is stress-free under room temperature conditions.

Additional increases in coating thickness will further lower the metal temperature and, in turn, improve blade rupture life. Thus, stress rupture is not limiting. However, high-pressure turbines are susceptible to low-cycle fatigue (LCF) failures related to transient thermal stresses. Therefore, to gain an understanding of the effect of TBC on LCF, a simplified engine transient stress analysis was conducted.

This transient elastic stress analysis was performed on the pitch section of the CF6-50 stage 2 HPT blade with the engine cycle shown previously in Figure 47. The analysis was conducted on both the uncoated airfoil and on the airfoil coated with 0.10 mm (0.004 in.) of bond coat and 0.25 mm (0.010 in.) of ceramic.

The results reveal that the blade (Rene'80) LCF life improved with the addition of the thermal barrier coating. The resulting strain range distribution for the blade is shown in Figure 54, the strain level at the leading edge (LE) has increased during the transient acceleration for the coated airfoil. This increased strain range is due to the reduced difference in LE temperature versus the blade bulk temperature as shown previously (Figure 48). The lower ΔT induces lower compressive thermal stresses in the LE, yielding a larger combined mechanical and thermal tensile stress. However, the corresponding LCF life increases because of the reduction in bulk metal temperature which increases the material LCF strength. The trailing edge (TE) shows similar results, with the coated blade being driven into tension because of the reduction in ΔT. In summary, the TBC has redistributed the blade temperatures especially of the TE. This redistribution plus the lesser thermal expansion of the TE, tilts the blade thermally, raising the LE strain. However, the lowering of the temperature at the LE is sufficient to result in a net LCF life improvement there.

Because the metal substrate shows improvements in both LCF and rupture life with the addition of coating to the blade, it appears that the potential of the thermal-barrier-coated airfoil is limited only by the lifetime of the ceramic coat or of the ceramic/metal bond.

4.4 Spallation Studies

The preceding analyses have assumed that the bond and ceramic coatings remain adherent to the metal substrate for the of the blade. Although it is not presently possible to predict analytically exactly when and where local spalling failure of the TBC might occur under engine conditions, the consequences of this type of failure to the blade were determined. To examine the effects of partial coating loss on the blade rupture life, four steady-state cases were studied (Figure 55). The studies for these four cases indicate that, if partial coating loss occurs, the airfoil would have less rupture life than the blade fully coated (Figure 56). Even so, the blade with partial coating loss has more rupture life available than an uncoated airfoil.

For LCF evaluation, an engine transient analysis was conducted on the pitch section of the blade with the assumption that leading and trailing edges had spalled the ceramic and bond layers. An example of the temperatures calculated for the spalled conditions is given in Figure 57. The major concern was that should the TBC spall, the now uncoated region would heat up closely approaching the original uncoated temperature, while the remaining coated airfoil being significantly cooler would force unacceptably large thermal strains in the spalled region. This worst case scenario was shown to be unfounded, however. For the case analyzed with LE and TE spalled (see Figure 57) LCF was reduced from the fully coated case and even somewhat below the original uncoated case at the limiting TE point. However, the LCF life would be 70% of the uncoated blade life which is more than adequate for a 1500 "C" cycle CF6-50 engine test (Sections 5.3 and 5.4). Bench test and then engine test corroboration is required, however

4.5 TBC Payoffs

To establish the related engine benefits of the TBC coated airfoil and to aid in selecting the coating configuration to be run in an engine test, three parameters were examined to determine their effects on engine specific fuel consumption (SFC): (1) cooling flow, (2) trailing edge blockage, and (3) surface finish.

Surface roughness has a larger effect on turbine performance/efficiency than TE blockage effects. Should the initial surface finish of 2 μm rms (polished TBC surface) deteriorate to 7.5 μm rms, as a severe limiting case, the SFC penalty would be about 0.15%. Individual plots of these performance relationships are given in Figures 58 through 61.

One way to take advantage of the thermal-barrier-coated airfoil is to reduce the blade cooling flow while maintaining an equivalent rupture and low-cycle fatigue life in relation to the uncoated configuration. The cooling flow could be reduced to about 50% of the original value and still maintain the bulk metal temperature of the uncoated airfoil. Additionally, at this reduced cooling airflow condition, the calculated rupture life of the blade would be slightly greater than for the uncoated design. This would yield a benefit in SFC of 0.32%.

The addition of TBC to existing blade designs, without modification to account for the decreased throat area, would reduce the turbine efficiency causing an increase in SFC. With the current configuration completely coated with 0.254 mm (0.010 in.) of ceramic and 0.102 mm (0.004 in.) of bond coat, the SFC penalty would be only 0.048% for the trailing edge blockage effects.

4.6 Conclusions and Recommendations for Engine Test Blades

The presence of a thermal barrier coating on the CF6-50 stage 2 HPT blade has been shown through computer analysis to provide substantial benefit. This benefit can be realized in two ways: 1) the TBC reduces the average bulk metal temperature which results in improved LCF and rupture life; 2) while maintaining the bulk metal temperature at normal levels, the cooling air flow could be reduced by about 50% which improves turbine efficiency and provides fuel savings. Additional analysis showed that TBC spallation from critical areas of the blade had the potential to reduce blade life and rupture life below that of an uncoated blade, even though 100% coolant flow was maintained, due to the local hot spot and resulting higher strain in the spalled region.

In selecting a TBC blade design for further laboratory evaluation and engine testing it was obvious that the present stage 2 blade would limit the manner in which TBC could be utilized to achieve the payoffs identified. The best payoff would require a blade which integrated TBC features from the initial design point. Thickness and TBC location could be integrated with cooling passages and the internal cooling schemes.

Within the constraints of the current stage 2 blade however the recommended TBC configuration was as follows: 0.10-0.15 mm (0.004-0.006 in.) of NiCrAlY bond coat and .25 mm (.010 in.) of Y_2O_3-ZrO_2 ceramic top coat over the entire airfoil and platform surfaces of the CF6-50 stage 2 HPT blade (Figure 62) and with a 100% coolant flow was recommended for laboratory evaluation and engine testing.

4.7 Refined Coated Airfoil Concept Based on Materials Development

If, for purposes of conceptual exploration, the restriction of putting a design immediately into an actual engine for test can be relaxed, it would be desirable to contemplate how to take maximum advantage of TBCs. Accordingly, design studies were undertaken which took into account the results obtained in the parallel materials development and evaluation efforts described in Section 3.

Analytical studies described in the preceding sections indicated that with the application of a TBC to the CF6-50 stage 2 HPT blade, the coolant flow could be reduced to about 50% of the metal blade design level while maintaining metal substrate lives and temperatures equivalent to the uncoated blade. Figure 63 presents a comparison of the detailed temperature distributions at the pitch section of the stage 2 blade for the uncoated airfoil, coated airfoil with 100% flow, and coated blade with 50% flow. It is noteworthy that the metal temperatures in the trailing edge are relatively unaffected by the application of the TBC to this region even when the cooling air is maintained at 100% flow.

From laboratory furnace tests the effects of temperature on coating life was investigated. TBCs exposed to a maximum temperature of 1000 °C (1832 °F) lasted about 10 times longer than those that had been heated to 1100 °C (2012 °F). At the lower temperature, the magnitude of observed furnace lifetimes substantially exceeded the duration of the planned engine tests. However, because of the more severe conditions in an actual engine, a design specification of 982 °C (1800 °F) for the allowable maximum temperature of the TBC/metal interface was tentatively selected. The calculated temperatures for the trailing edge sections given in Figure 63 already exceeded this design temperature limit.

Two studies were undertaken to overcome this limitation. The objective of one study was to determine the best coating configuration with a CF6-50 production blade assuming the bond-coat design temperature limit. The other study was to redesign the

CF6-50 stage 2 HPT blade with the thermal barrier coating integrated into a totally new design.

4.7.1 Study I: Best Present Blade Configuration with 982 °C (1800 °F) Bond Coat Limitation

This concept, based on the present CF6-50 stage 2 HPT production blade, is directed at minimizing the coolant flow, satisfying the dual requirements of 1) maintaining present blade life and 2) holding the NiCrAlY temperature below the assumed 982 °C (1800 °F) limit. The result of this study (Figure 64), indicates that, except at the trailing edge region, the airfoil would be fully coated with 0.51 mm TBC. For this TBC design configuration, the air cooling flow could be reduced to 65% of the uncoated design flow. Figure 65 gives the temperature distribution for this "improved" TBC configuration. Since in this design the trailing edge is not coated with TBC, there is no reduction in turbine efficiency because of trailing edge blockage.

4.7.2 Study II: Advanced Blade Configuration with TBC

This effort was aimed at conceiving an improved blade configuration which would derive maximum benefit from the TBC in terms of reduced airfoil coolant flow. The basic parameters used in deriving this configuration are as follows:

(1) airfoil contour remains unchanged from the uncoated design;

(2) mass of the blade is reduced to achieve a quick bulk temperature response which diminishes transient gradients between bulk and leading and trailing edges;

(3) bond coat temperature is held to the assumed design limit of 982 °C (1800 °F);

(4) temperature differences between bulk and trailing edge are maintained or reduced relative to the uncoated design.

Since the benefits of thermal barrier coating are greatest in regions of high heat flux, the optimum blade concept utilized impingement baffles and turbulence promoters to increase the convection coolant coefficients. In addition, knowing that the metal substrate at the blade trailing edge has higher temperature capabilities than the assumed bond coat limit, the trailing edge is designed to be uncoated. However, in order to reduce the difference in the bulk temperature and trailing edge temperature for the TBC design, the majority of the coolant air would be used as film cooling through a row of holes on the pressure-side surface. To match the gas stream flow path radial temperature profile, these film cooling holes would only be needed to cool the hottest section of the blade trailing edge between the 30 and 70% airfoil span.

With this type of advanced TBC cooling design concept (Figure 66) the coolant air flow could be reduced to about 55% of the base uncoated blade. If a higher bond coat temperature capability were assumed ~1038 °C (1900 °F), the blade could be fully coated which would result in still lower coolant flow and higher benefit.

4.7.3 Benefits of Refined Conceptual Designs

The refined coated airfoil studies demonstrated the possibility of improving the thermal barrier coating benefit over that obtained for a fully coated, standard blade. A comparison of this improvement, in terms of specific fuel consumption (SFC), is shown in Table X. The benefit obtained was maximized by the optimum blade design with TBC developed in Study II.

TABLE X

Payoff Comparisons for the CF6-50 Stage 2 HPT Blade With Various TBC Configurations

Configuration	Coolant Flow	Coating Thickness	Δ SFC*
Standard Blade Uncoated	100%	0	0
Standard Blade** Fully Coated	100%	.254mm(.010 in.)	+0.048%
Standard Blade ** Fully Coated	50%	.254mm(.010 in.)	-0.322%
Study I: Fully Coated Except Trailing Edge	65%	.381mm(.015 in.)	-0.260%
Study II: New Design Fully Coated Except Trailing Edge	55%	.381mm(.015 in.)	-0.370%

* Negative values are improvements, positive values are penalties

** Bond coat temperature exceeds the assumed design limit of 982°C (1800°F) at the airfoil trailing edge.

5.0 COATED TURBINE BLADE LEADING TO ENGINE TESTS

This portion of the work was undertaken (1) to implement the recommendations that emerged from the materials development and characterization efforts, (2) to adapt the developed coating techniques to the present complex geometry of blades, (3) to develop adequate coating process control and reliability to satisfy engine test requirements, (4) to provide representative blades for conducting the necessary bench tests to qualify coated blades for engine testing, (5) to test coated blades in an actual engine and, (6) to evaluate their performance.

The CF6-50 stage 2 HPT blade uniformly coated with TBC on the airfoil and the flow path surfaces of the platform was used to evaluate the coatings. The two plasma spray processes (air and LP/HV) were re-evaluated for the blade geometry because of the obvious differences that would result in thermal history compared with coupon preparation. It was also necessary to determine whether the aluminide coating standard on engine-quality blades would affect the TBC deposition process or behavior. Twenty engine-quality blades were coated. Most were used in the required pre-engine qualification tests. Six blades were evaluated on a piggyback basis in a CF6-50 test engine. During the engine exposure the coatings remained adherent, although with indication of localized foreign object damage at the leading edge. The test run was terminated after 626 cycles for reasons not related to these blades.

5.1 Plasma Spray Process Development for Blades

The requirement was to deposit uniform and durable coatings on the stage 2 blades at a thickness of 0.10 to 0.15 mm (0.004 to .006") for the NiCrAlY layer and 0.25 mm (0.010") for the oxide coating. Both the air and the LP/HV processes were investigated for applying the metal layer; only the air process was used for the oxide.

5.1.1 Air Process

Prior to coating, all blades were grit-blasted and ultrasonically cleaned and degreased. The CF6-50 stage two HPT blades were manually coated in air with Ni-22Cr-10Al-1Y and 8 w/o Y_2O_3-ZrO_2. The coatings were applied by spraying overlapping bands of coating on the airfoil. A single band was sprayed by passing the gun from the tip to the root radius of the airfoil. The blade was rotated so that deposition was always perpendicular to the substrate. Overlapping bands were applied repeatedly until the desired thickness was obtained. The platform was coated at an angle of about 30° from the perpendicular.

5.1.2 LP/HV Process

Six CF6-50 stage 2 HPT blades were coated with Ni-22Cr-10Al-1Y using the LP/HV deposition process. A microprocessor controlled the gun motion, which consisted of linear, horizontal, and vertical movements along with a rotatioı 'ıngular) movement of the gun was used. In addition, the blade was also rotated.

A typical coating run consisted of airfoil heating, cleaning, and coating procedures. Prior to coating, all blades were grit-blasted and ultrasonically cleaned and degreased. At the start of a run, the airfoil was preheated to about 1000 °C in the plasma arc. Oxides which may have formed were removed with the reverse transfer arc process prior to the final coating process.

After coating, one of the NiCrAlY-coated blades was sectioned at the airfoil, platform, and root radius areas for metallographic examination (Figure 67). Table XI lists the microscopically measured NiCrAlY coating thicknesses at various locations on the airfoil sections. The variation in the NiCrAlY was close to the specified tolerance of 0.10 to 0.15 mm. The only area where the NiCrAlY thickness deviated from these values was at the pressure-side root radius area. Figure 68 shows micrographs of the NiCrAlY coating. This figure shows an absence of oxide inclusions in the NiCrAlY. The porosity was observed to be low at the airfoil sections but was slightly greater at the platform and root radius areas of the airfoil. These trends are attributable to the difficulty in applying NiCrAlY uniformly and densely on complex geometries with high radii of curvature.

5.2 Studies Relevant to Aluminide Coating on the Blades

The CF6-50 stage-two HPT blades are Rene'80 alloy. The hot-oxidation resistance of the Rene'80 is ennanced by the use of an aluminide environmental coating in which NiAl is the dominant phase. For the work described in chapter 4 the TBC variations investigated were applied to non-aluminided substrates. However, in an engine consideration was given to insure a fail-safe mode of operation of a blade in the event of losing the TBC protection. Therefore, blades were given an aluminide coating before the TBC was applied. A cyclic furnace test was developed to evaluate the lifetimes of TBCs on the aluminide coated CF6-50 stage 2 HPT blades and to evaluate any airfoil geometry effects on TBC lifetimes. This test was performed simultaneously on two blades and consisted of a 5 min heatup to 1100 °C, a 40 min hold at 1100 °C, followed by a 15 min air blast cooldown. Blades were rapidly

TABLE XI

NiCrAlY THICKNESS (mm) DEPOSITED ON CF6-50 STAGE TWO HPT BLADE USING LP/HV DEPOSITION PROCESS

	Airfoil Section		
	Tip	Center	Root
Leading Edge	0.12	0.09	0.09
Suction Side	0.15	0.105	0.09
Trailing Edge	0.135	0.14	0.15
Pressure Side	0.135	0.11	0.105

Root Radius and Platform

Suction Side	
Platform	0.135
Root Radius	0.14
Pressure Side	
Platform	0.14
Root Radius	0.225

quenched during the 15 min cooldown by blowing high-pressure air through the internal cooling passages. Table XII summarizes the types, numbers, and lifetimes of the coated blades which were cyclic furnace tested. A description of each test series is given below.

5.2.1 Air-Deposited NiCrAlY

5.2.1.1 Uncoated Blades. To get baseline data, one blade was not aluminided. This blade was coated with NiCrAlY and 8 w/o Y_2O_3-ZrO_2 with the procedures described above for the air deposition process and subjected to cyclic furnace testing. The coating appeared adherent until the 148th hourly cycle, when a small 1 cm-diameter patch of ceramic had spalled from the convex side of the airfoil. The center of the spalled area was located about 1.5 cm behind the leading edge and 1 cm above the platform. Loss of ceramic also occurred on about 20% of the platform section of the blade. Spallation was noted to occur always at the bond coat/ceramic interface.

5.2.1.2 Aluminide Coated Blades. For these tests four CF6-50 stage 2 blades (aluminide coated) were used. The blades were coated with NiCrAlY and ceramic in air by the procedures described earlier. Micrographs verified that the aluminide coating was not removed by the grit-blasting cleaning step. It is noteworthy that during the NiCrAlY deposition, two of the blades suffered NiCrAlY spallation while the other two were coated without problems. NiCrAlY spallation had not been previously encountered when coating non-aluminided coated substrates and is probably a result of NiAl oxidation during coating. The two blades with spalled NiCrAlY were stripped of NiCrAlY and reprocessed without further problem.

Two blades were initially exposed to the cyclic furnace test described above. After about 24 cycles of testing, loss of coating was evident on the platform of both blades. Not until 168 hr of testing was further spallation detected, this time on the suction (convex) side of the airfoil of one blade. The coating separation appeared to have initiated at the airfoil tip and proceeded down about two-thirds the length of the suction side of the airfoil. Figure 69 is a photograph of the two airfoils after 168 furnace cycles. The TBCs had a mixed failure mode with spallation at the aluminide NiCrAlY interface near the trailing edge, and

TABLE XII

SUMMARY OF CYCLIC FURNACE TESTS OF CF6-50 STAGE TWO HPT BLADES (Aluminide Coated)

	# Blades Tested	Cycles to Cause Spallation from Airfoil
0.15 mm Air-deposited NiCrAlY 8 w/o Y_2O_3-ZrO_2 on uncoated René 80	1	148
0.15 mm Air-deposited NiCrAlY 0.25 mm 8 w/o Y_2O_3-ZrO_2 on NiAl coated René 80	4	(a) 168 (b) 168 (c) 148 (d) 148
0.15 mm LP/HV-deposited NiCrAlY 0.25 mm 8 w/o Y_2O_3-ZrO_2 on uncoated René 80	1	193
0.15 mm LP/HV-deposited NiCrAlY 0.25 mm 8 w/o Y_2O_3-ZrO_2 on NiAl coated René 80	1	193

failure near the ceramic/NiCrAlY interface towards the leading edge. The spallation at the platform occurred at the aluminide/NiCrAlY interface. (In our previous tests on non-aluminided Rene'80 coupons, coating spallation always occurred at the ceramic/NiCrAlY interface.)

A second pair of blades was tested under identical experimental conditions to confirm the first test. After 148 furnace cycles, the TBC on one blade developed cracks on the trailing edge. Testing was terminated after 160 cycles when both blades lost about 50% of their coating on the suction side. The failure occurred by peeling on one blade (Figure 70c) and by spallation on the other blade (Figure 70a). There was only a minimal loss of coating from the pressure side of one blade (Figure 70b) and no loss of coating from the platforms of either blade. In all cases spallation occurred at the aluminide/NiCrAlY interface, as evidenced by the dark, oxidized NiCrAlY adhering to the ceramic which had popped from the airfoil (Figure 70a). However, in some areas the more common mode of failure between the ceramic and bond coat layers occurred.

In order to determine the cause of spallation at the aluminide/NiCrAlY interface, the tip of one airfoil was sectioned and polished (right-hand blade of Figures 70a and 70b). Figure 71 shows micrographs of the blade sections where (a) NiCrAlY and ceramic had spalled from the aluminide surface, (b) NiCrAlY is just parting from the aluminide surface, (c) 8 w/o Y_2O_3-ZrO_2 spalled from the NiCrAlY, and (d) no spallation of any coating is occurring. In all cases there is some internal oxidation of the remaining NiCrAlY and an oxide layer (presumably Al_2O_3) at the aluminide/NiCrAlY Rene'80 interface. This oxide may be responsible for the poor adhesion of the NiCrAlY, i.e., the Al_2O_3 might weaken the bond at the NiAl/NiCrAlY interface.

5.2.2 LP/HV-Deposited NiCrAlY on Coated and Uncoated Blades

To test the hypothesis that Al_2O_3 formation on the aluminide coating might be responsible for poor NiCrAlY adhesion to NiAl, two blades were coated with NiCrAlY by the LP/HV process and with ceramic by the air process. Only one blade had been given an aluminide coating.

The TBC blades were exposed to cyclic furnace testing. The lifetimes of the TBCs on these two blades were virtually identical. Both ran 193 cycles before any spallation was observed. Figure 72 shows front and back views of the blades after cyclic furnace testing. Spallation was confined to the platform and a small area of the suction side of the blade without the aluminide coating. For the aluminide-coated blade, spallation was somewhat more extensive and occurred on the leading edge, suction side, and on the platform. In all cases spallation occurred at the NiCrAlY/ceramic interface, not at the NiAl/NiCrAlY interface.

5.2.3 Conclusions Regarding Aluminiding

The LP/HV process has two possible advantages over the air process for deposition of NiCrAlY on aluminided Rene'80. The LP/HV process is performed under low pressure, which reduces the formation of oxides. Furthermore, the reverse transfer arc capability associated with the LP/HV process can clean away any oxides formed immediately prior to deposition of NiCrAlY.

In addition, the following three major points summarize the results of the cyclic furnace tests on aluminided and non-aluminided CF6-50 stage 2 blades coated with TBCs:

(1) The lifetime of the Ni-22Cr-10Al-1Y/8 w/o Y_2O_3-ZrO_2 TBC system is not significantly affected by the presence of an aluminide coating on blades.

(2) Lifetimes of TBC systems in which the NiCrAlY is deposited by the LP/HV process are about 20% greater than when the NiCrAlY is deposited by the air process.

(3) Spallation of TBCs in which the NiCrAlY and ceramic are deposited by the air process occurs at both the aluminide/NiCrAlY interface, and the NiCrAlY/ceramic interface.

(4) Spallation of TBCs in which the NiCrAlY was deposited by LP/HV process occurred only at the NiCrAlY/ceramic interface.

5.3 Preparation of Blades for Engine and Pre-Engine Tests

5.3.1 Coating Procedures and Controls

Thirty CF6-50 stage 2 HPT blades were plasma spray coated with Ni-22Cr-10Al-1Y with the LP/HV system. Twenty of the blades were engine-quality blades used for high-cycle fatigue testing and engine testing. Four of the other 10 blades were sentinel blades and were coated at evenly spaced intervals during the coating schedule. These were sectioned to check for coating thickness and microstructural uniformity throughout the coating schedule. The remaining six were used to set up and check out the LP/HV process at the start of coating operations.

The thickness of the NiCrAlY bond coating was determined at five positions on the airfoil surface by gauging the airfoil before and after coating with a micrometer array shown in Figure 73. The coating thicknesses were measured at two positions on the pressure side, two positions on the suction side, and one position at the leading edge of the airfoil. The measured weight and thickness of LP/HV-deposited NiCrAlY on the airfoil are given in Table XIII). The reproducibility of the measurements is about 10 µm. Somewhat more NiCrAlY was deposited at the tip of the blade (Positions 2 and 3) than at the lower portions (Positions 4 and 5) of the blade. The average NiCrAlY coating thicknesses varied from 100 to 200 µm. The weight gain measured for the blades were consistent to within 6% and averaged 9.8 ± 0.6 grams.

After the NiCrAlY coating thicknesses and weights had been measured, 29 of the original 30 blades were further coated with a nominal 280 µm of 8 w/o Y_2O_3-ZrO_2 ceramic with an air plasma spray gun, operated by hand. The ceramic plasma spray powder had a nominal sizing of -200 + 325 mesh.

In order to reduce aerodynamic losses because of surface roughness, the as-sprayed ceramic surfaces were polished with a 280-grit aluminum-oxide paper. This procedure reduced the surface roughness from 350 to 150 micro inches. The ceramic coating thicknesses remeasured after polishing showed that an average of 30 µm of ceramic was removed by the polishing. Table XIII lists the weight of ceramic coating before and after polishing. The complete set of coated and polished CF6-50 stage 2 HPT blades is shown in Figure 3.

Two of the remaining blades were sectioned and metallographically polished to check the coating thickness measurements and to determine the coating microstructure. Typical microstructures of these blade coatings are given in Figure 74.

5.3.2 Qualification Testing

The engine-quality blades coated were sent to Aircraft Engine G. up at Evendale, Ohio. The blades were given a cooling-air flow check, and one of the blades was found to have one circuit with a flow rate below the allowable minimum. All other blades had air flows which fell within the allowable limits.

Eight blades underwent component high-cycle fatigue testing. The blades were heated by an induction coil with a susceptor to 927 °C (1700 °F). The temperature was measured with thermocouples. On all blades, one thermocouple was attached to the underside of the platform on the pressure side of the blade,

TABLE XIII

LP/HV COATING PROCESS RESULTS*
(Weight and Thickness Measurements)

	NiCrAlY		ZIRCONIUM OXIDE			
			As Deposited		After Polish	
Average weight (grams)	9.8 ± 0.6		-		12.6 ± 1.6	
Avg. Thickness	μm	mils	μm	mils	μ	mils
Middle, Leading Edge	130 ± 20	5.1 ± 0.8	290 ± 30	11.4 ± 1.1	250 ± 40	10.0 ±
Upper, Pressure Side	190 ± 30	7.6 ± 1.2	285 ± 30	11.2 ± 1.1	265 ± 40	10.4 ±
Upper, Suction Side	200 ± 25	8.0 ± 1.0	300 ± 30	11.8 ± 1.1	285 ± 30	11.2 ±
Lower, Suction Side	100 ± 12	4.0 ± 0.5	275 ± 30	10.8 ± 1.1	235 ± 35	9.3 ±
Lower, Pressure Side	120 ± 10	4.6 ± 0.4	280 ± 25	11.1 ± 0.9	235 ± 35	9.3 ±

* Combined Results of 24 Coatings. The indicated variation represents the standard error.

and a second thermocouple was inserted into the internal air passages of the blade through one of the cooling air inlet holes in the dovetail. This second thermocouple was removed once thermal equilibrium had been reached and before high-cycle fatigue testing was begun.

High-cycle fatigue testing of the blades began with a blade tip deflection of 2.03 mm (0.080 in.). A "staircase" method was used to determine the tip deflection to be used on subsequent blades. If failure occurred at a given tip deflection, the next blade was tested with 0.254 mm (0.010 in.) less deflection. If failure did not occur (run out was 10^7 cycles), the next blade was run with 0.254 mm (0.010 in.) greater deflection. A summary of the HCF test results is given in Table XIV. The mean tip deflection was found to be 1.91 mm (0.075 in.). This was 13% lower than the mean value for stage 2 blades without a thermal barrier coating; however, it was sufficiently high to qualify the blades to be run in a test engine.

5.4 Engine Tests

Six TBC blades were delivered to CF6-50 Engine Systems for engine testing.

5.4.1 Macroscopic Examination

The blades were assembled in a rotor, balanced, and tip ground. No damage from the tip-grinding operation was observable. The blades were then assembled in a ground based test engine which was scheduled to run for 1500 "C" cycles. A typical "C" cycle is shown in Figure 75.

Examination of the blades after 16 hr of engine check-out (Figure 76) revealed some coating damage on all of the TBC blades. The damage was restricted to the upper third of the leading edge on the airfoils and appeared to be small pock marks in the ceramic layer. The damage is believed to be due to the impact of material lost by some developmental shrouds in the preceding stage of the high-pressure turbine. Subsequent boroscope examination of the blades during the test showed no observable progression of the damage along the leading edge after 316 "C" cycles. However, examination after 476 "C" cycles (Figure 77) showed slight additional ceramic coating loss which may possibly be attributed to further foreign object damage, but it was still limited to the upper third of the leading edge. No coating loss was observed at any other location on the blades. The test was terminated after 626 "C" cycles because of engine failure initiated in the preceding stage of the high pressure turbine.

TABLE XIV

HIGH CYCLE FATIGUE TEST RESULTS

Serial Number	Tip Deflection, (mm)	Cycles to Fail
H3447	2.03	run out
32517	2.29	1.6×10^5
F5354	2.03	9.6×10^6
M2906	1.78	1.8×10^6
M8771	1.52	run out
F7988	1.78	run out
M8528	2.03	2.6×10^5
L9019	1.78	run out

All of the second-stage blades (those with and without TBC) were severely damaged when the test engine failed. Extensive loss of blade material occurred at the leading edge and blade tip. In addition, considerable impact damage was noted on the suction side of the airfoils near the leading and trailing edges. The ceramic coating losses from the remaining airfoil surface were about 10 to 15% on the pressure side (concave) and 20 to 30% on the suction side (convex). The NiCrAlY, however, remained intact over nearly all of the remaining airfoil surface.

5.4.2 Microstructural Examination

The photomicrograph in Figure 78 shows the coating damage which was sustained on the suction side of the airfoil near the leading edge. Nearly all of the ceramic coating is gone, and the NiCrAlY layer is fragmented and detached because of impact damage. The surface deposit in this micrograph covered all of the pressure side of the airfoil and about half of the suction side. The deposit was analyzed to be Rene'80. The coating microstructure in the area which had not sustained impact damage is shown in Figure 79. The coating is in very good condition and shows no evidence of cracking or separation. The coating microstructure on the pressure side of the airfoil near the blade tip is shown in Figure 80. Here, the ceramic layer had begun to separate from the bond coat and, in fact, some coating spallation had occurred in this area on all of the engine-tested blades.

Formation of an oxide layer at the ceramic/NiCrAlY interface, as had been observed in laboratory specimens, was not generally apparent. This is probably due to the relatively short time (~166 hr) at elevated temperature in the engine test. However, in some areas near the leading and trailing edges, a thicker oxide layer was observed at the ceramic/NiCrAlY interface. These areas experienced much higher temperature than the bulk of the airfoil as evidenced by a variation in color of the Rene'80 deposit on the TBC surface.

X-ray diffraction analysis of the ceramic coating from an engine-run blade showed the 8 w/o Y_2O_3-ZrO_2 to be mostly tetragonal, with a small percentage of the monoclinic phase.

5.4.3 Conclusions from Engine Test

Component high-cycle fatigue (HCF) testing showed that the presence of the TBC on CF6-50 stage 2 HPT blades did not significantly degrade the HCF properties when compared to the uncoated blade.

The impact damage which resulted in some ceramic coating loss during the early part of the engine test emphasized the need to improve the foreign object damage resistance of TBCs if they are to be readily accepted as turbine component coatings.

Evaluation of the engine-run blades with thermal barrier coating was limited because of extensive damage which resulted when the engine failed. Despite the abnormally severe conditions, the TBC remained adherent over most of the airfoil and platform, except in areas where severe impact had occurred.

6.0 CONCLUSIONS

1. The MCrAlY bond coatings deposited by a low pressure plasma deposition system give more reproducible and better thermal barrier coating life compared with the case of air plasma spraying.

2. The most durable thermal barrier coating system investigated in this study was an 8 w/o Y_2O_3-ZrO_2 ceramic coating deposited in air and a Ni-22Cr-10Al-1Y bond layer deposited by a low pressure plasma deposition process.

3. Interdiffusion of the MCrAlY layer and the substrate is substantial at elevated temperatures and may be a major degradation mechanism leading to TBC failure.

4. The durability of thermal barrier coatings is limited by degradation of adhesion by environmental interactions rather than by mechanical stress per se.

5. Design analysis shows undegraded thermal barrier coatings can withstand higher compressive and tensile strains without spallation than would ever be expected from a simple consideration of thermal expansion and typical ceramic failure strains.

6. Spallation of the thermal barrier coating from both the leading and trailing edge areas results in an increase of transient thermal stresses. Such spallation, if it occurs, has the potential to reduce blade life below that of an uncoated blade, even though 100% coolant flow was maintained.

7. The cooling flow to a CF6-50 stage 2 HPT blade coated with 0.25 mm (0.010 in.) of thermal barrier coating can be reduced to about 50% of the original value and still maintain the bulk metal temperature of the uncoated airfoil.

8. Thermal barrier coatings can remain adherent when used in an engine. However, the ability of TBCs to resist foreign object damage in service needs further improvement.

7.0 RECOMMENDATIONS

Because thermal barrier coatings offer an important technology for improved aircraft turbine engines, and in view of the insights gained in this work we offer the following recommendations:

(1) The design/materials community interface is needed to achieve maximum benefit.

(2) Efforts should be undertaken to define a TBC failure law in terms of:

   (a) the constituent materials and their microstructures,
   (b) the strains experienced by the part,
   (c) the temperature, service cycles, and environment to which the coatings are exposed, and
   (d) geometric effects such as free edges, regions of high curvature, etc.

(3) The effect of process variables should be more carefully defined, such as the effects of powder variations and environment during application of the coatings.

(4) Bond-coat compositions offering even higher temperature capability and longer life should be investigated.

(5) Factors affecting and improving the impact resistance of the oxide layer should be studied.

8.0 REFERENCES

1. E.S. Stepka, C.H. Liebert, and S. Stecura, "Summary of NASA Research on Thermal-Barrier Coatings", NASA TMX-73584, 1977.

2. C.H. Liebert and E.S. Stepka, "Potential Use of Ceramic Coating as a Thermal Insulation on Cooled Turbine Hardware", NASA TMX-B425, 1976.

3. S. Timoshenko, Strength of Materials-I, Robert E. Kreiger Publishing Co., NY, 1976, p. 217.

4. M. Hansen, Constitution of Binary Alloys, McGraw-Hill, NY, 1958, p. 543.

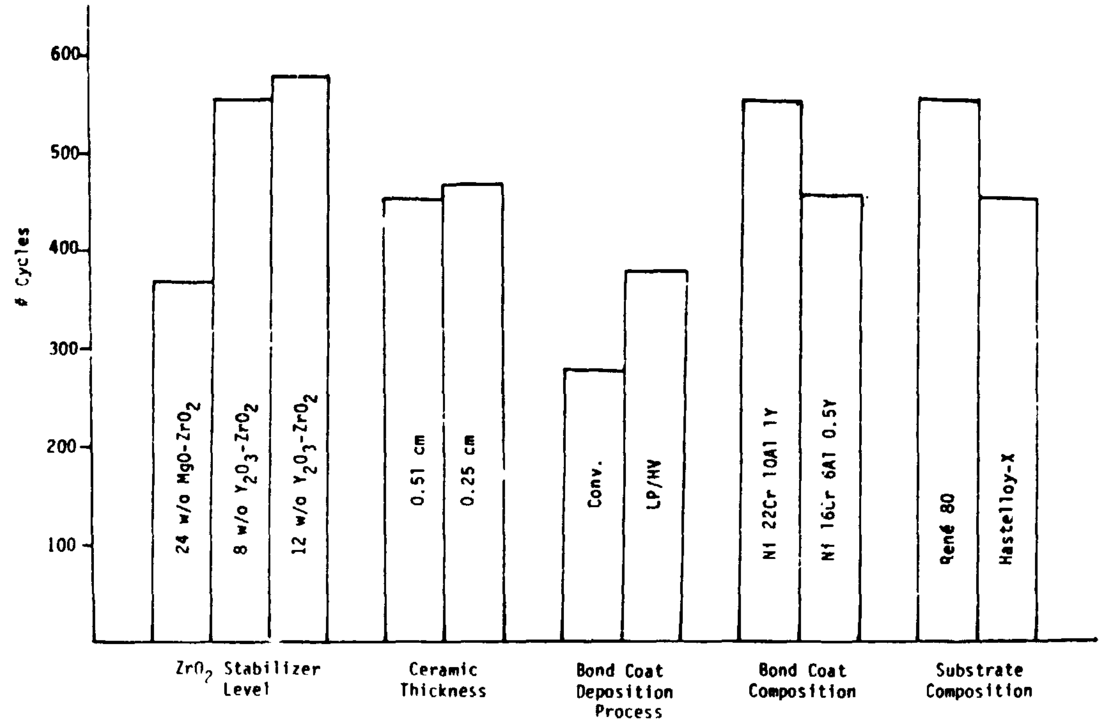

Figure 1 Average lifetimes of TBC variations investigated. (Note that at 500 cycles the severity of the test was markedly increased by increasing the maximum temperature from 1000 to 1100°C.

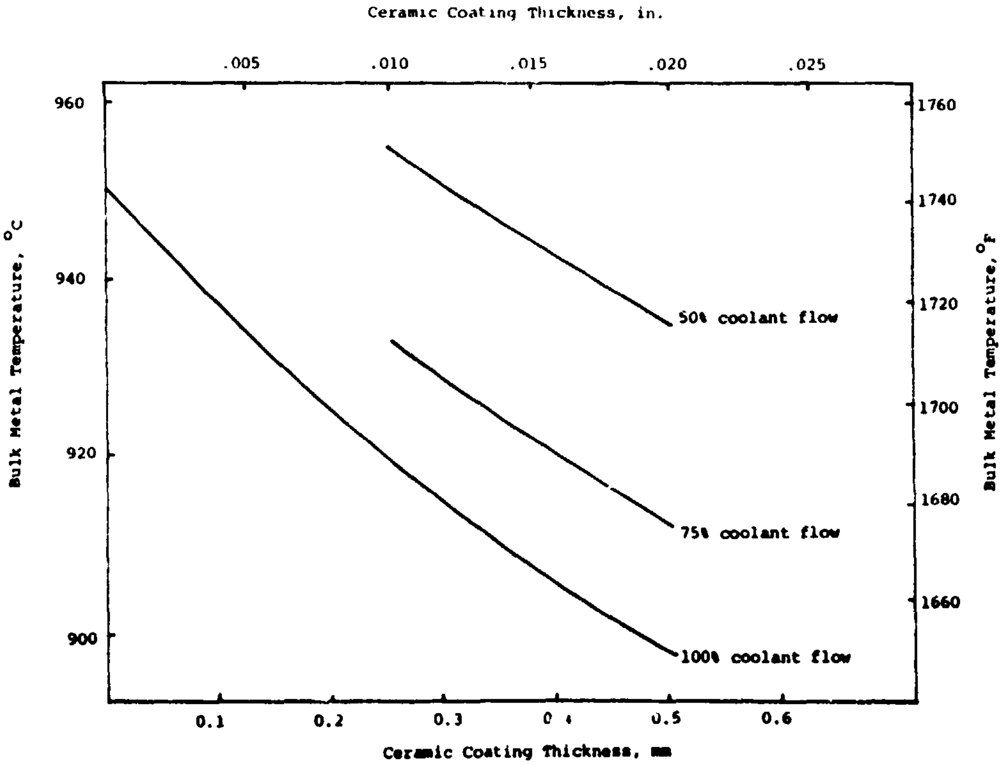

Figure 2 Variation of the average bulk metal temperature of a CF6-50 stage 2 HPT blade with ceramic coating thickness and percent of normal coolant flow.

Figure 3 CF6-50 Stage 2 High Pressure Turbine Blades coated with 0.13 mm (0.005") NiCrAlY and 0.25 mm (0.010") 8 w/o Y_2O_3-ZrO_2

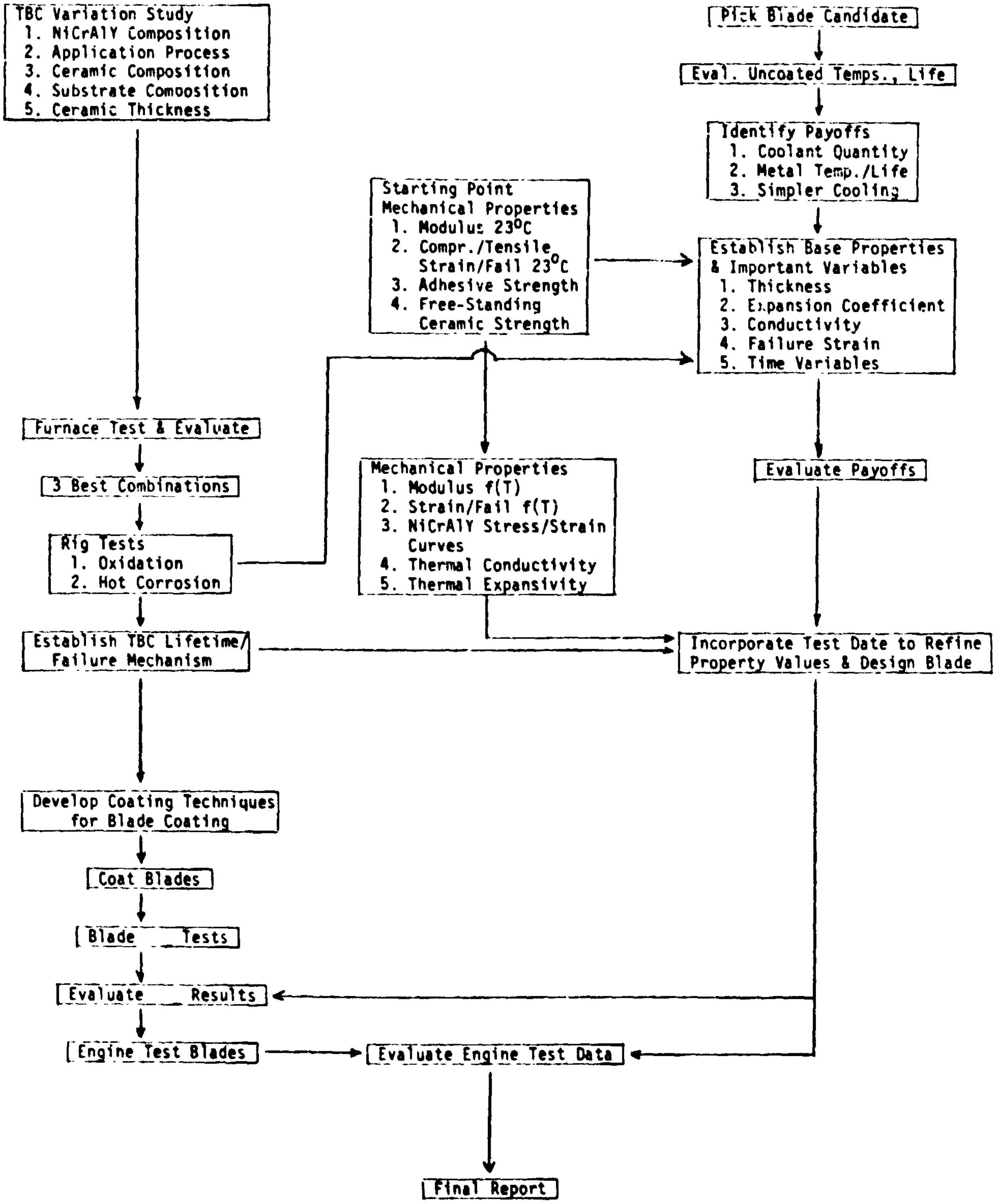

Figure 4 Flow Diagram of the TBC Program

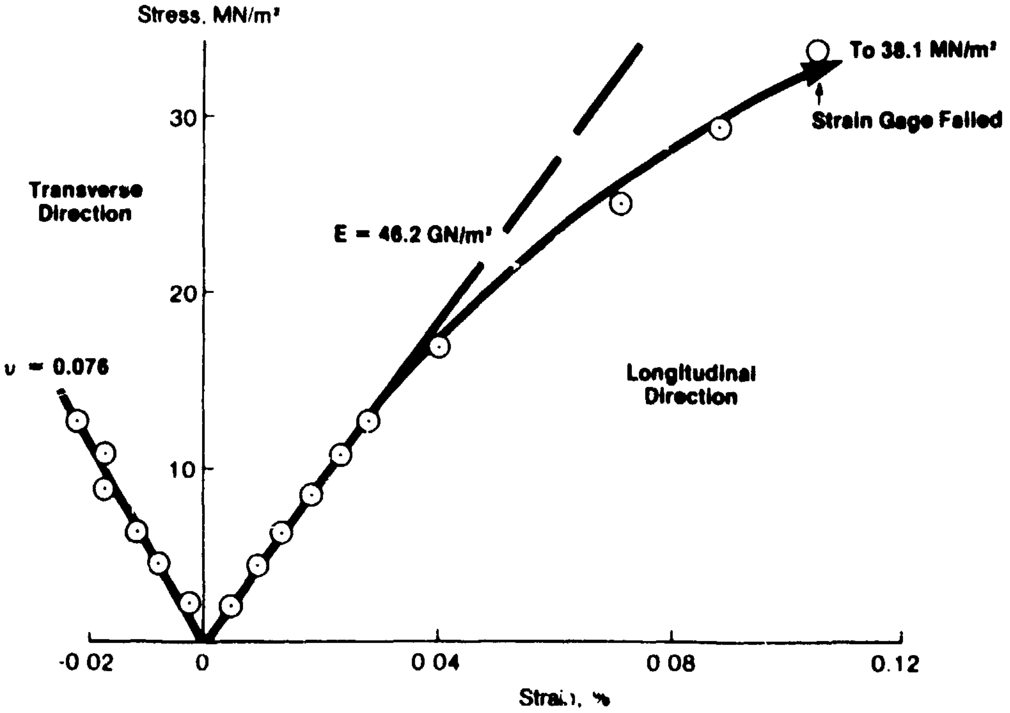

Figure 5 Stress-strain behavior of $MgO\text{-}ZrO_2$

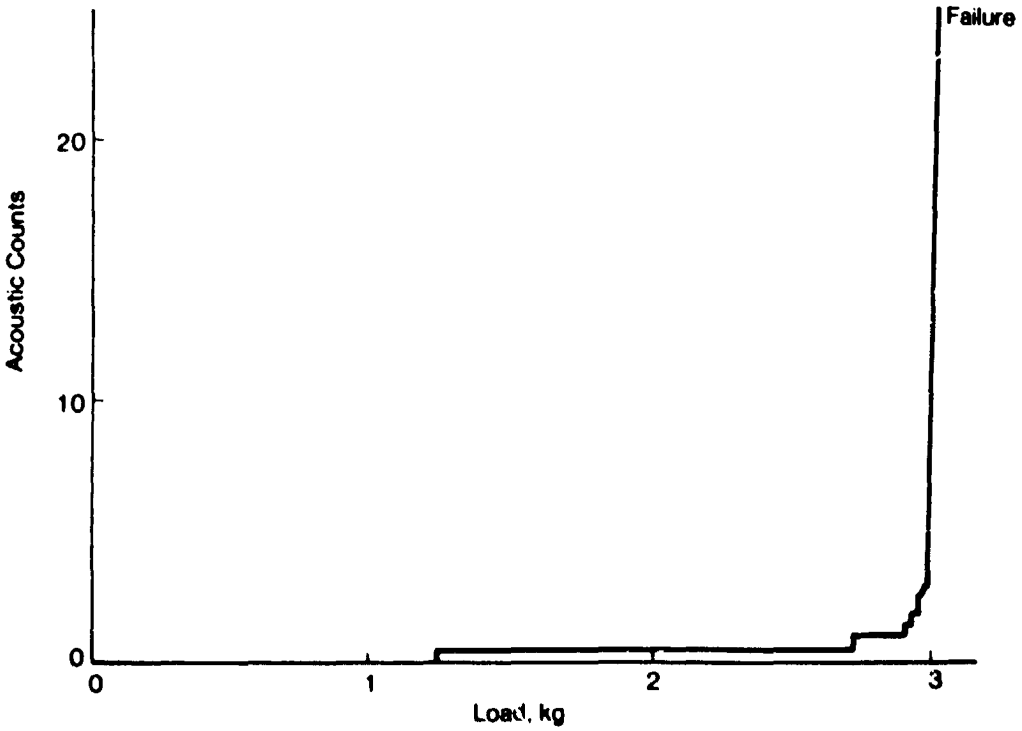

Figure 6 Acoustic emission during straining of free-standing $MgO\text{-}ZrO_2$

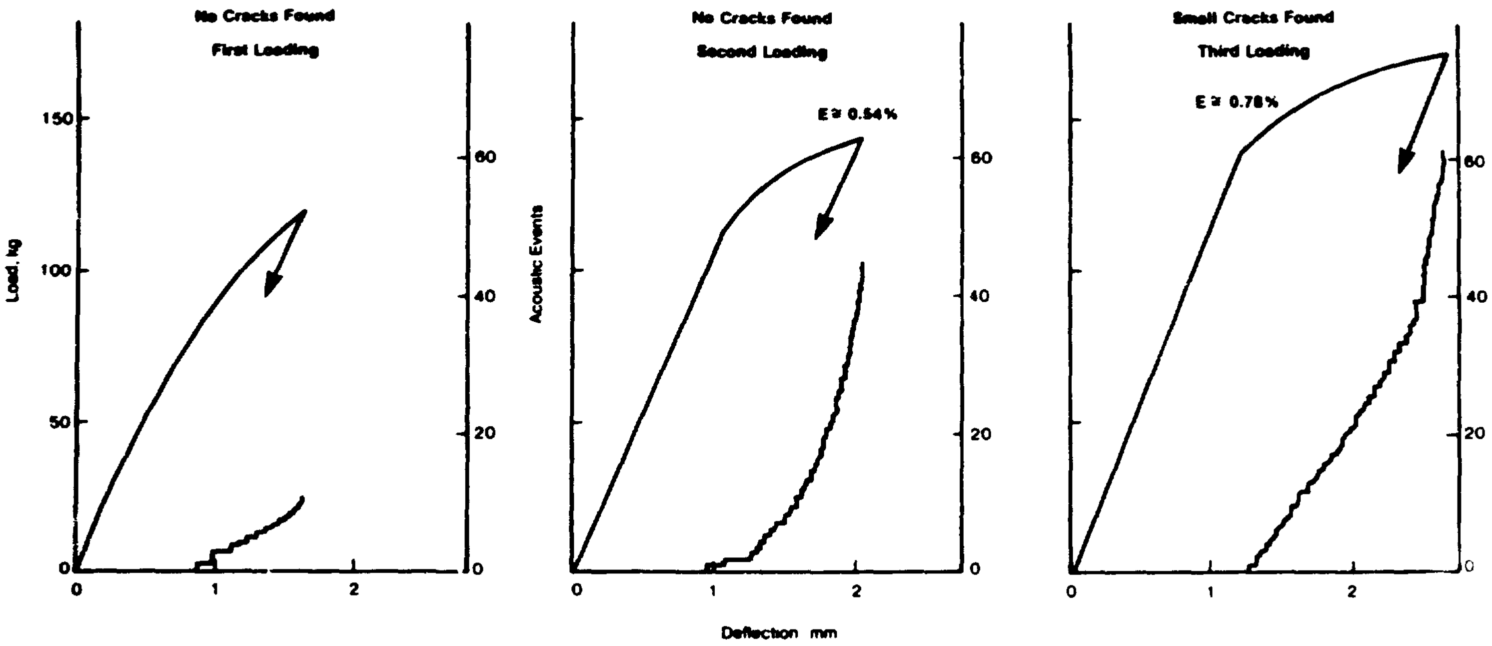

Figure 7 Acoustic emission of MgO-ZrO_2 on substrate upon repeated straining.

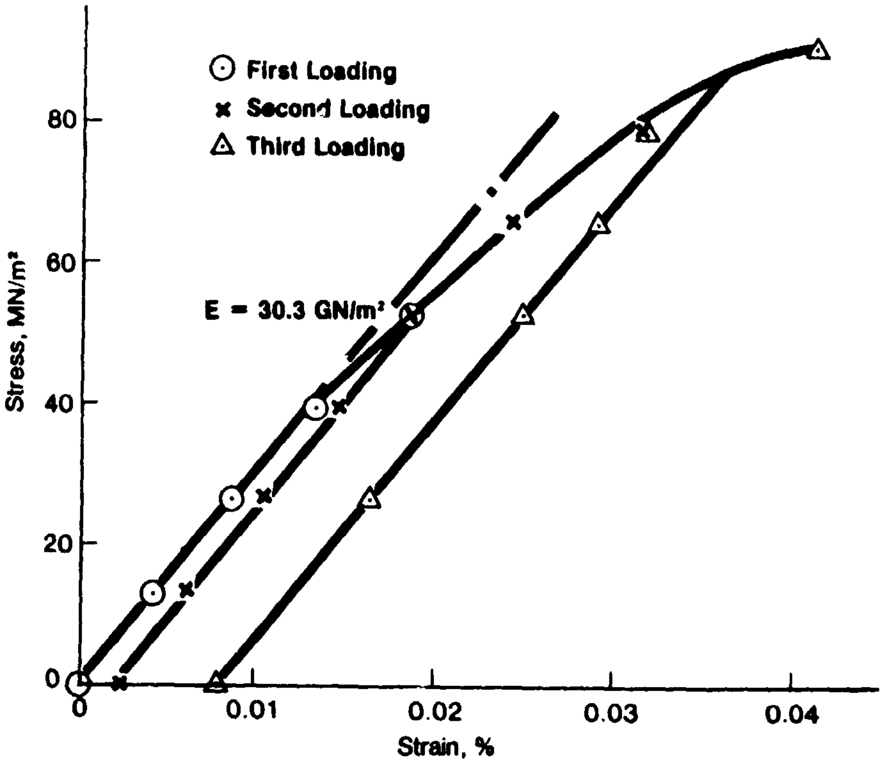

Figure 8 Stress strain behavior of MgO-ZrO_2 on substrate upon repeated tensile loading.

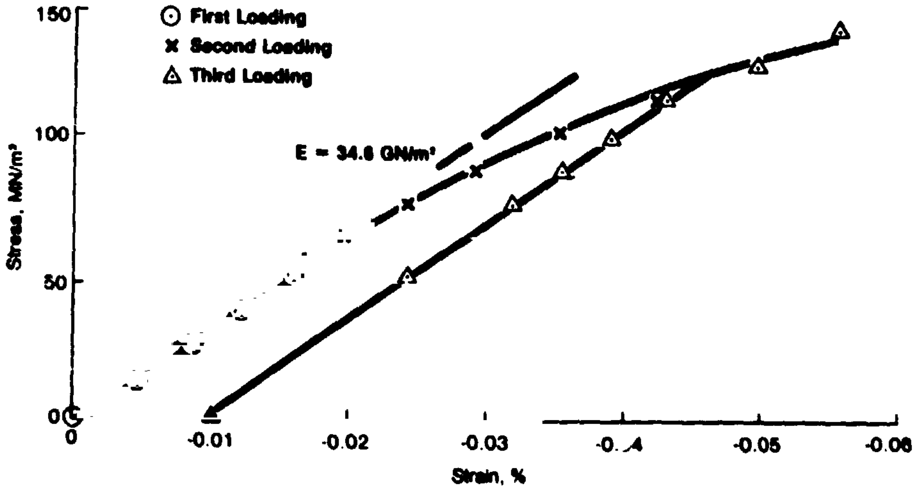

Figure 9 Stress strain behavior of MgO-ZrO_2 on substrate upon compressive loading.

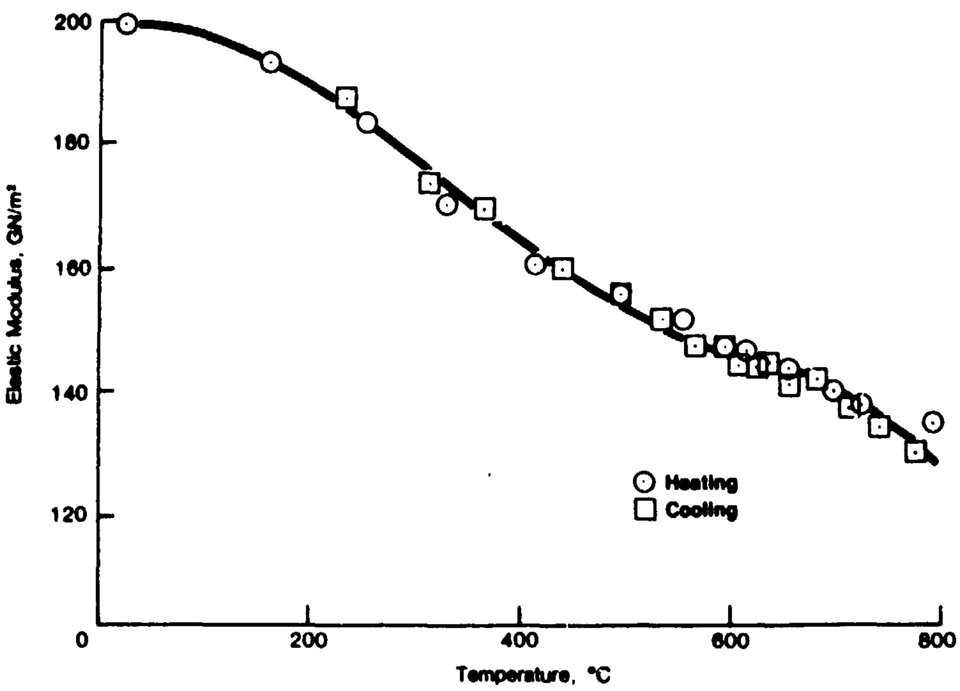

Figure 10 Elastic modulus of Ni-22Cr-10Al-1Y as a function of temperature.

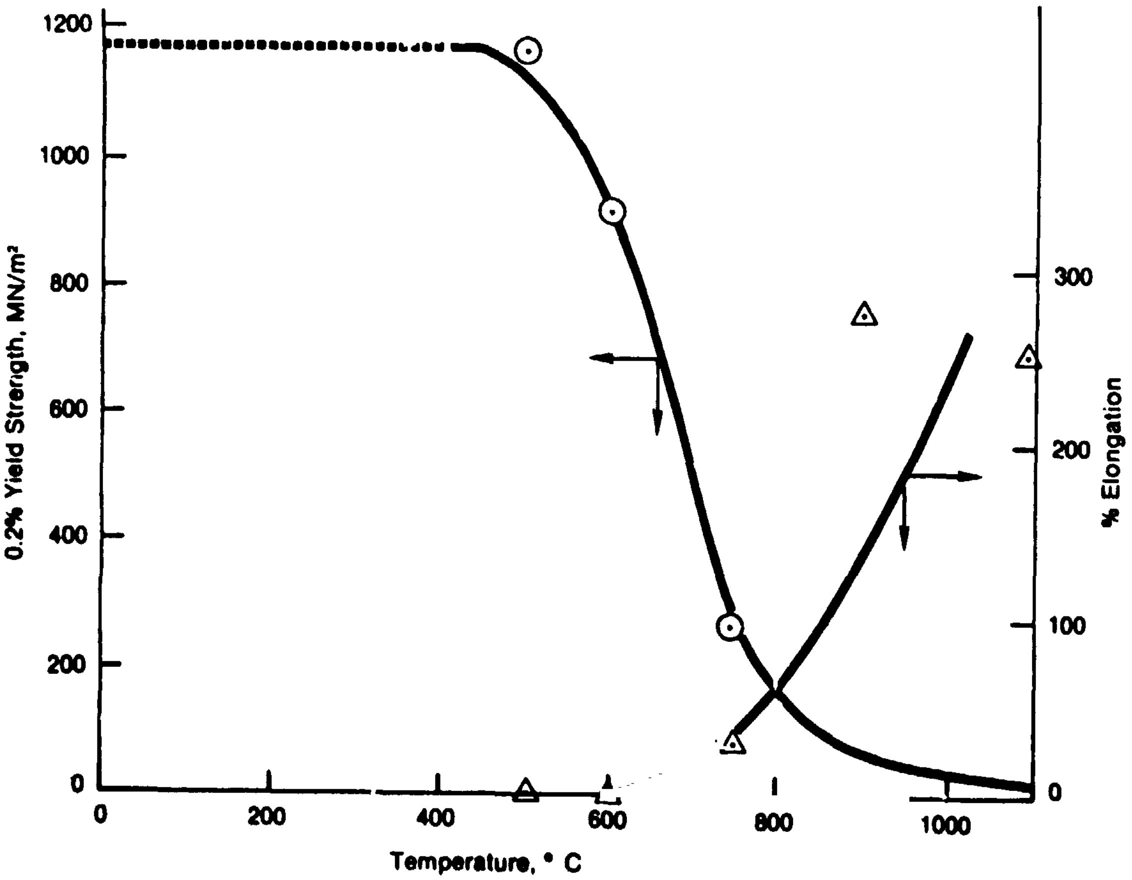

Figure 11 Yield strength and ductility of Ni-22Cr-10Al-1Y as a function of temperature.

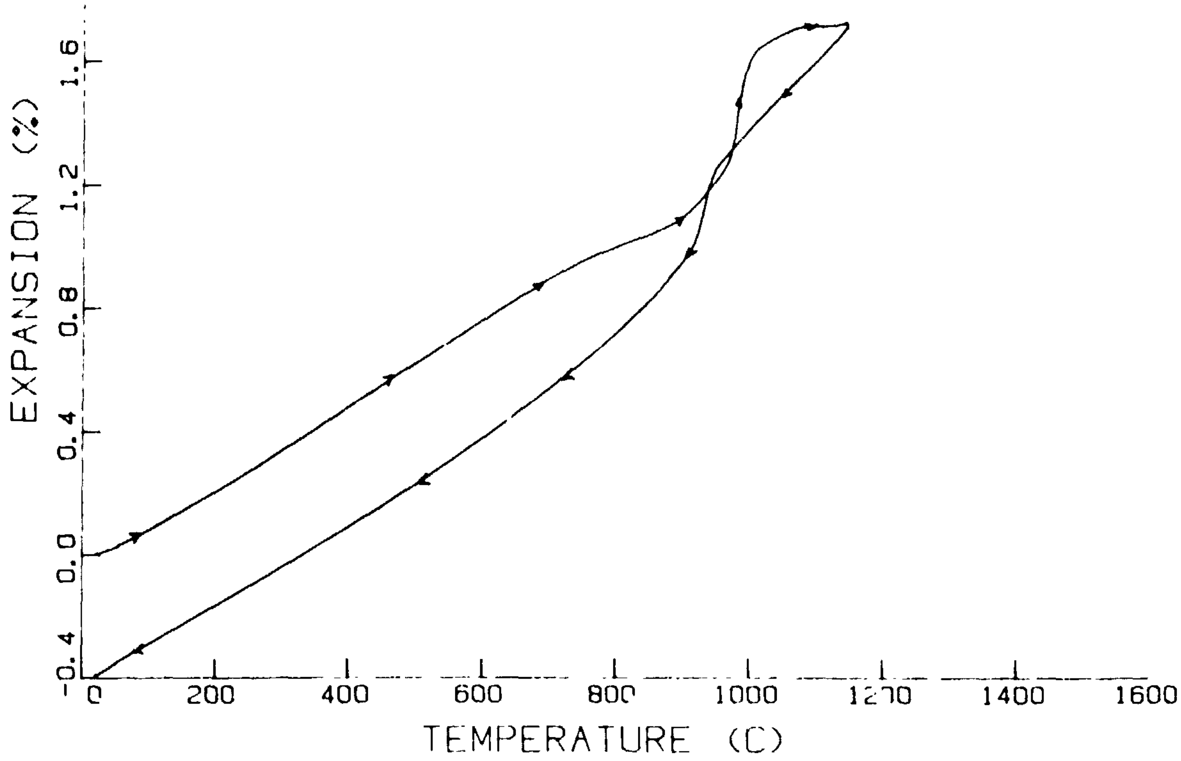

Figure 12 Thermal expansion of plasma sprayed Ni-22Cr-10Al-1Y during initial heat up and cooling.

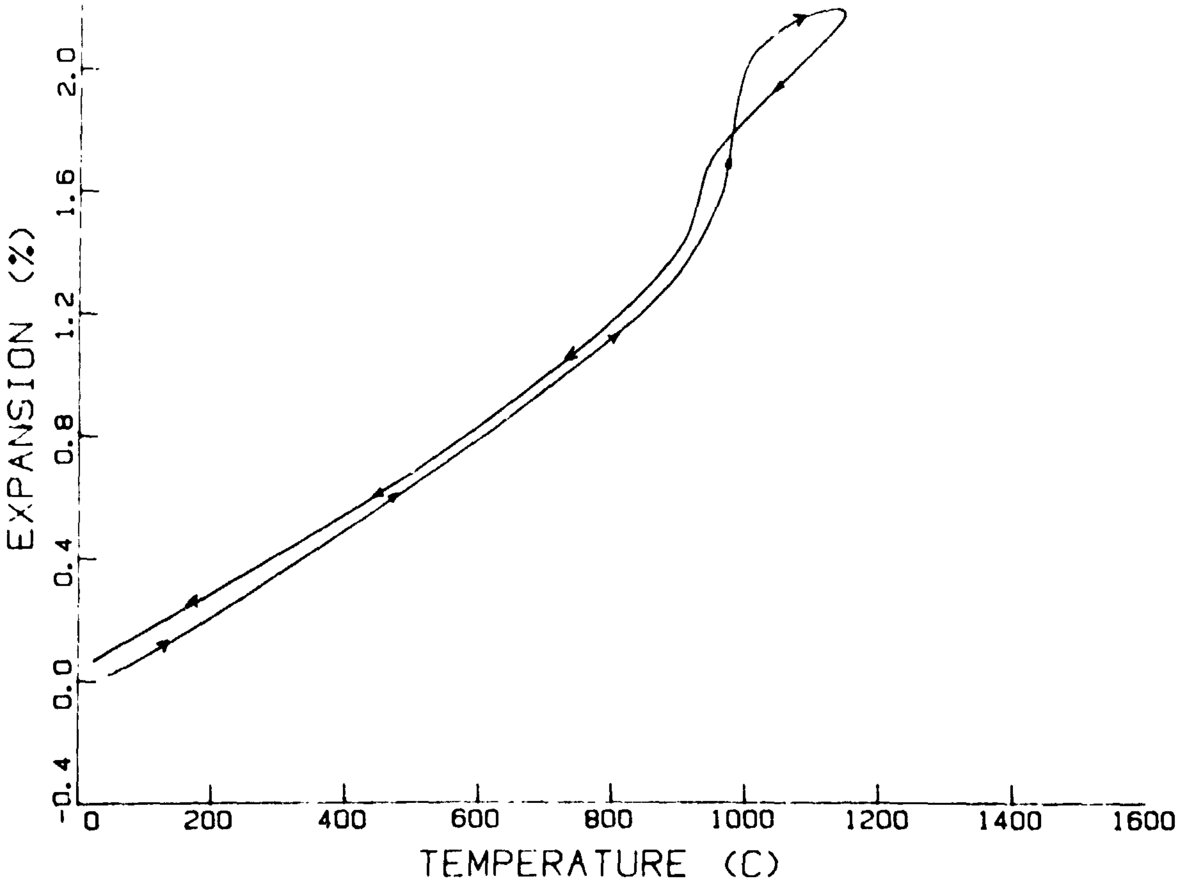

Figure 13 Thermal expansion of plasma sprayed Ni-22Cr-10Al-1Y during second cycle of heating and cooling.

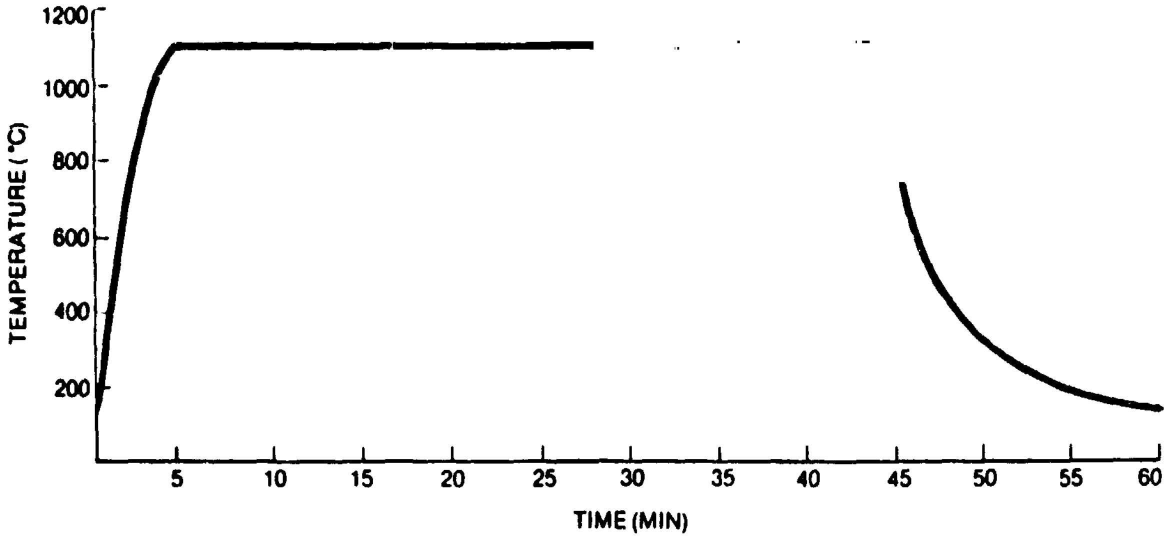

Figure 14 Furnace temperature cycle used to test TBC specimens.

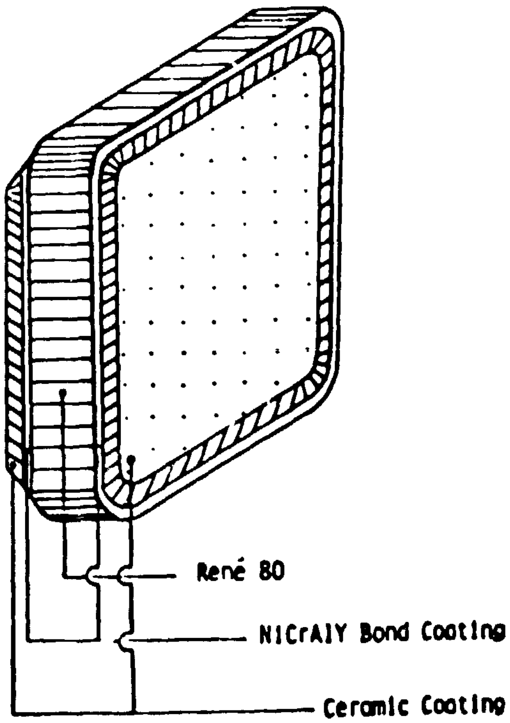

Figure 15 Detail of Double Coated Test Coupon

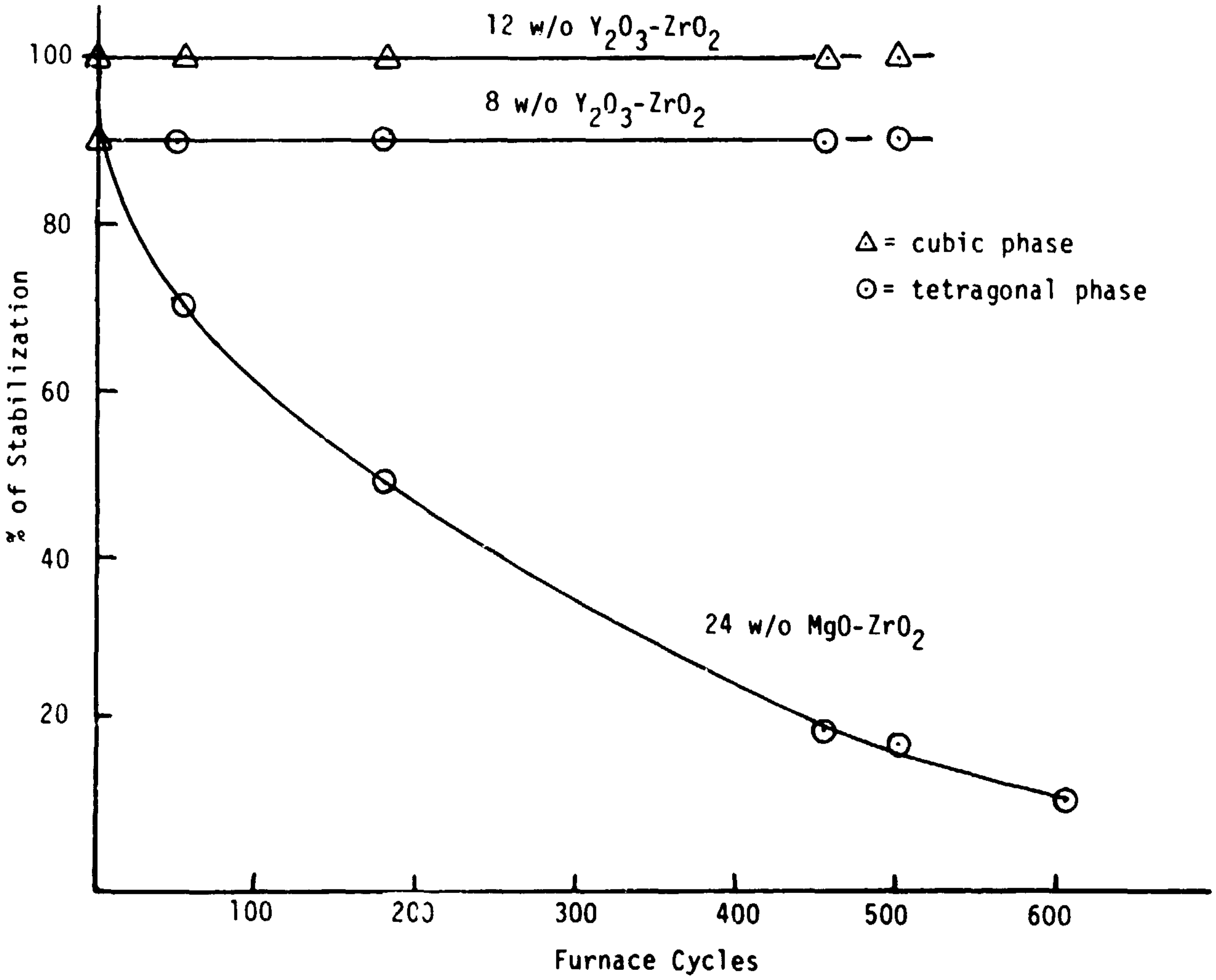

Figure 16 Dependence of phase stability of plasma sprayed coatings on temperature cycling.

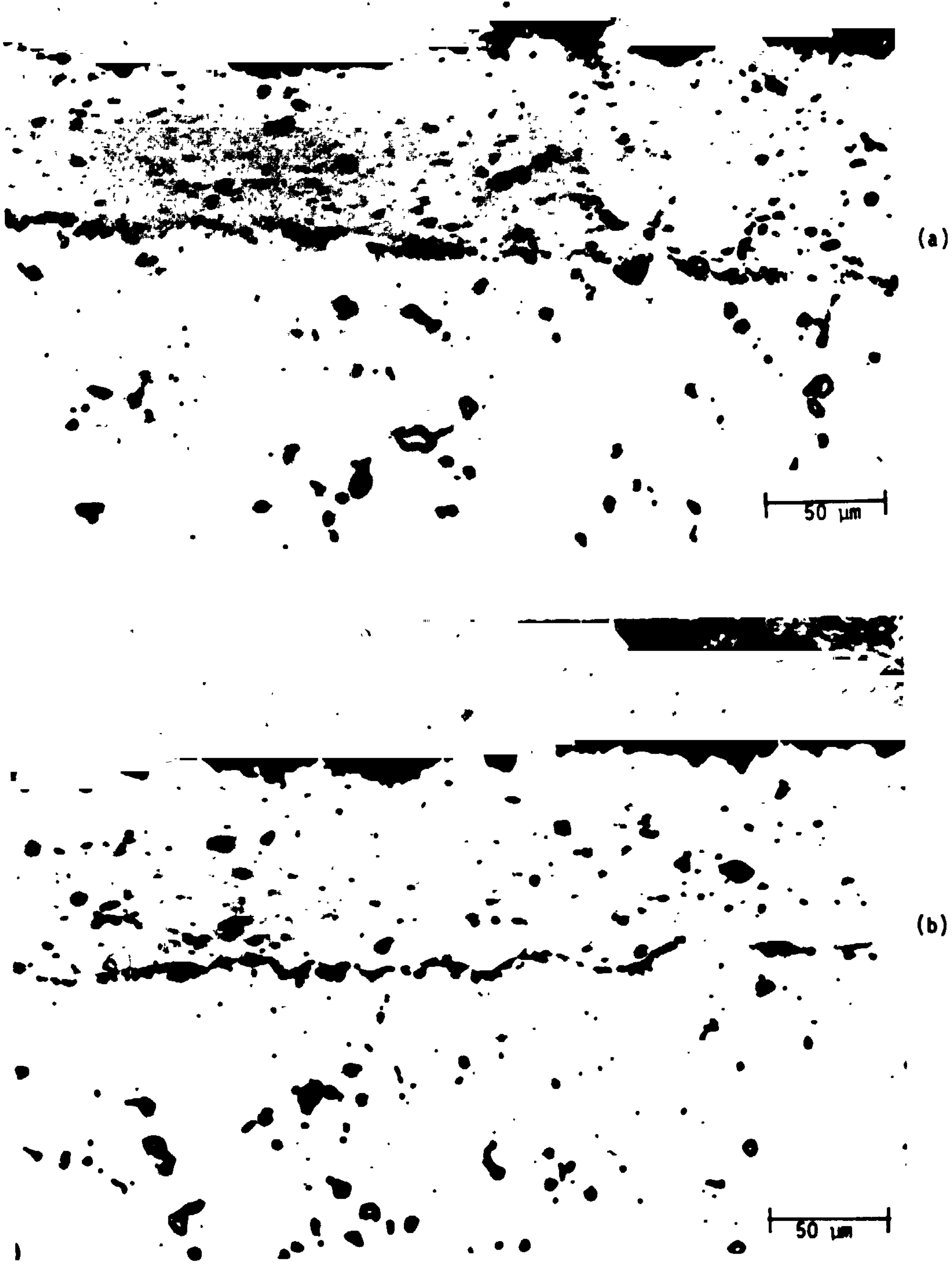

Figure 17 Micrographs of ceramic coatings over LP/HV-applied Ni-22Cr-10Al-1Y coatings on a 1.59 mm thick Rene'80 casting before cyclic oxidation testing. (a) Side No. 1 - 24 w/o MgO-ZrO_2 ceramic; (b) Side No. 2 - 8 w/o Y_2O_3-ZrO_2

ORIGINAL PAGE IS
OF POOR QUALITY

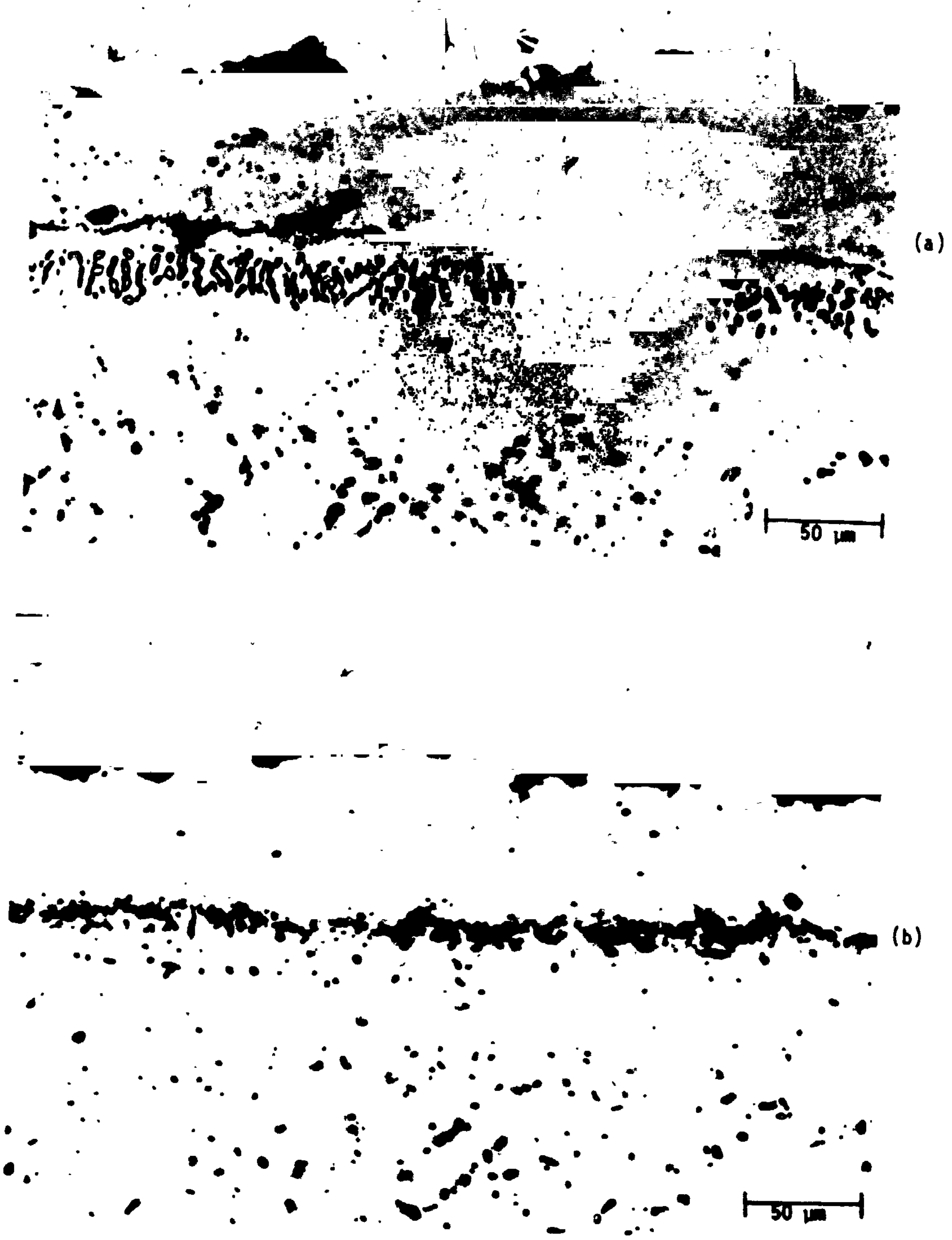

Figure 18 Micrographs of LP/HV-applied Ni-22Cr-10Al-1Y coating on Rene'80 substrate after 658 cycles of furnace tests. (a) Side No. 1 - 24 w/o $MgOZrO_2$ coating initiated failure at 510 cycles, completely failed at 517 cycles; (b) Side No. 2 - 8 w/o Y_2O_3-ZrO_2, no spallation after 658 cycles.

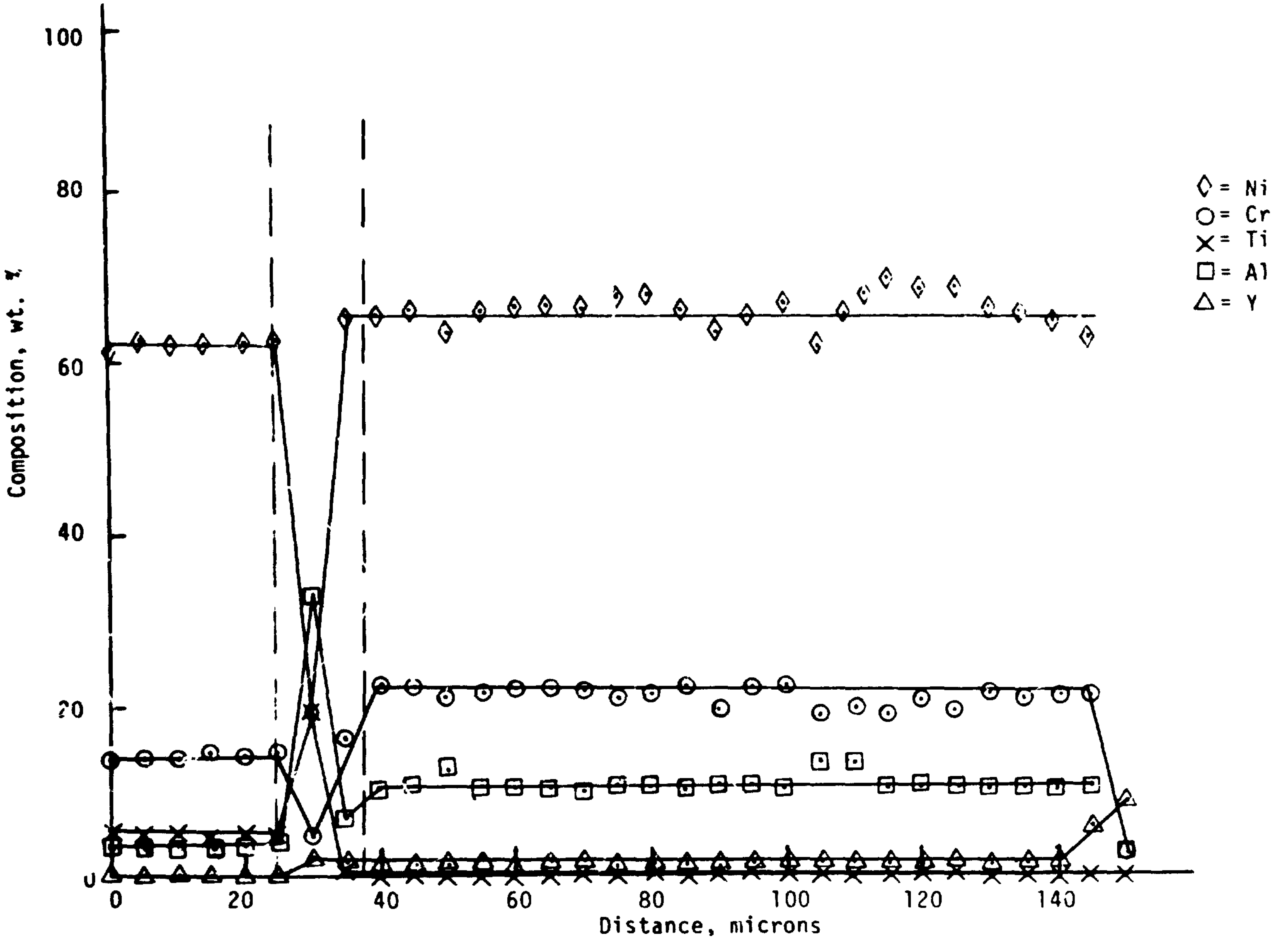

Figure 19 Elemental concentration profile of LP/HV-applied Ni-22Cr-10Al-1Y coating on Rene'80 before cyclic furnace testing.

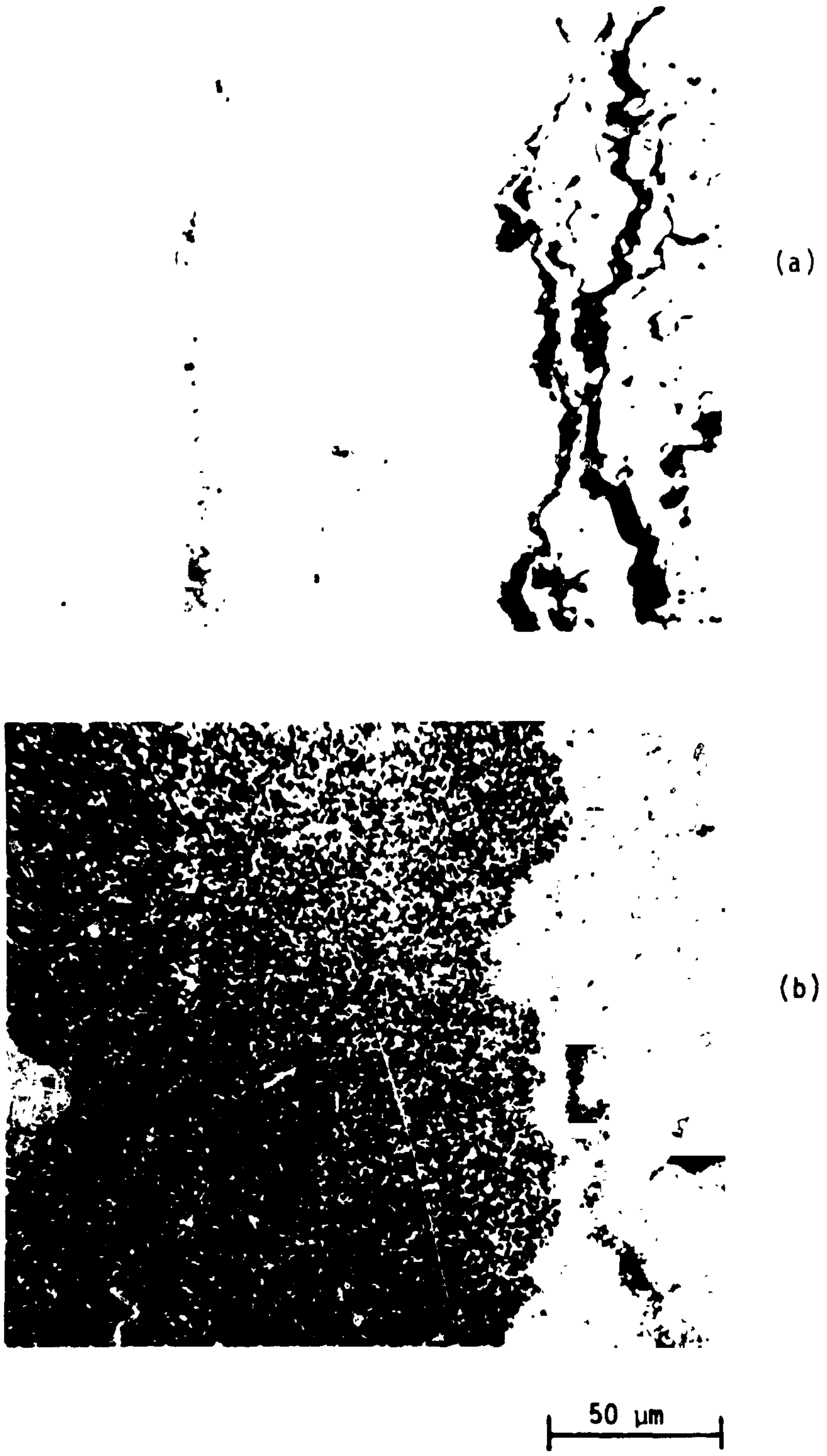

Figure 20 (a) Secondary electron image of LP/HV-applied Ni-22Cr-10Al-1Y and air-applied 12 w/o Y_2O_3-ZrO_2 coatings on Rene'80 substrate before cyclic furnace testing; (b) Al x-ray density map of area shown in (a).

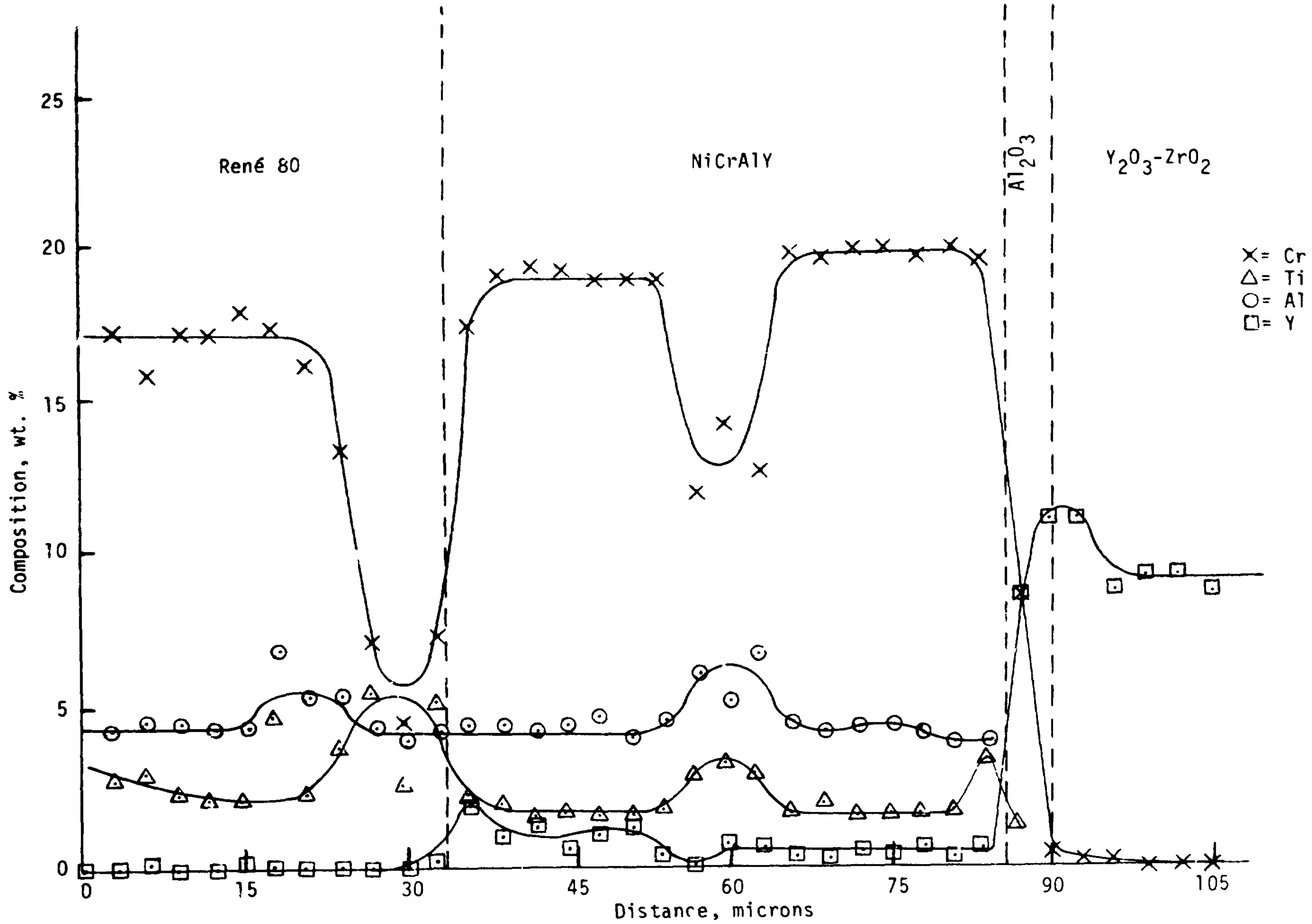

Figure 21 Elemental concentration profile of LP/HV-applied Ni-22Cr-10Al-1Y coating on Rene'80 after 67 hourly cycles of furnace testing with upper and lower temperature limits of 1100 and 140°C, respectively.

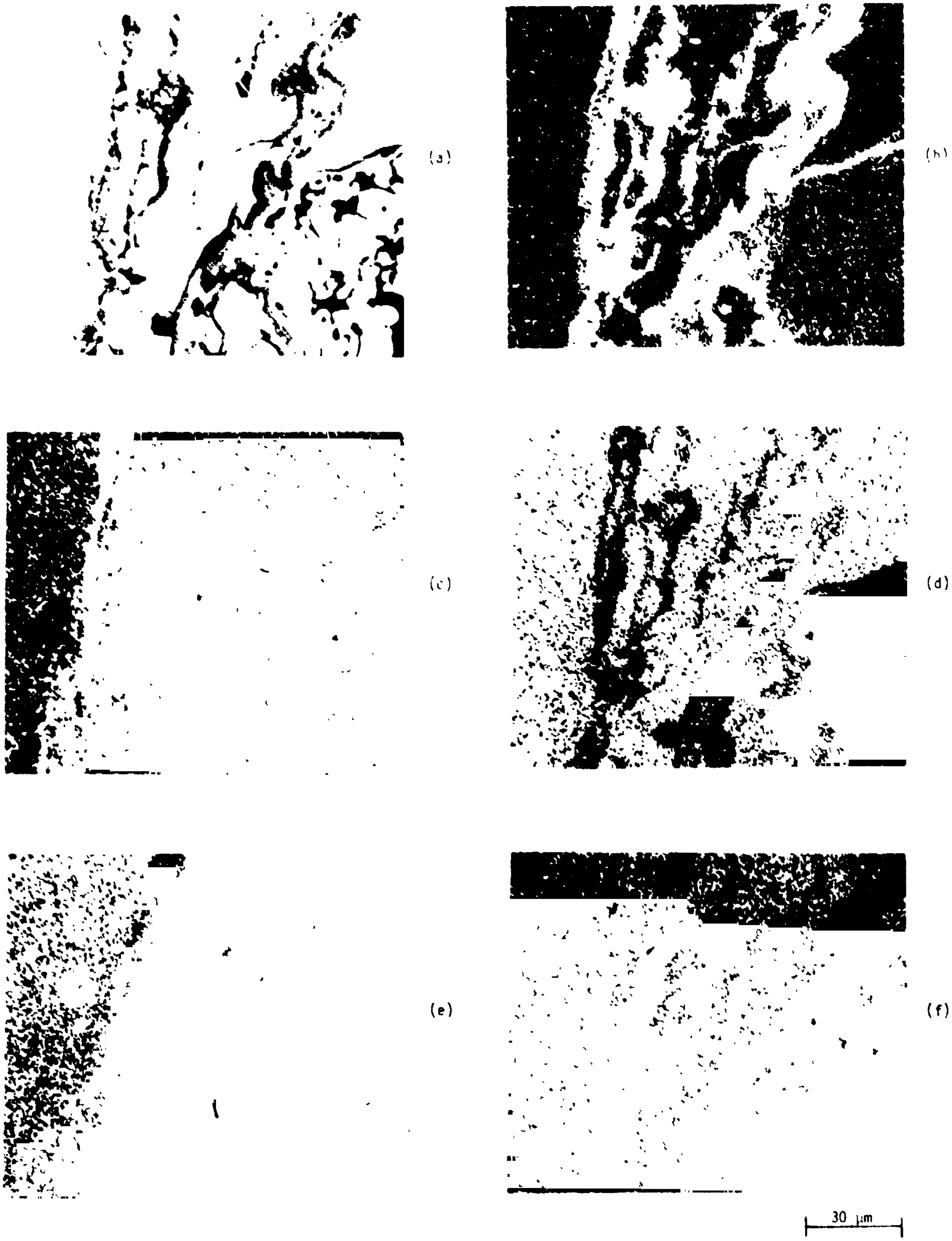

Figure 22 (a) Secondary electron image of air sprayed Ni-22Cr-10Al-1Y and air sprayed 12 w/o Y_2O_3-ZrO_2 coating on Rene'80 substrate after 67 hourly cycles of furnace testing with upper and lower temperature limits of 1100 and 140°C, respectively. Elemental x-ray density maps of (b) Al; (c) Ti; (d) Ni; (e) Co; (f) Cr.

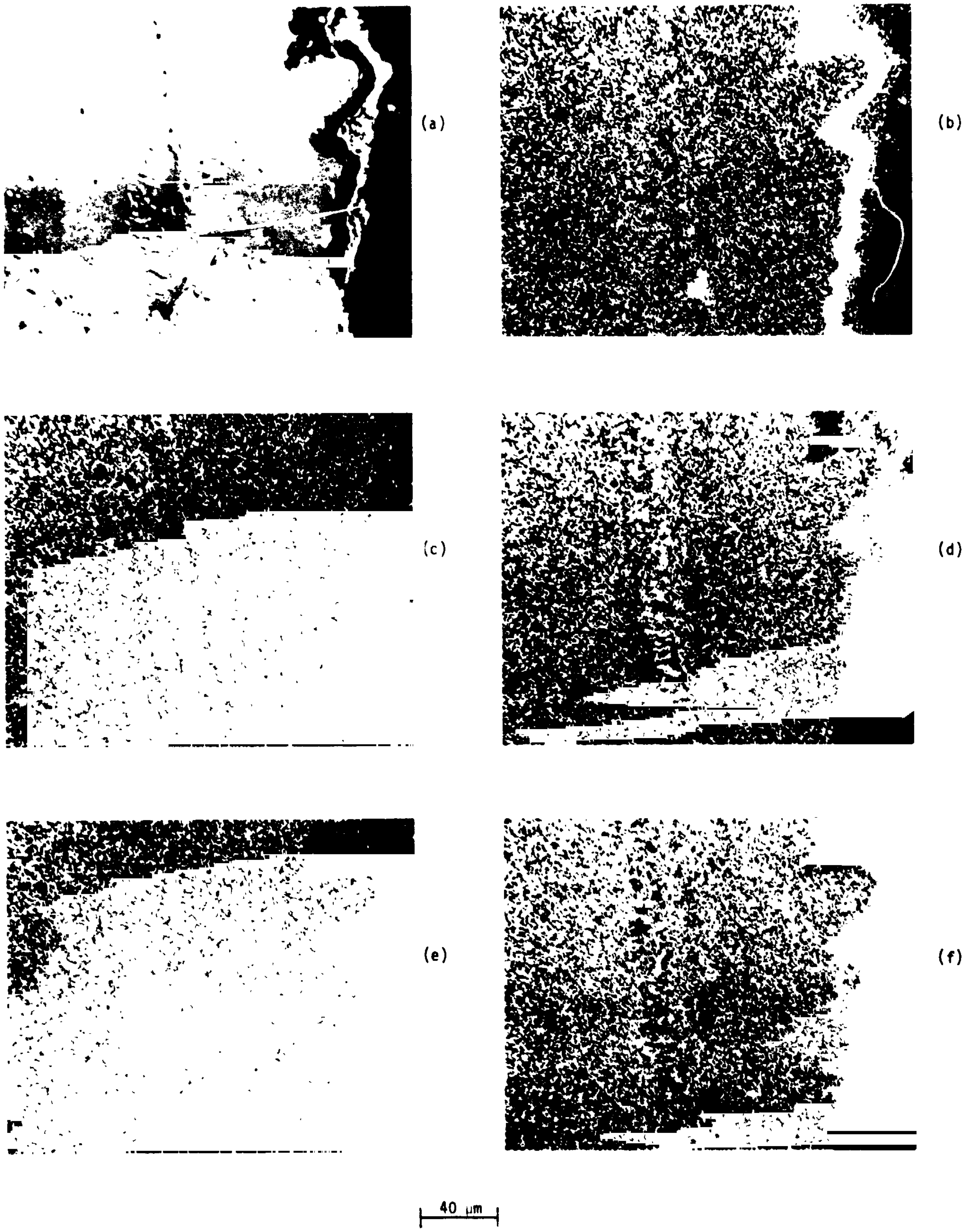

Figure 23 (a) Secondary electron image of LP/HV-applied Ni-22Cr-10Al-1Y and air sprayed 24 w/o MgO-ZrO_2 after 658 hours of cyclic furnace testing. Elemental x-ray density maps of (b) Al; (c) Ti; (d) Cr; (e) Co; (f) Ni.

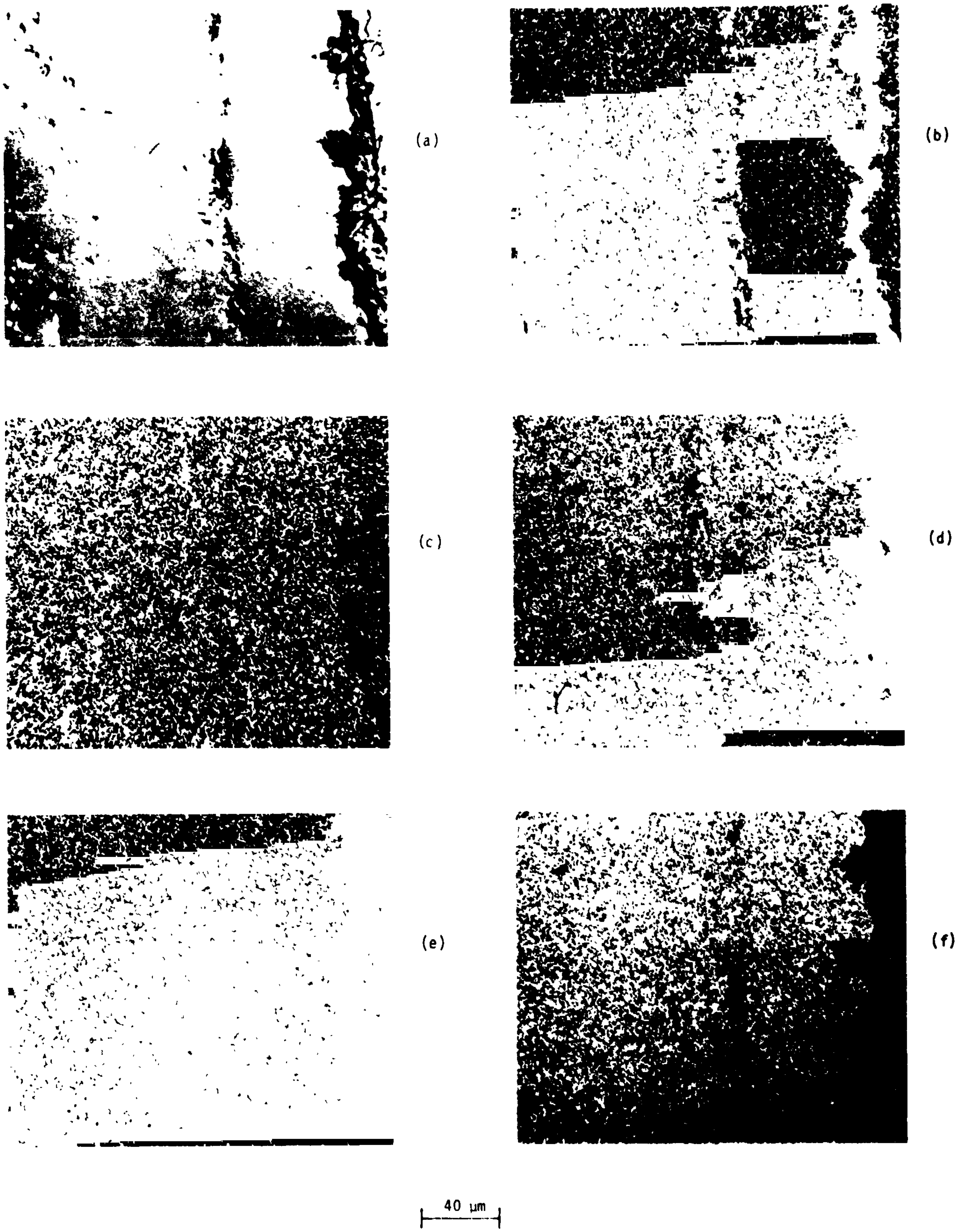

Figure 24 (a) Secondary electron image of LP/HV-applied Ni-22Cr-10Al-1Y and air sprayed 8 w/o Y_2O_3-ZrO_2 after 658 hours of cyclic furnace testing. Elemental x-ray density maps of (b) Al; (c) Ti; (d) Cr; (e) Co; (f) Ni.

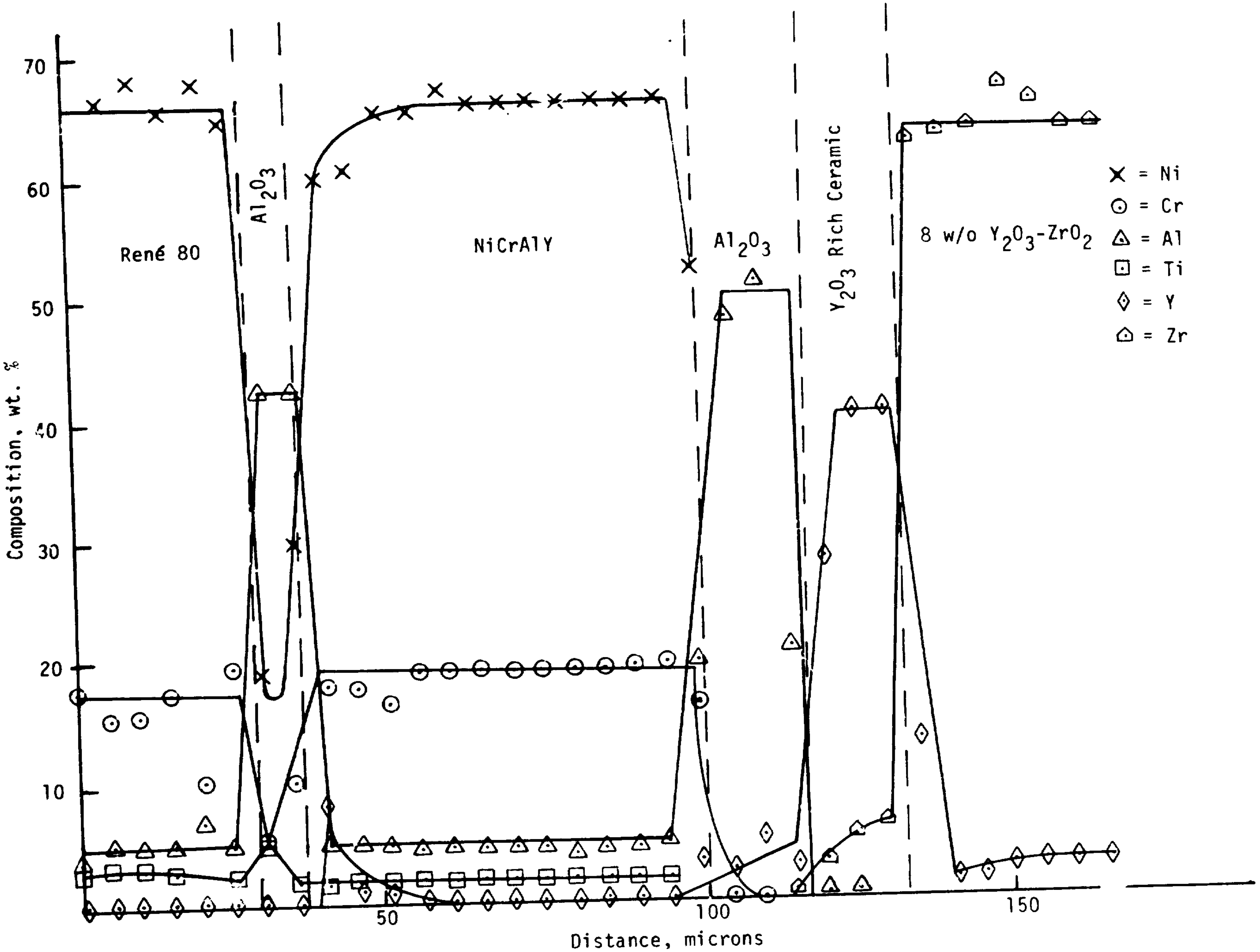

Figure 25 Elemental concentration profile of LP/HV-applied Ni-22Cr-10Al-1Y coating and air sprayed 8 w/o Y_2O_3-ZrO_2 coating on Rene'80 after 658 oxidation cycles.

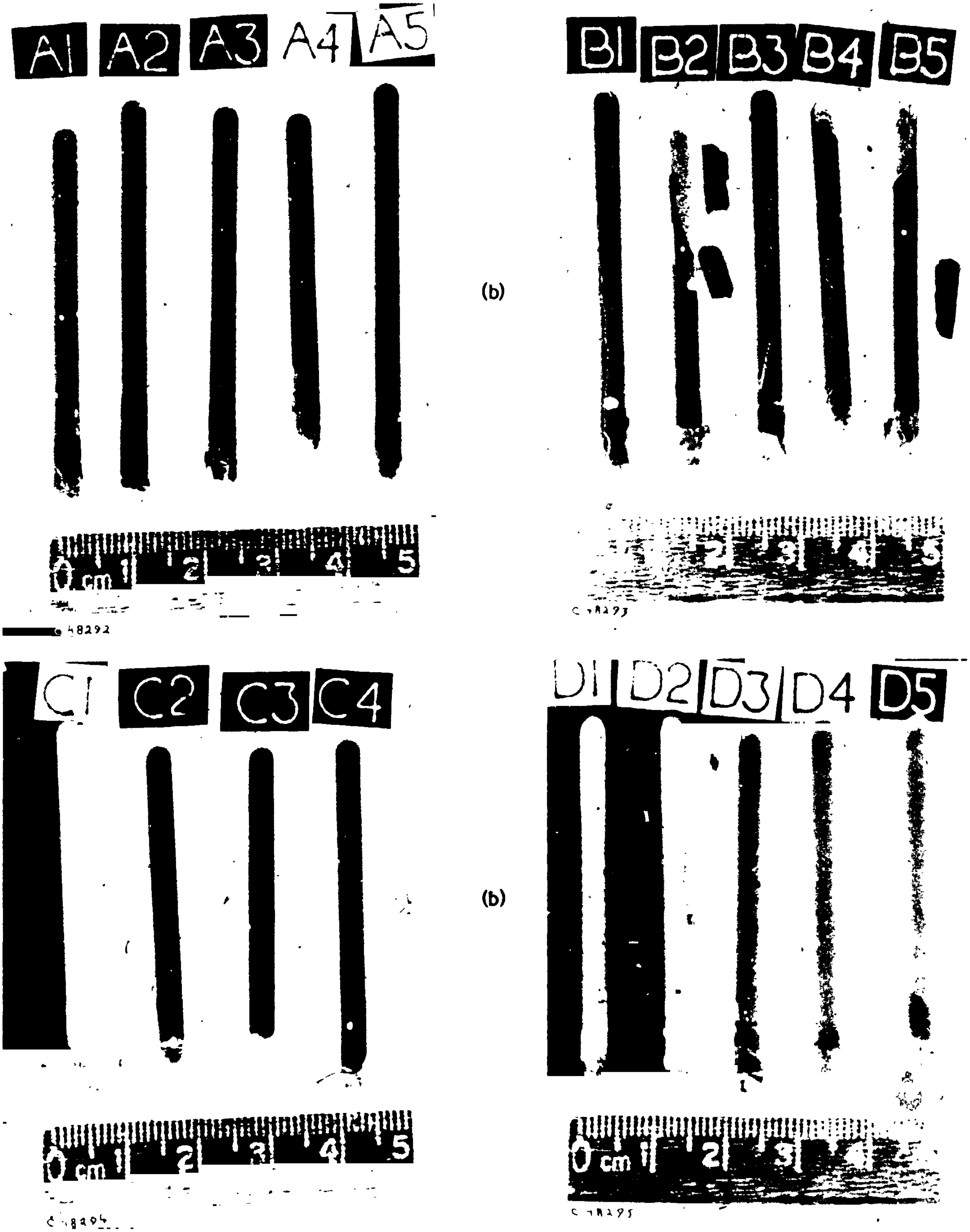

Figure 26 After-test condition of hot corrosion test specimens with coating systems as follows: (a) A (8 w/o Y_2O_3-ZrO_2, LP/HV); (b) B (12 w/o Y_2O_3-ZrO_2, LP/HV); (c) C (8 w/o Y_2O_3-ZrO_2, air); (d) D (8 w/o Y_2O_3-ZrO_2, air, NASA)

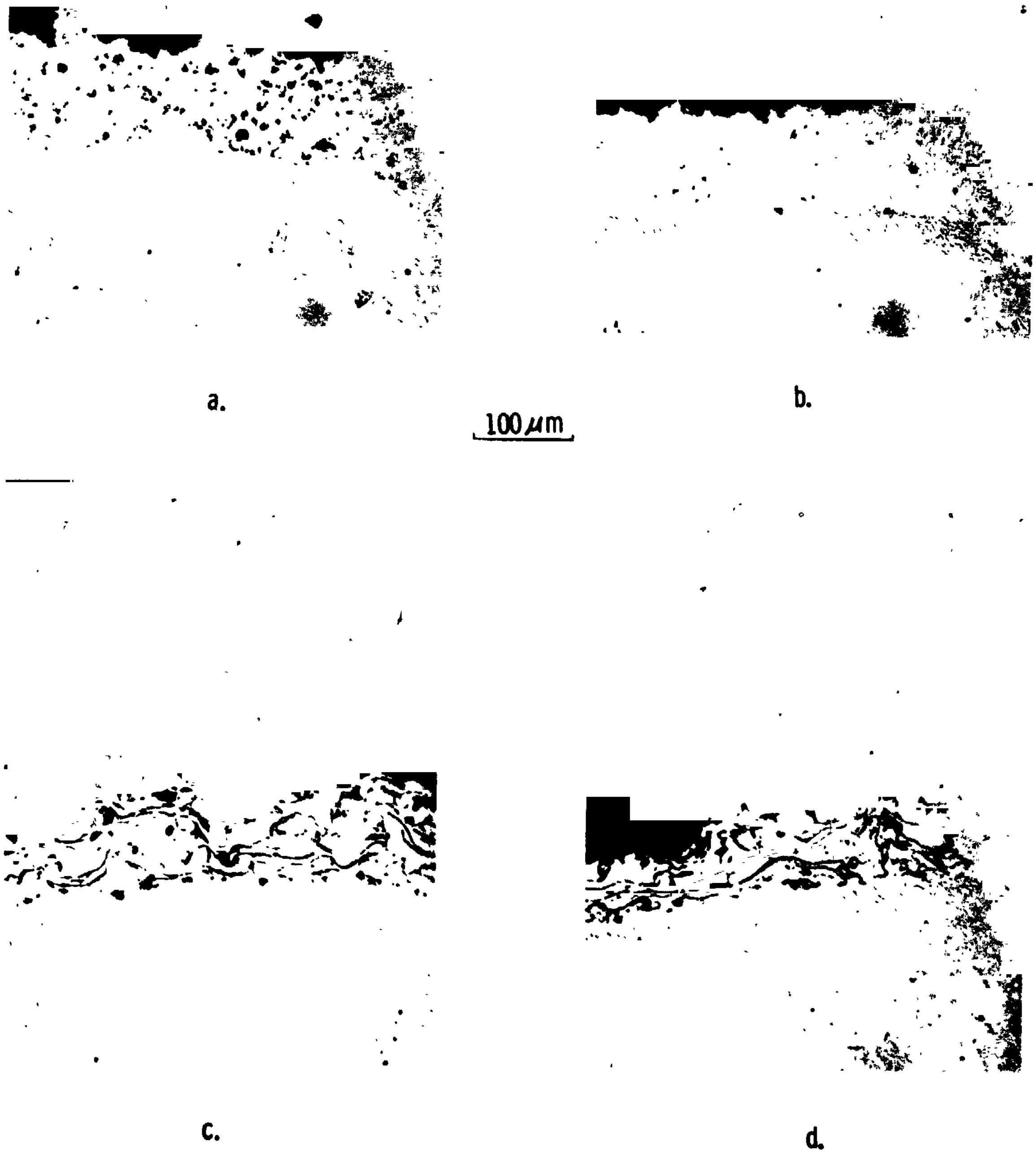

Figure 27 Typical hot corrosion test specimen microstructures. (a) Specimen A6 - as-coated 8 w/o Y_2O_3-ZrO_2 with LP/HV applied NiCrAlY; (b) Specimen A4 - same coating as A6 after completing 292 hours in the hot corrosion rig; (c) Specimen D6 - as-coated 8 w/o Y_2O_3-ZrO_2 with conventionally applied NiCrAlY; (d) Specimen D4 - same coating as D6 after 526 hours in the hot corrosion rig.

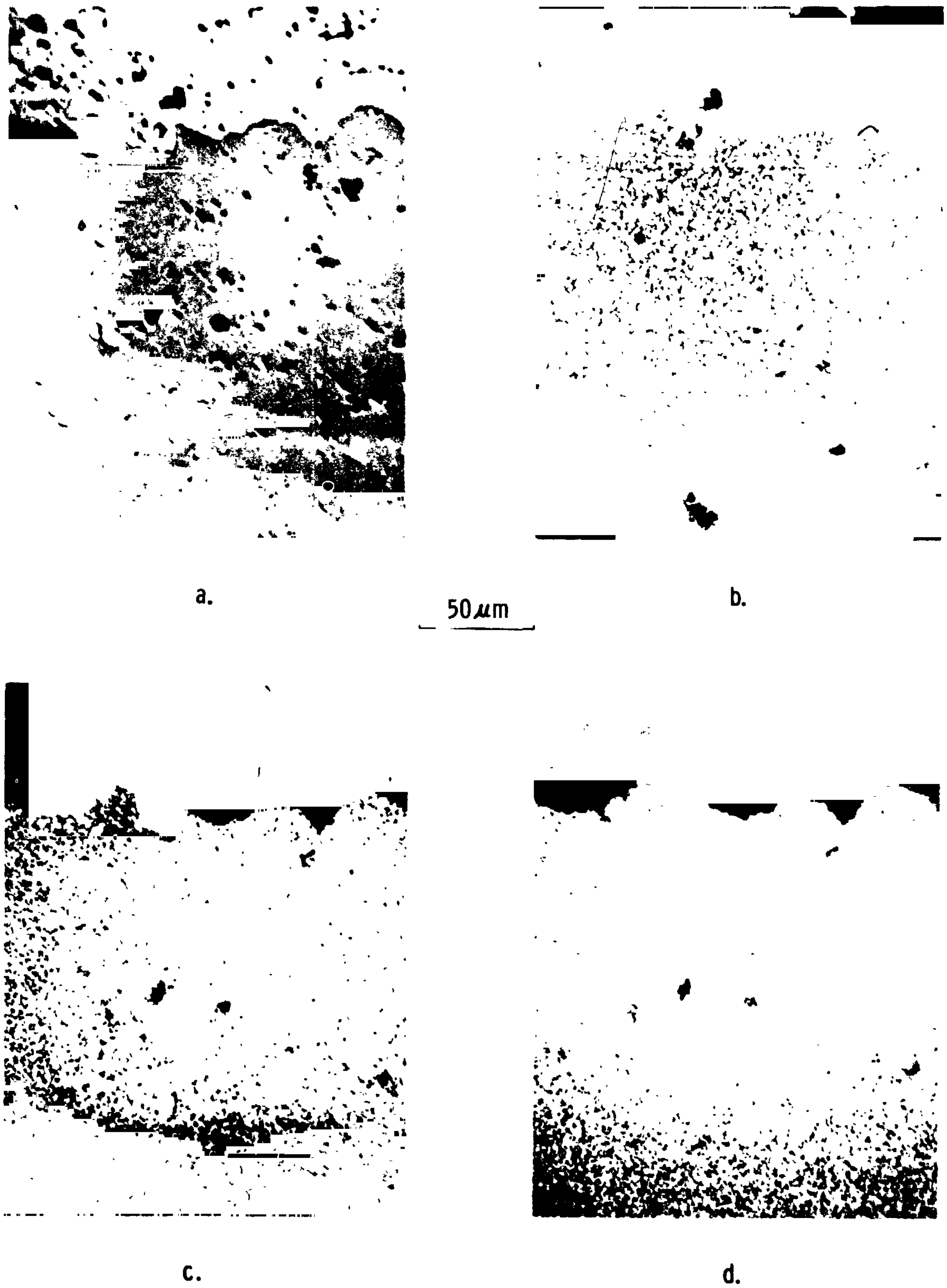

Figure 28 (a) Secondary electron image of specimen A6 - as-coated 8 w/o Y_2O_3-ZrO_2 ceramic and LP/HV applied Ni-22C-10Al-1Y NiCrAlY. Elemental x-ray density maps of (b) aluminum, (c) chromium, and (d) nickel.

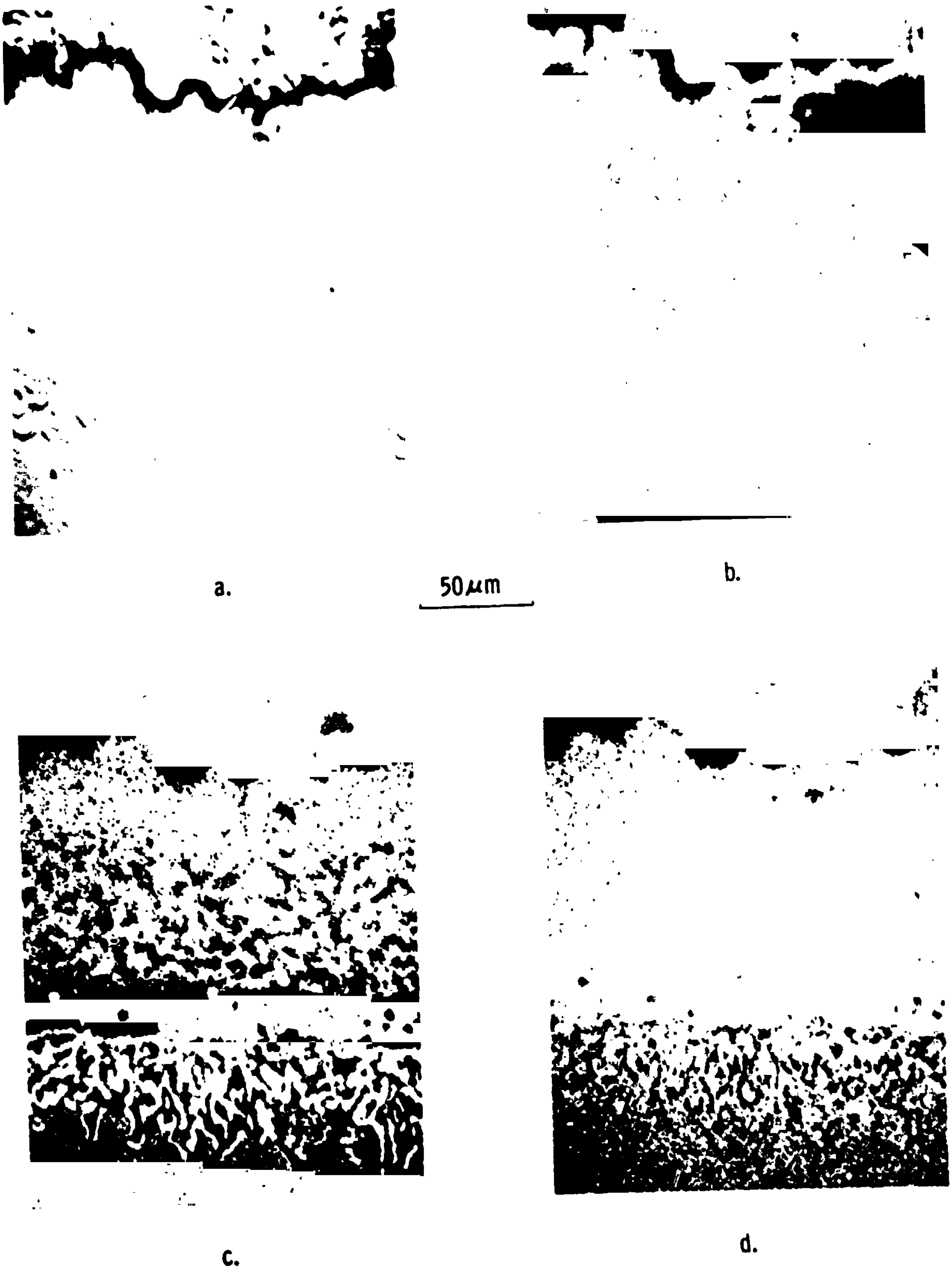

Figure 29 (a) Secondary electron image of specimen Al - 8 w/o Y_2O_3-ZrO_2 ceramic with LP/HV applied Ni-22Cr-10Al-1Y NiCrAlY after 596 hours in hot corrosion testing. Elemental x-ray density maps of (b) aluminum, (c) chromium, (d) nickel.

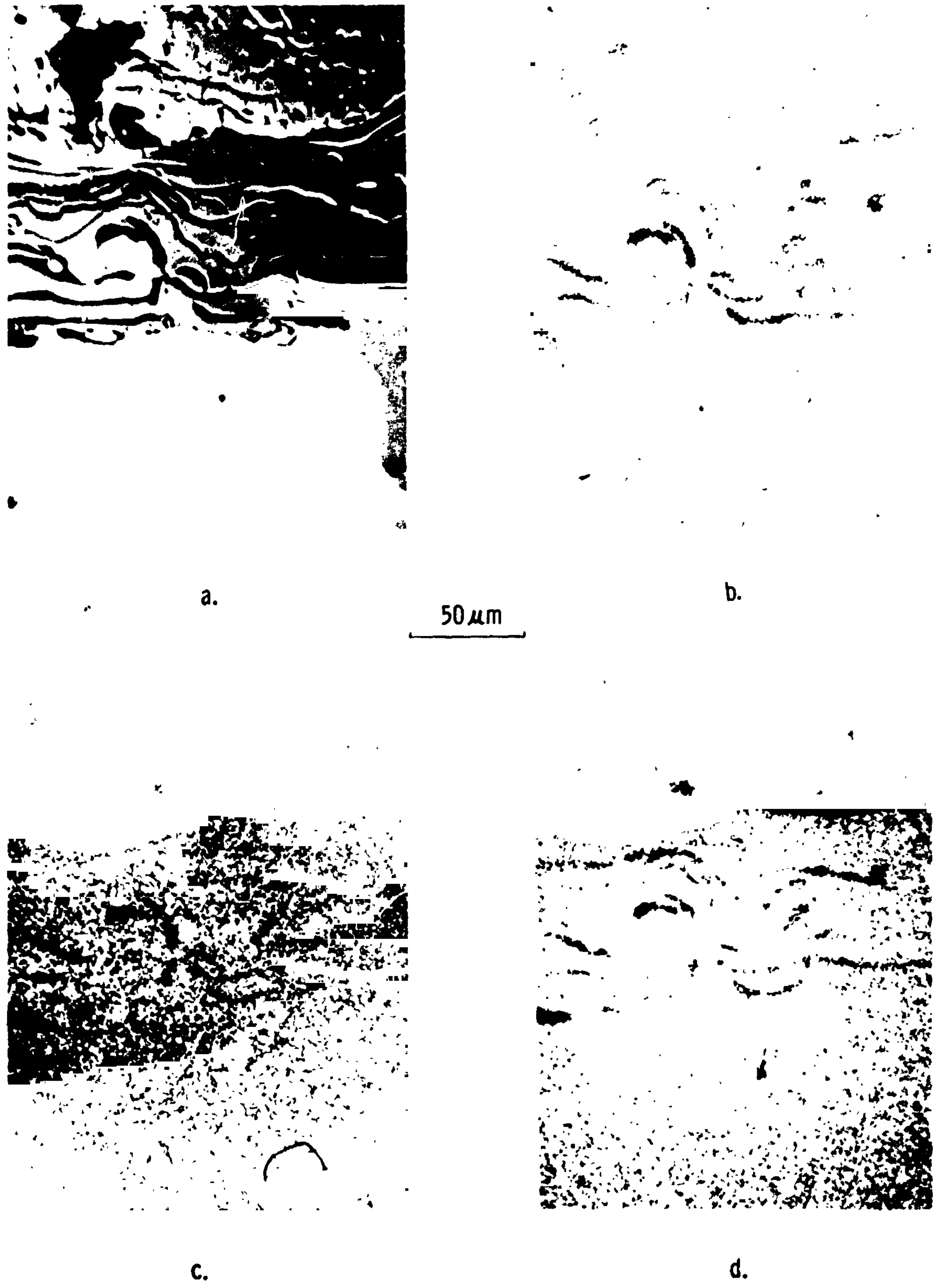

Figure 30 (a) Secondary electron image of specimen D6 - as-coated 8 w/o Y_2O_3-ZrO_2 ceramic with air sprayed Ni-18Cr-12Al-0.3Y NiCrAlY. Elemental x-ray density maps of (b) aluminum, (c) chromium, (d) nickel.

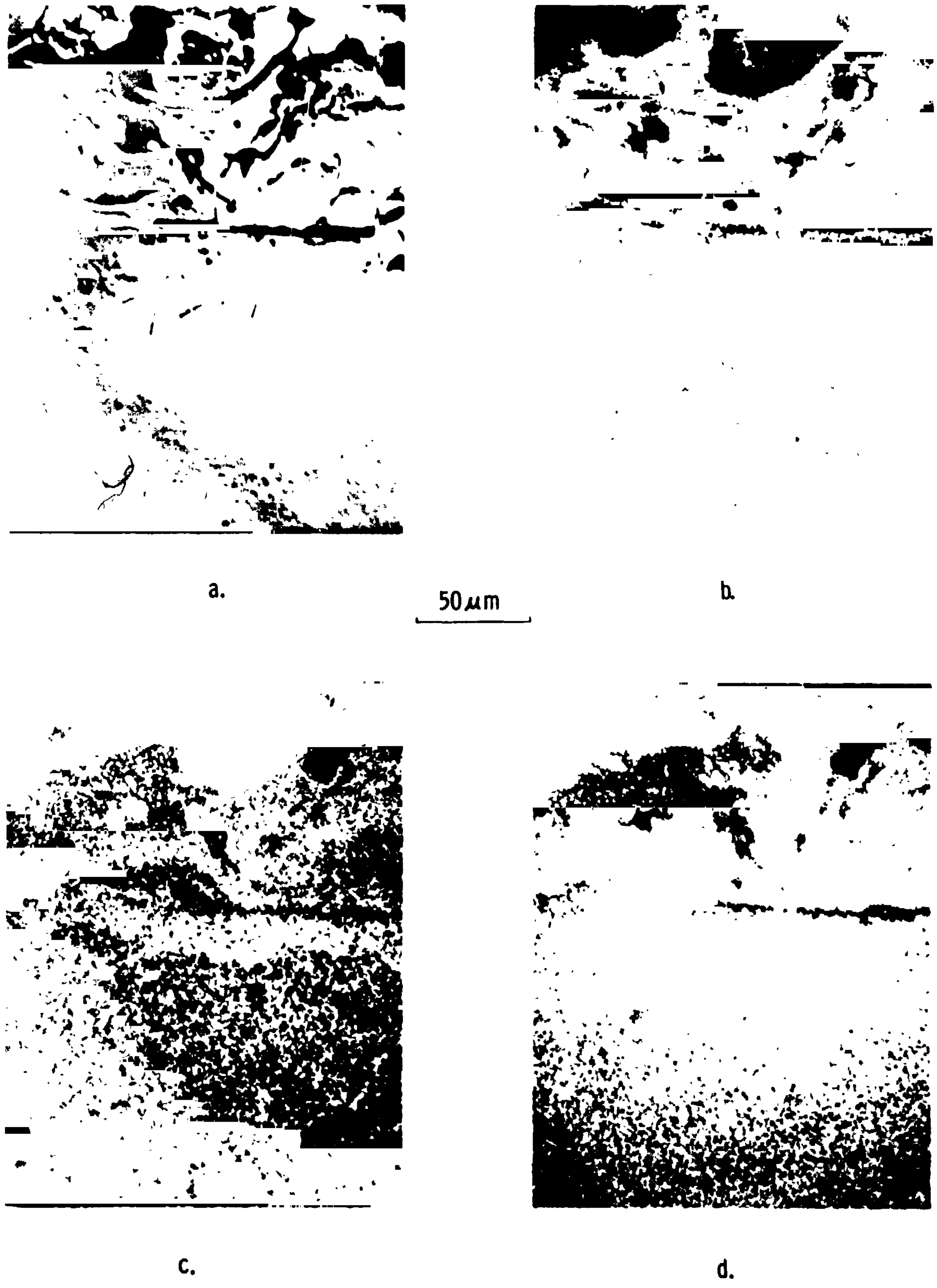

Figure 31 (a) Secondary electron image of specimen D4 8 w/o Y_2O_3-ZrO_2 ceramic with air sprayed Ni-[illegible]Cr-12Al-0.3Y NiCrAlY after 526 hours in hot corrosion testing. Elemental x-ray density maps of (b) aluminum, (c) chromium, (d) nickel.

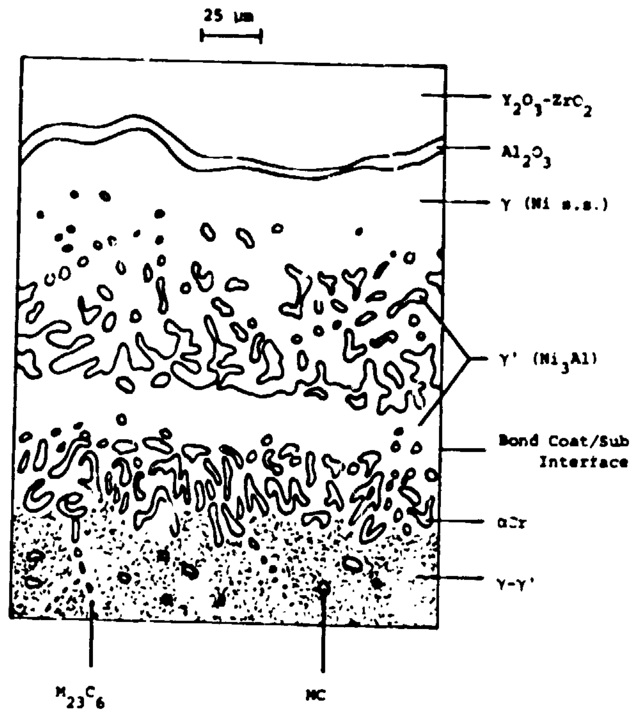

Figure 32 Schematic diagram of a typical hot corrosion test specimen with LP/HV bond coat after time at temperature identifying the phases present in the microstructure.

(a)

(b)

Figure 33 (a) Specimen B5 - 12 w/o Y_2O_3-ZrO_2 ceramic with LP/HV applied Ni-22Cr-10Al-1Y NiCrAlY after 168 hours in hot corrosion testing. (b) Specimen B6 - as-coated 12 w/o Y_2O_3-ZrO_2 ceramic with LP/HV applied Ni-22Cr-10Al-1Y NiCrAlY.

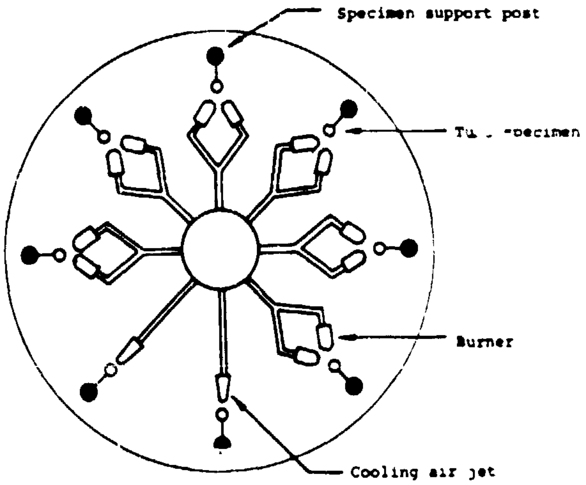

Figure 34 Schematic diagram of M&PTL's SETS II test rig.

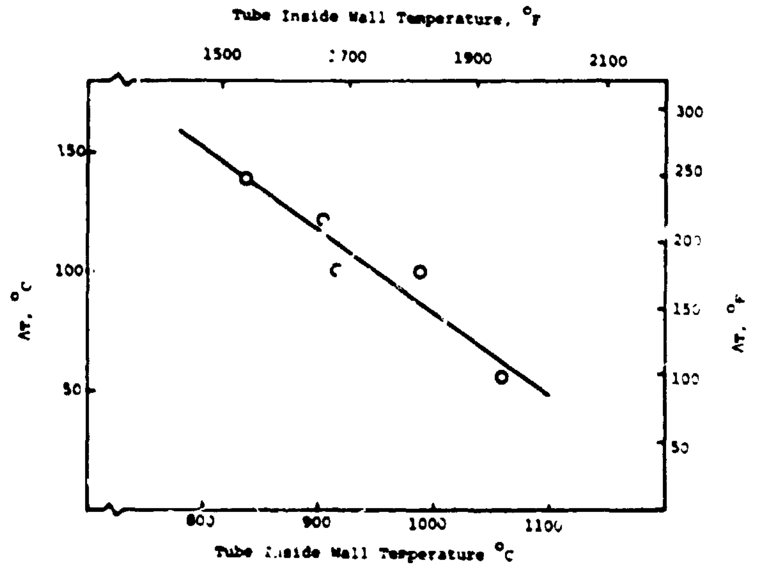

Figure 35 Plot of the ΔT obtained while varying tube inside wall temperature for a sample specimen in the SETS II test rig.

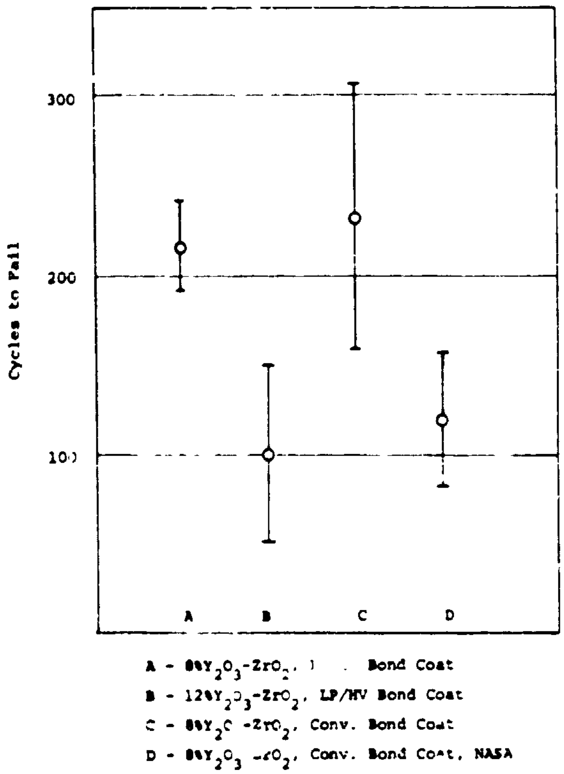

Figure 36 Summary of the cyclic oxidation test results comparing the four coating systems. Error bars are ± 1σ.

Figure 37 Cyclic oxidation test specimens with coating system B (12 w/o Y_2O_3-ZrO_2, LP/HV) showing the failure mode which was typical of all specimens.

Figure 38 (a) Specimen B2 - 12 w/o Y_2O_3-ZrO_2 ceramic with LP/HV applied Ni-22Cr-10Al-1Y NiCrAlY after 178 one-hour cycles in cyclic oxidation testing. (b) Specimen D3 - 8 w/o Y_2O_3-ZrO_2 ceramic air sprayed Ni-18Cr-12Al-0.3Y NiCrAlY after 268 one-hour cycles in cyclic oxidation testing.

C - 2

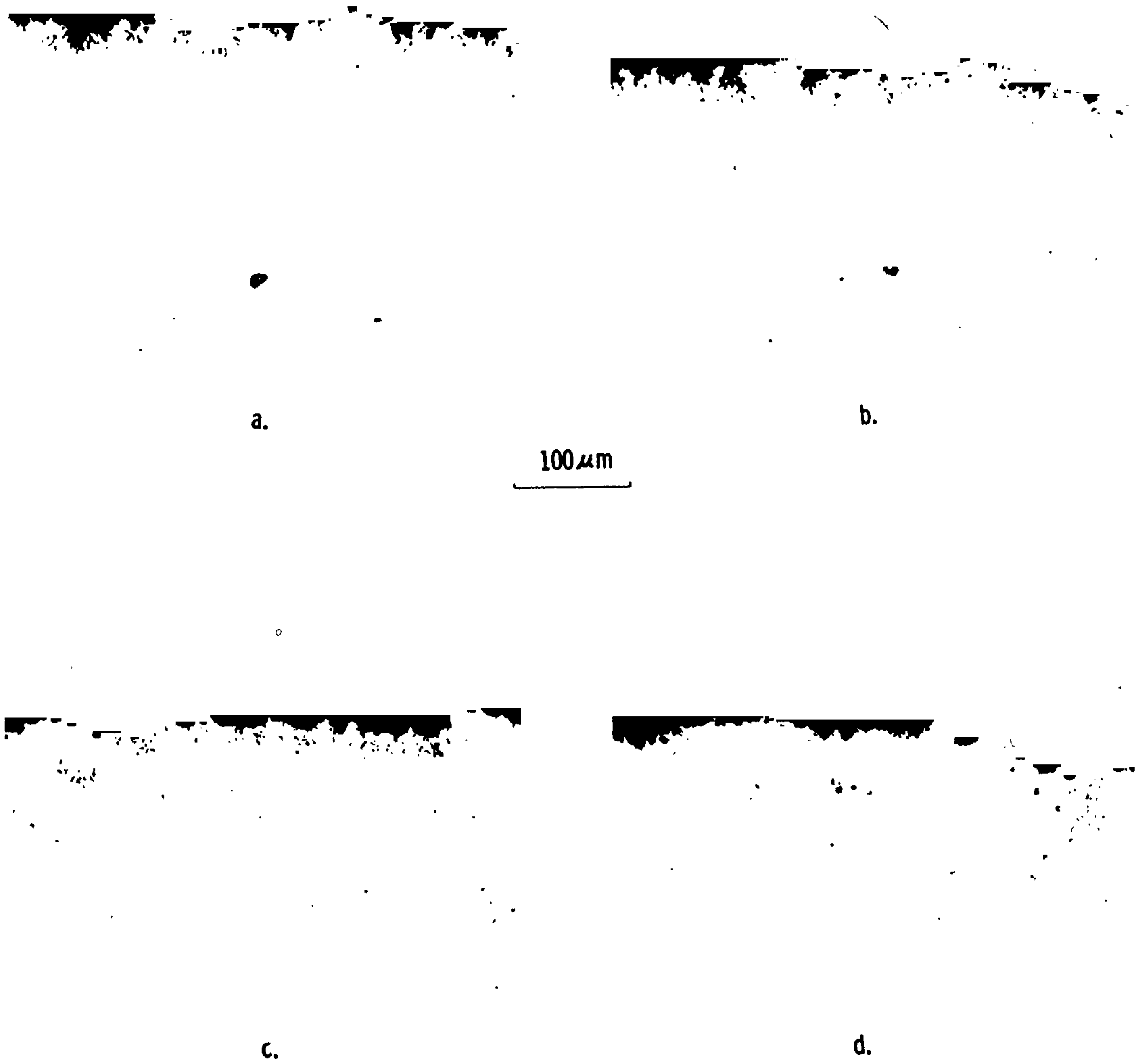

Figure 39 Specimen A1 - 8 w/o Y_2O_3-ZrO_2 ceramic with LP/HV applied Ni-22Cr-10Al-1Y NiCrAlY after 250 one-hour cycles in cyclic oxidation testing. (a) Hot side; (b) 60° toward cool side; (c) 120° toward cool side; (d) cool side.

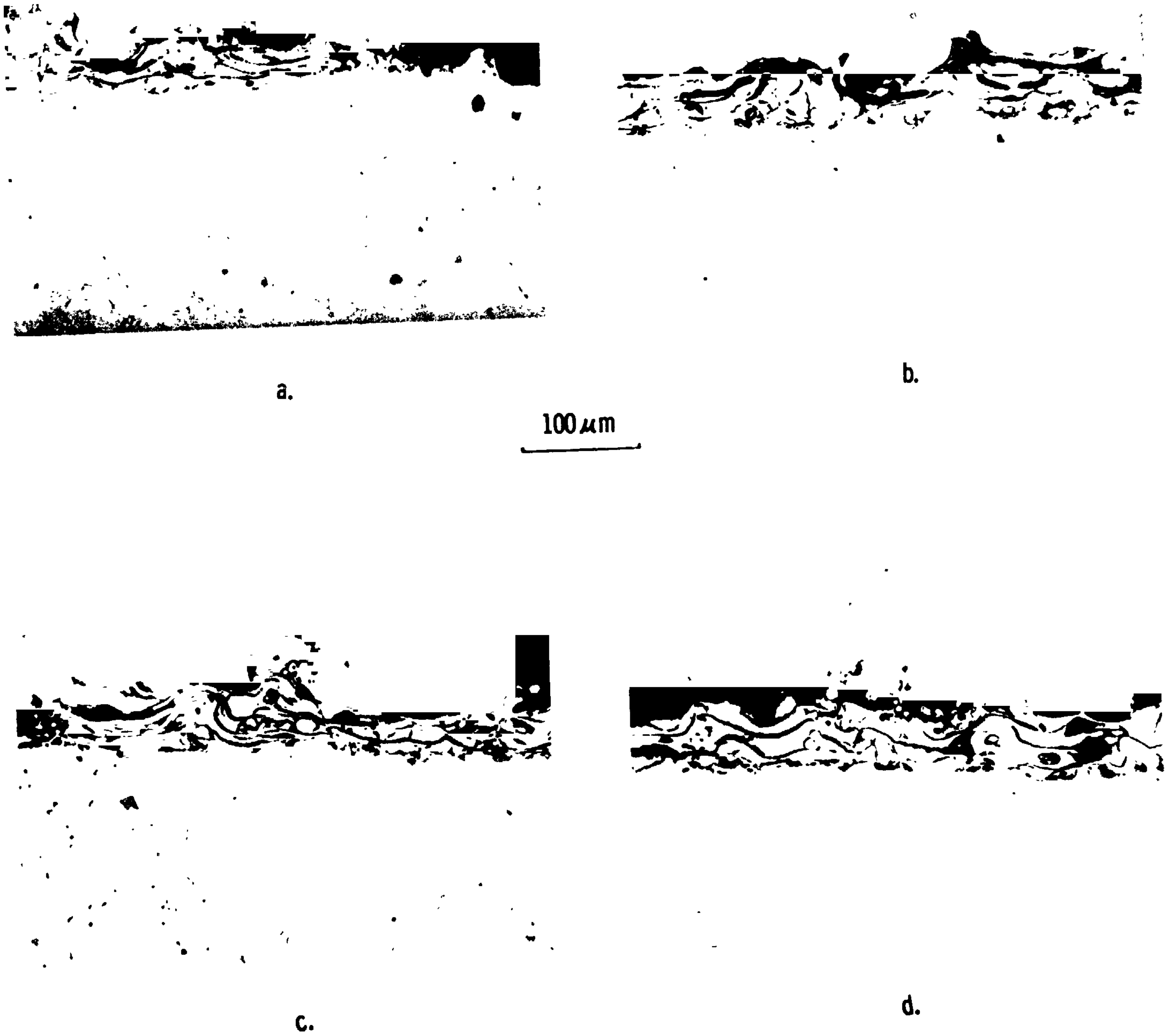

Figure 40 Specimen D3 - 8 w/o Y_2O_3-ZrO_2 ceramic with air sprayed Ni-18Cr-12Al-03Y NiCrAlY after 268 one-hour cycles in cyclic oxidation testing. (a) Hot side; (b) 60° toward cool side; (c) 120° toward cool side; (d) cool side.

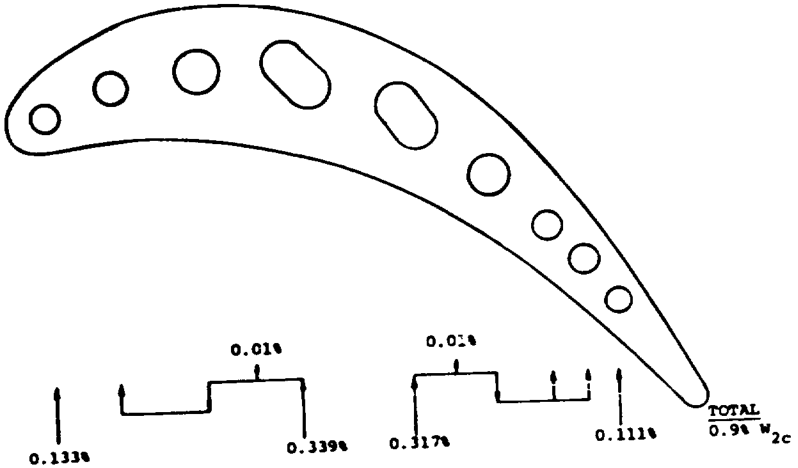

Average compressor exit gas temperature.	T_3 = 591°C (1095°F)
Average turbine inlet gas temperature.	T_4 = 1437°C (2618°F)
Average turbine gas temperature relative to the second stage blade.	T_{TR} = 1076°C (1968°F)
High pressure turbine rotor speed.	N = 10391 rpm
Compressor inlet air flow.	W_{2c} = 124.6 kg/sec (274.4 lb/sec)
Second stage blade coolant flow.	W_{ct} = 0.9% W_{2c}

Figure 41 Coolant flow geometry and standard design conditions of the CF6-50 stage 2 high pressure turbine blade.

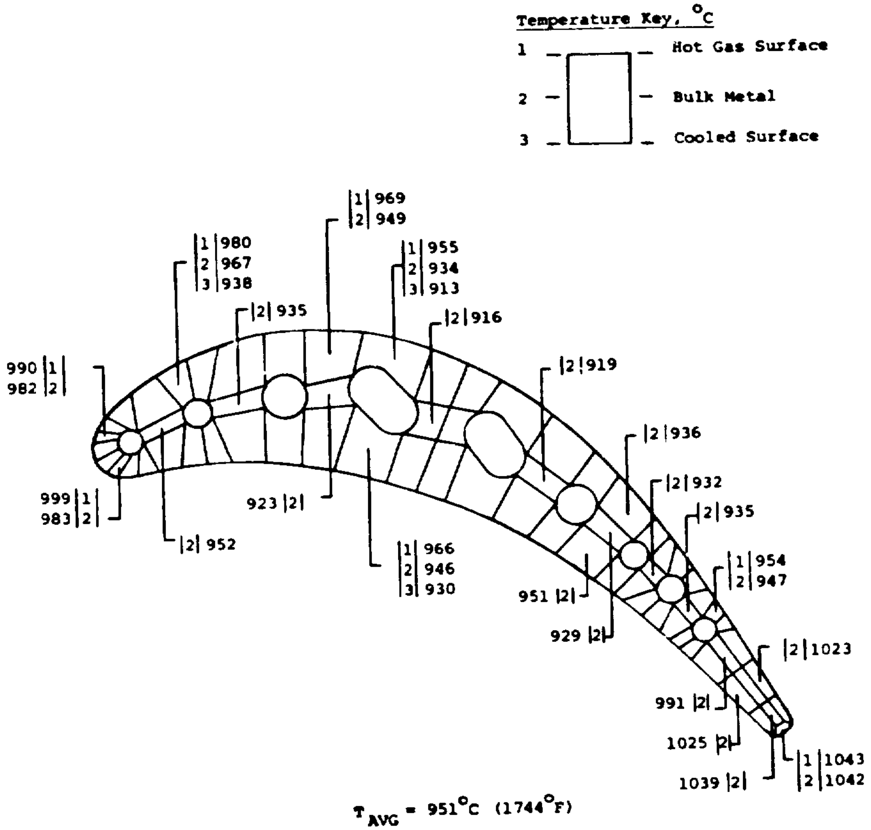

Figure 42 Temperature distribution without a thermal barrier coating of the CF6-50 stage 2 high pressure turbine blade at the 50% span location.

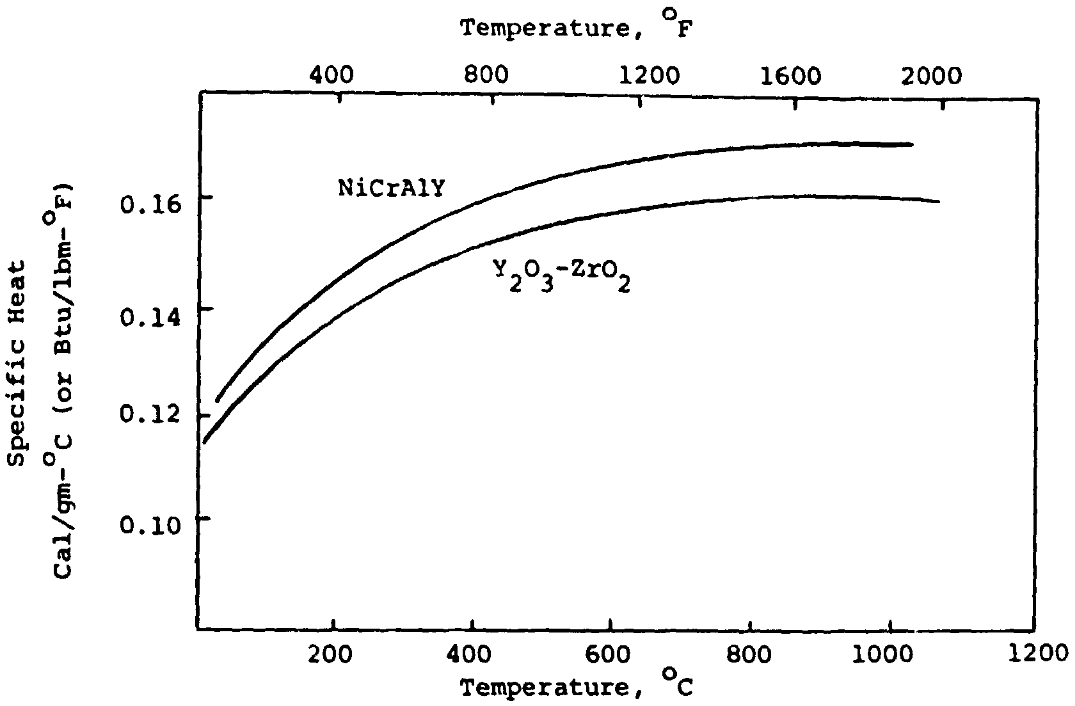

Figure 43 Variation of specific heat with temperature for the NiCrAlY bond coat and Y_2O_3-ZrO_2 top coat. (Ref. NASA Report CR-135359).

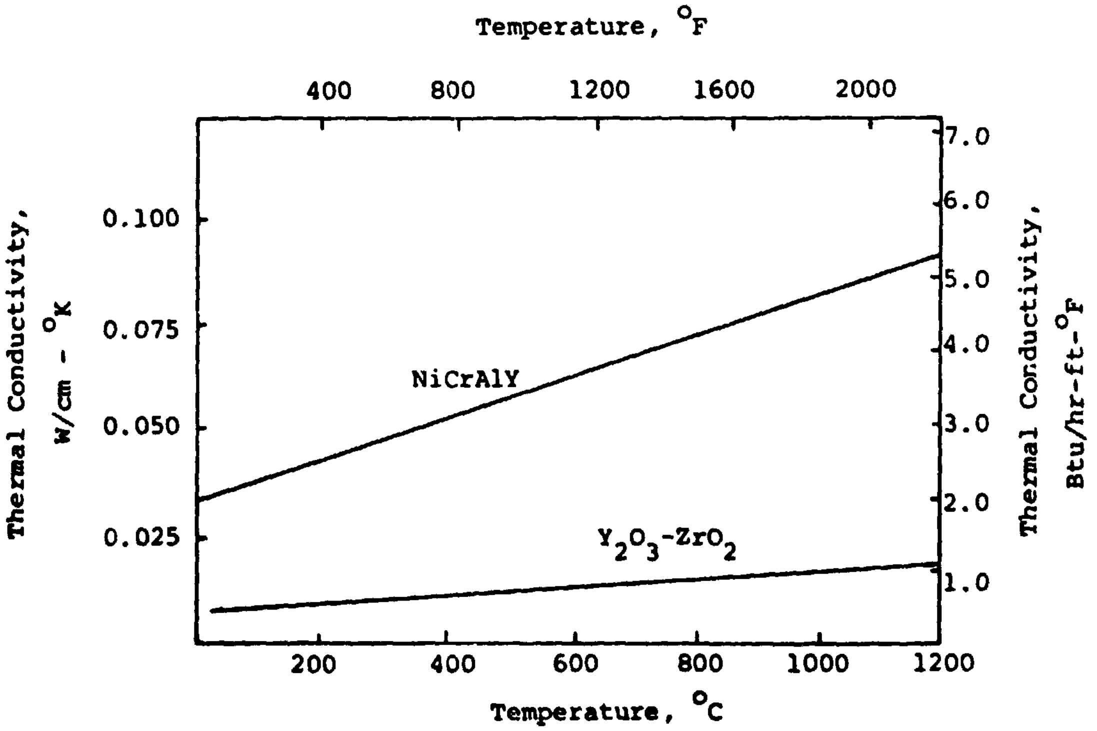

Figure 44 Variation of thermal conductivity with temperature for the NiCrAlY bond coat and Y_2O_3-ZrO_2 top coat. (Ref. NASA Report CR-135359).

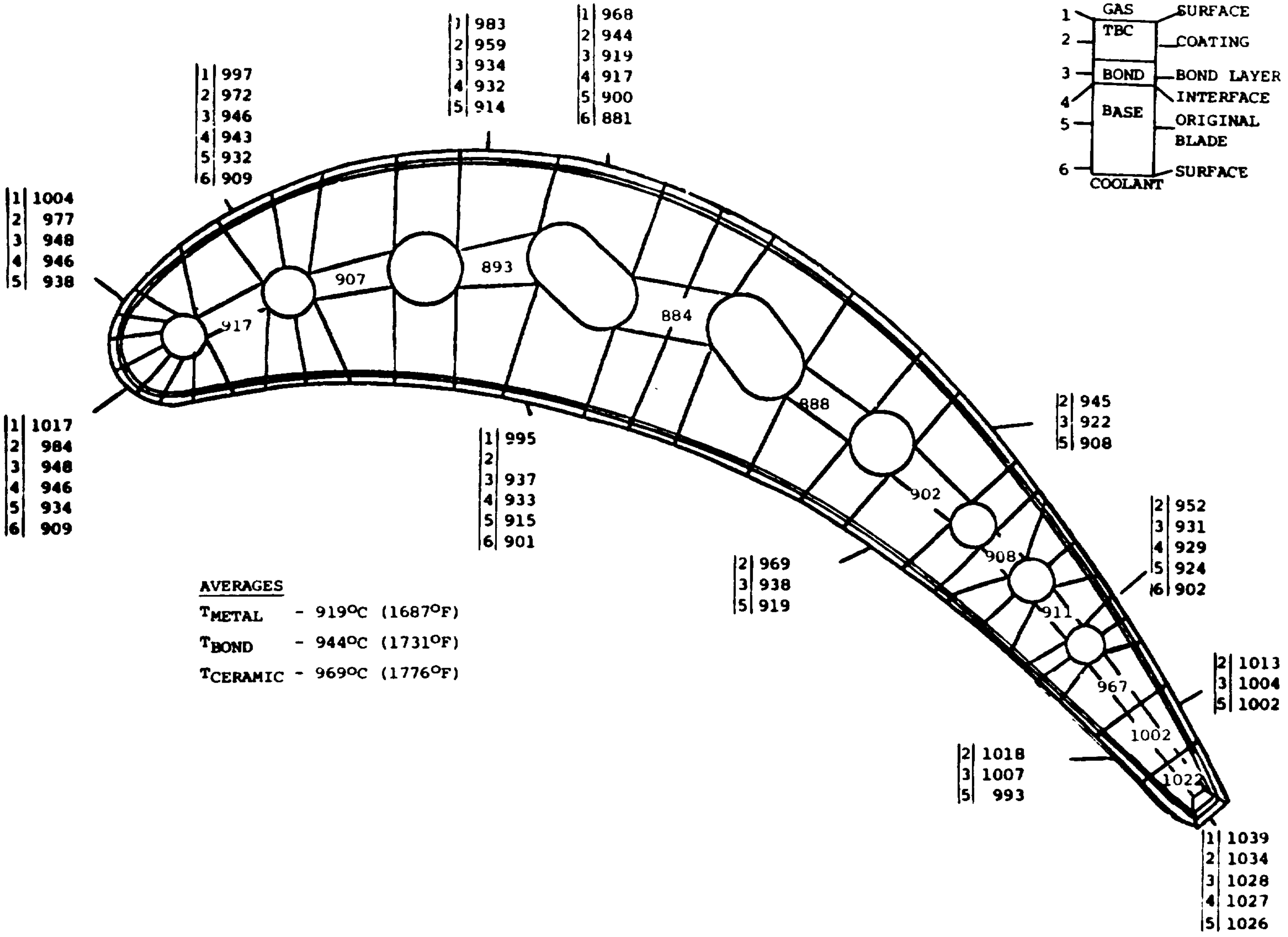

Figure 45 Temperature distribution in a CF6-50 stage 2 HPT blade with a 0.254 mm (0.010 inch) ceramic layer, a 0.127 mm (.005 inch) bond layer, and 100% coolant.

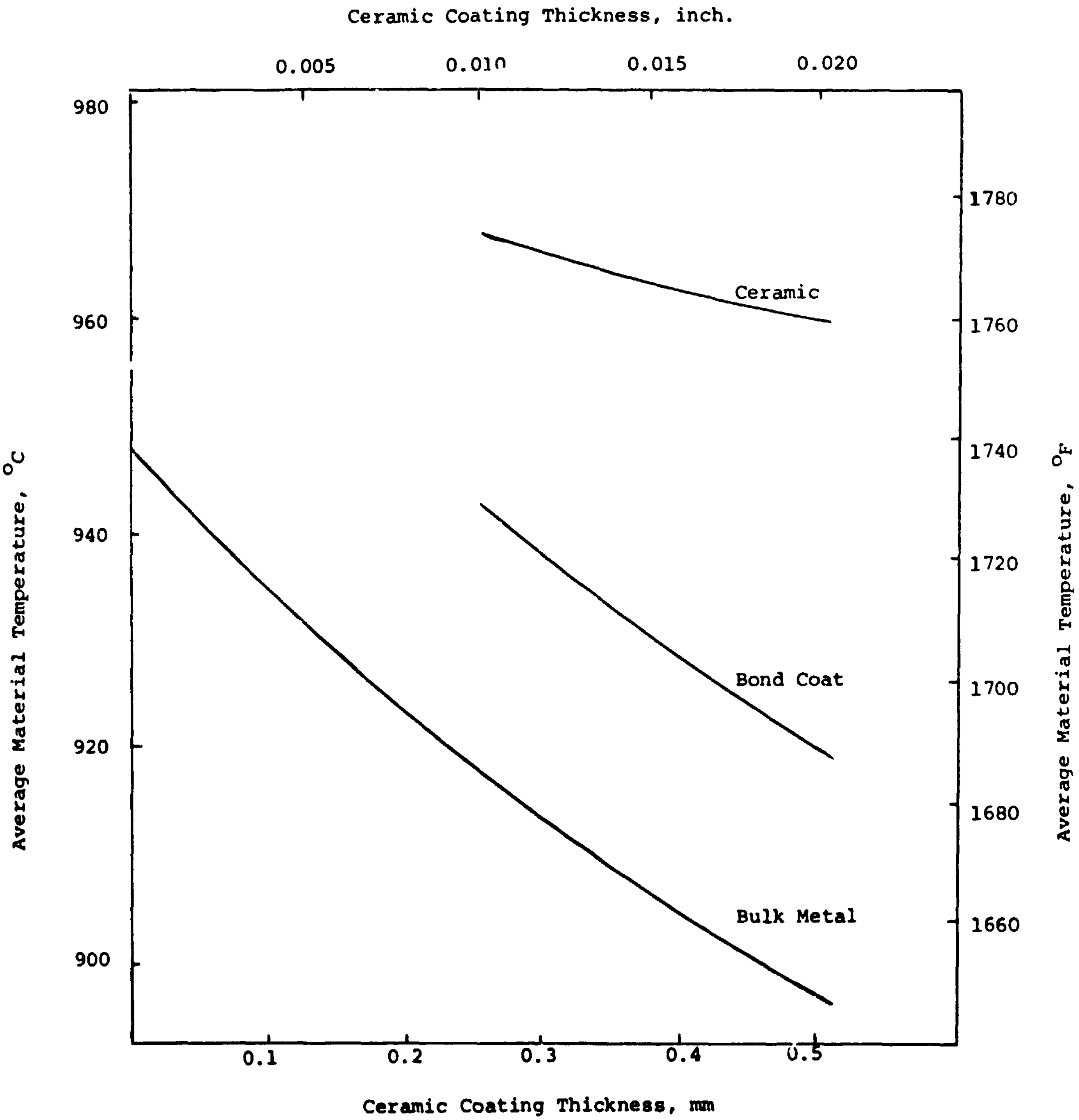

Figure 46 The effect of the ceramic layer thickness on the average material temperatures for a fully coated CF6-50 second stage blade with 100% of standard coolant flow.

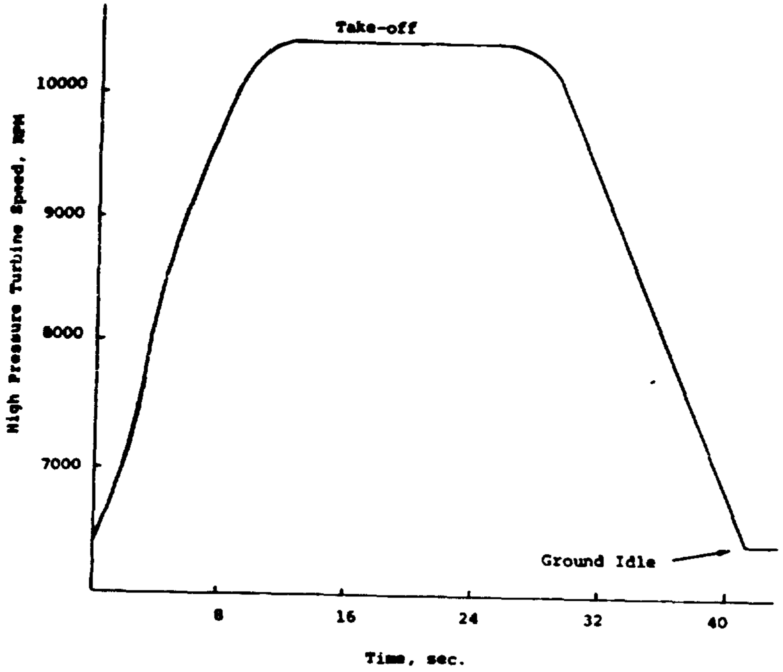

Figure 47 CF6-50 transient HPT speed cycle used in the trade-off study analyses.

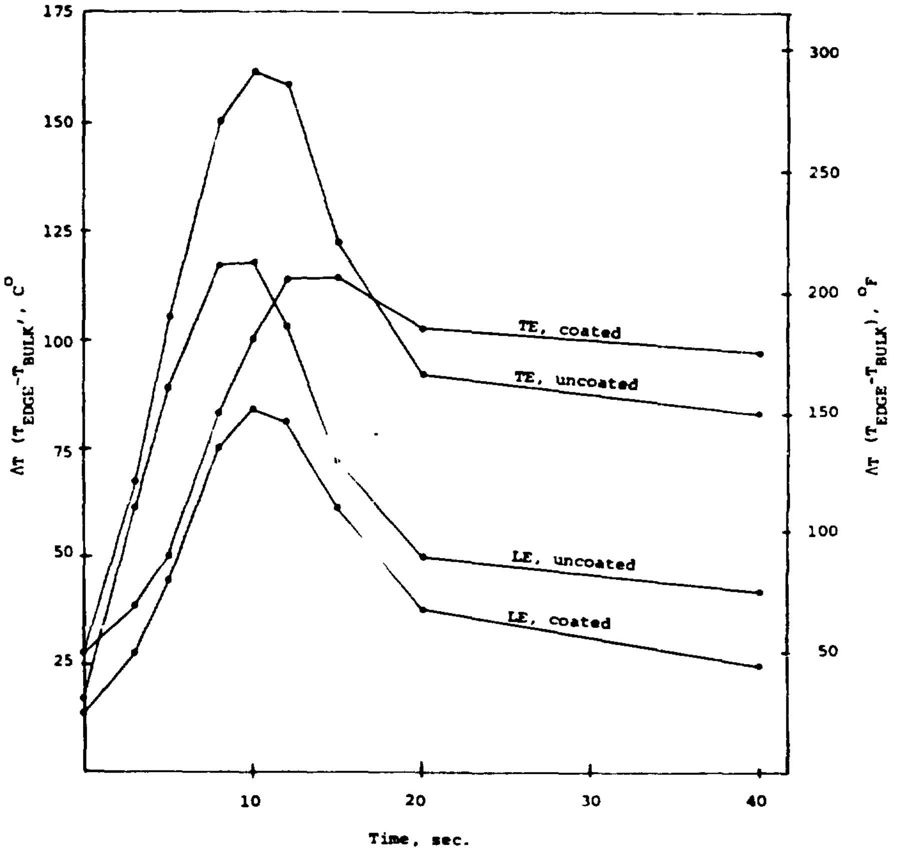

Figure 48 CF6-50 stage 2 HPT blade leading and trailing edge transient ΔT's during the acceleration portion of the transient cycle with and without .25 mm (.010 inch) TBC. Note that because cooling at trailing edge (TE) is less effective than that over entire blade on average the TE of coated blade is relatively hotter at steady state.

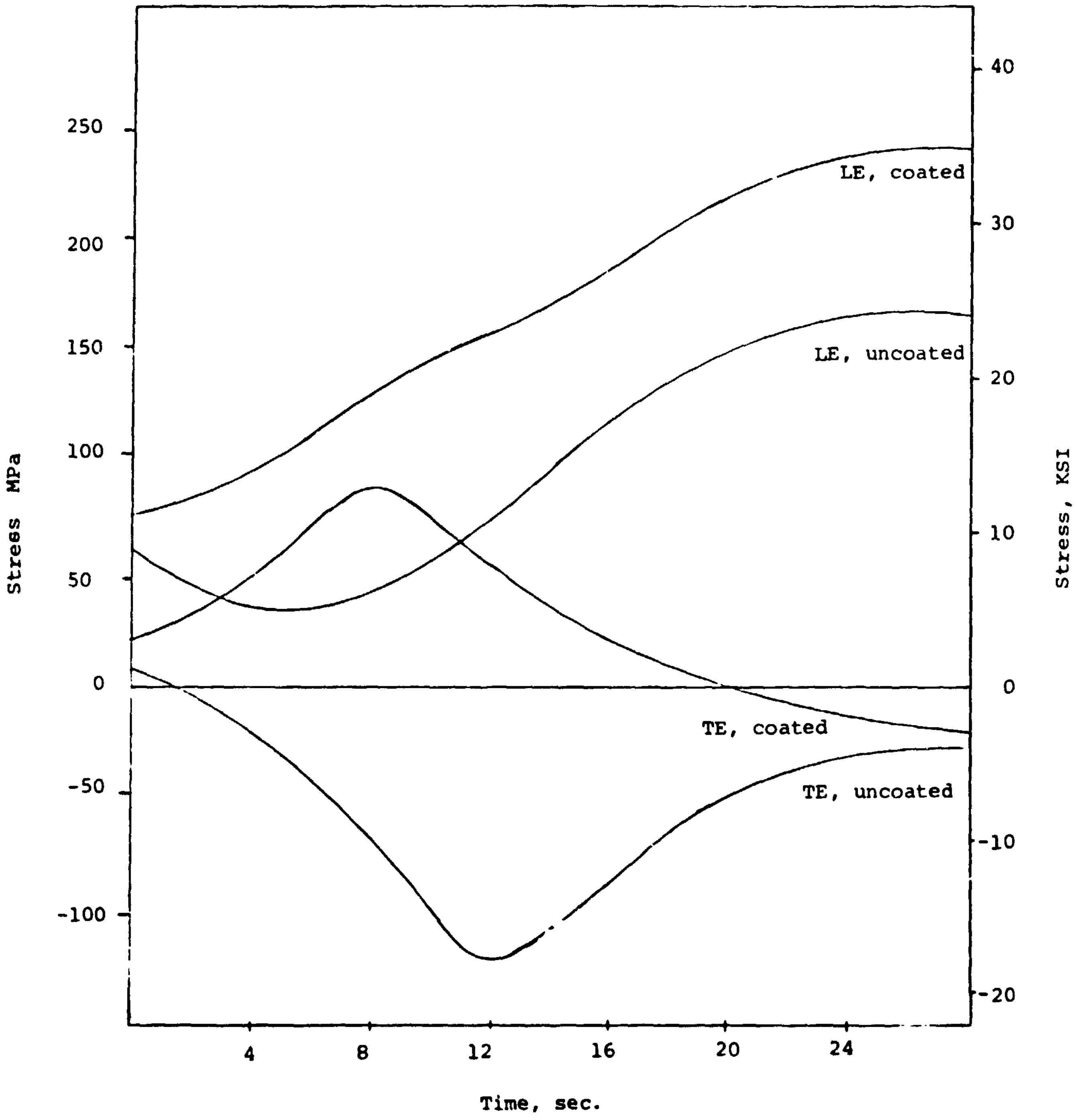

Figure 49 CF6-50 stage 2 HPT blade leading LE and trailing edge TE stress response in the metal substrate during a ground-idle-to-take-off acceleration with and without 0.25 mm (0.010 in.) TBC. Note that TBC produces increase of tensile stress at LE, but decrease of compressive stress at steady stage.

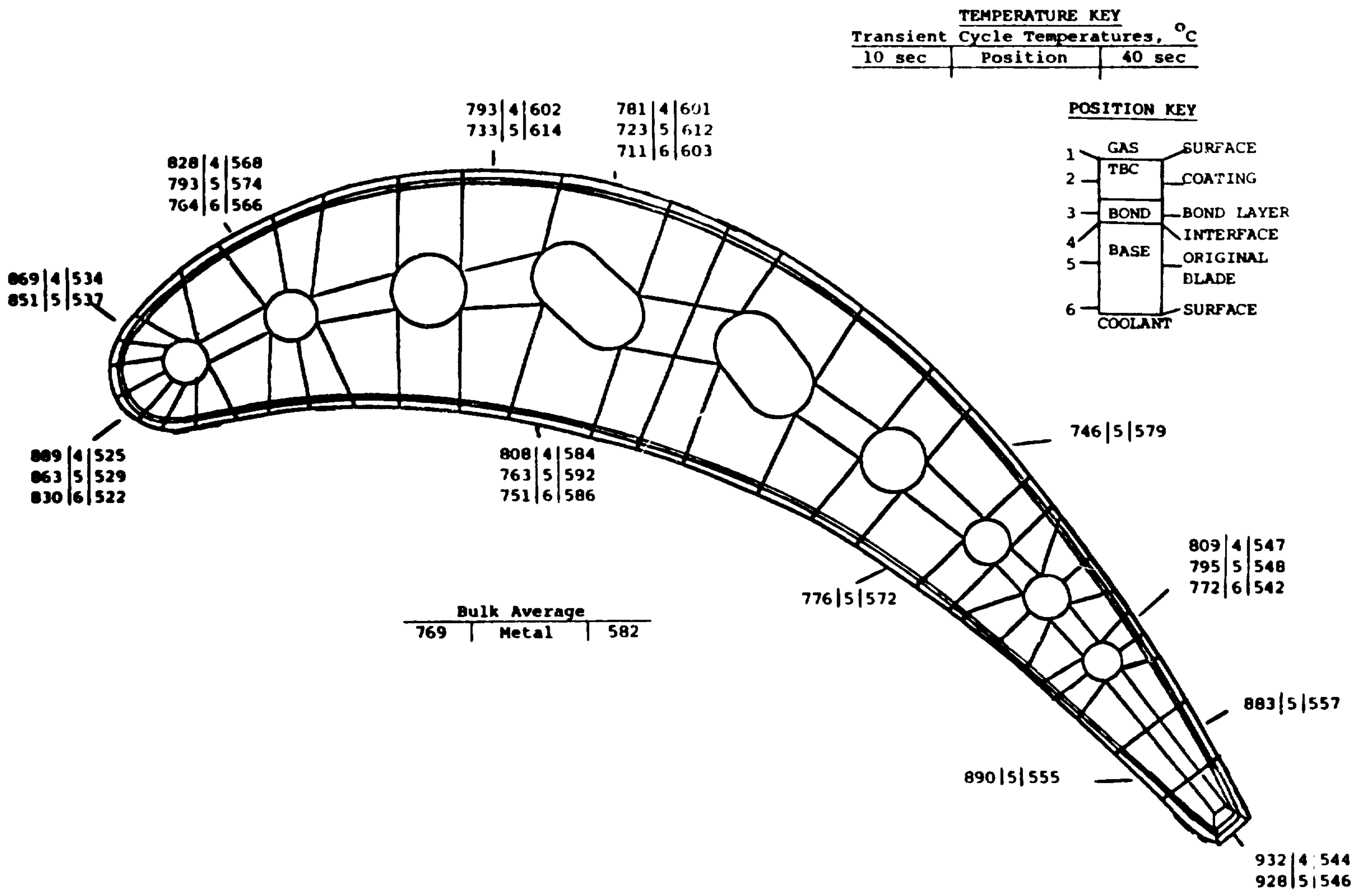

Figure 50 Transient cycle temperature distribution for a CF6-50 stage 2 HPT blade without TBC at take-off time (10s) and ground idle (40s) time points.

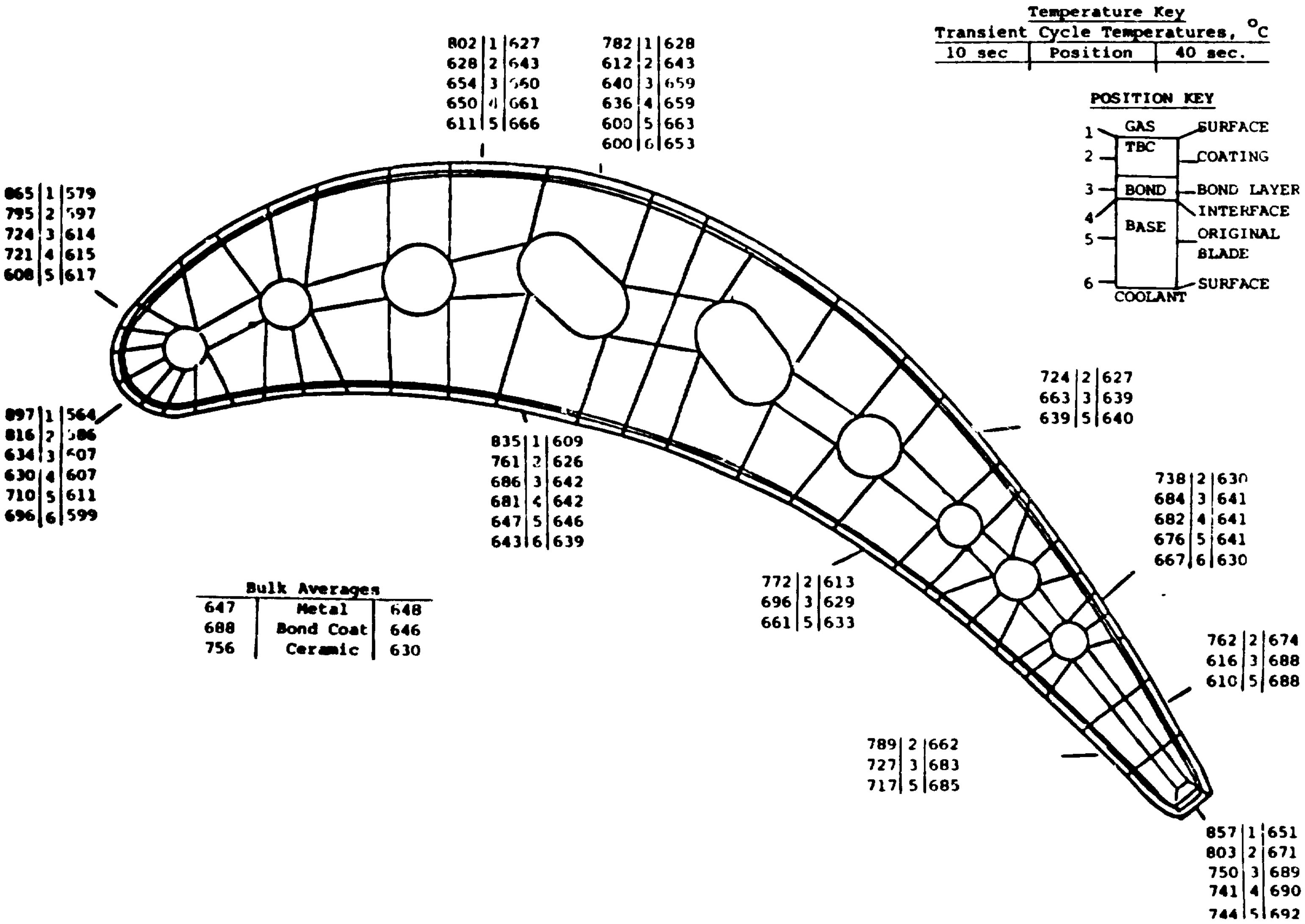

Figure 51 Transient cycle temperature distribution for a CF6-50 stage 2 HPT blade with a thermal barrier coating (0.102 mm bond coat, 0.254 mm ceramic top coat) at take-off (10s) and ground idle (40s).

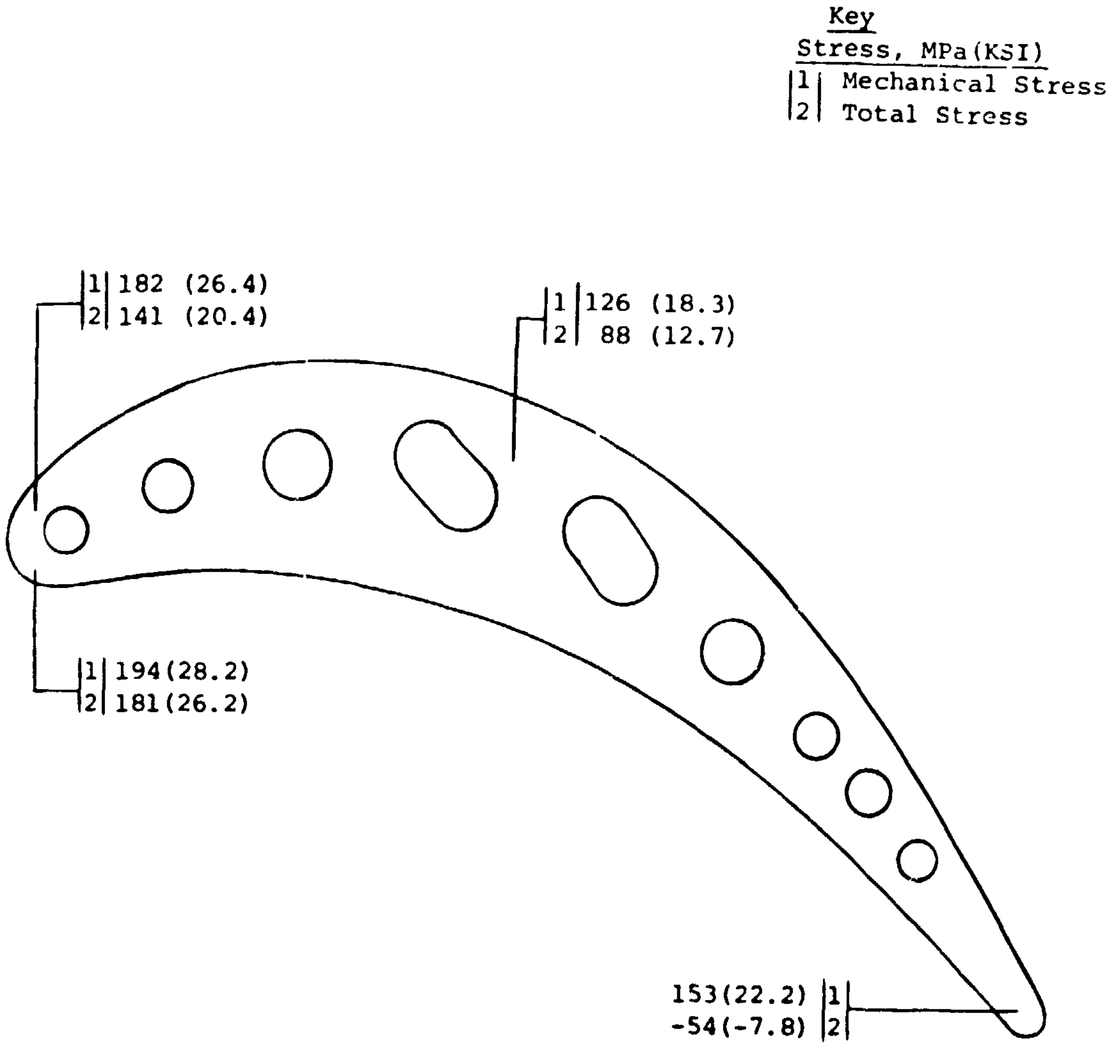

Figure 52 Computed mechanical and total stress within an uncoated CF6-50 stage 2 HPT blade (pitch section) assuming steady state, hot day take-off.

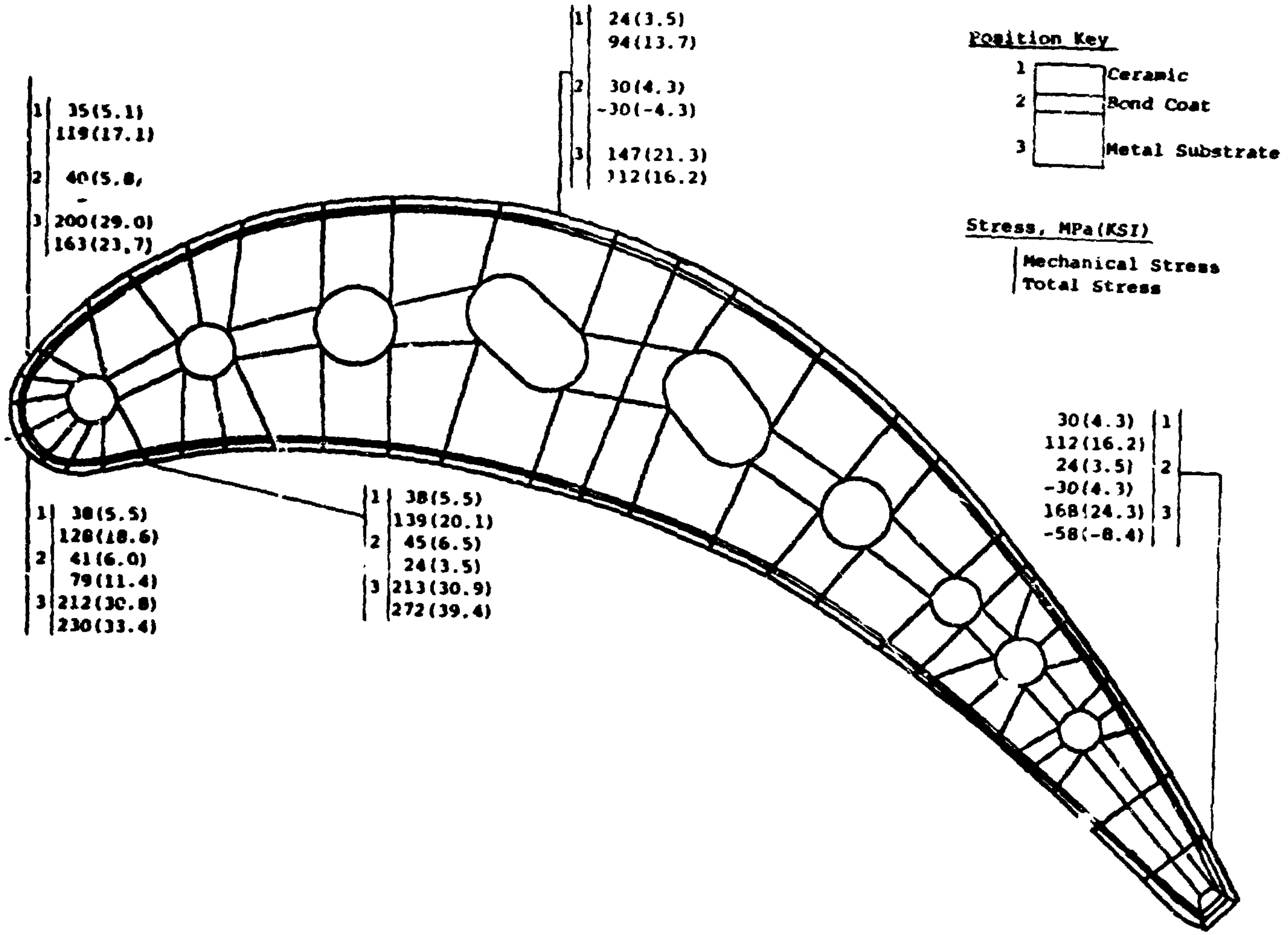

Figure 3 Computed mechanical and total stress within a thermal barrier coated CF6-50 stage 2 HPT blade assuming steady state, hot day take-off.

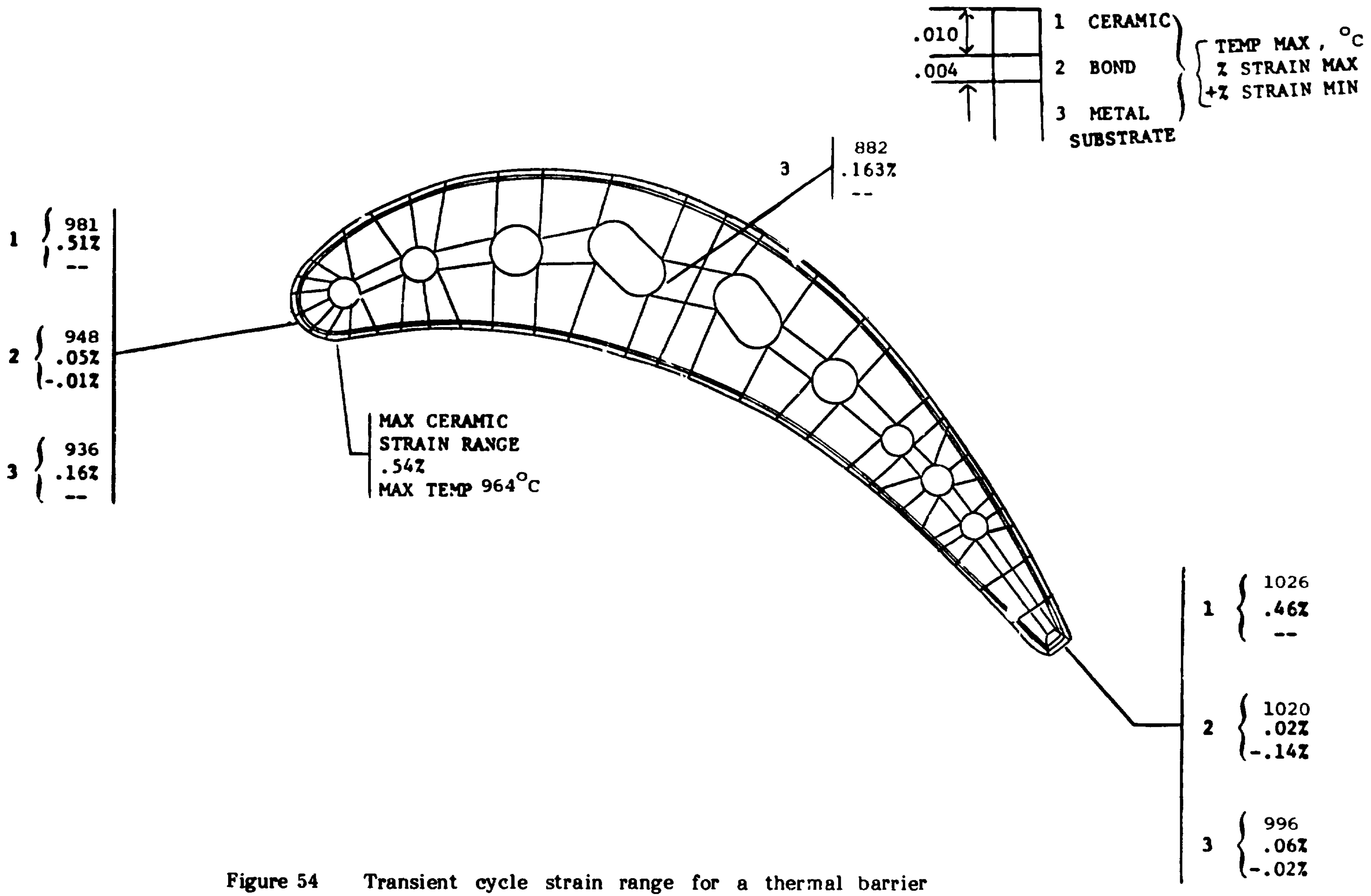

Figure 54 Transient cycle strain range for a thermal barrier coated CF6-50 stage 2 HPT blade.

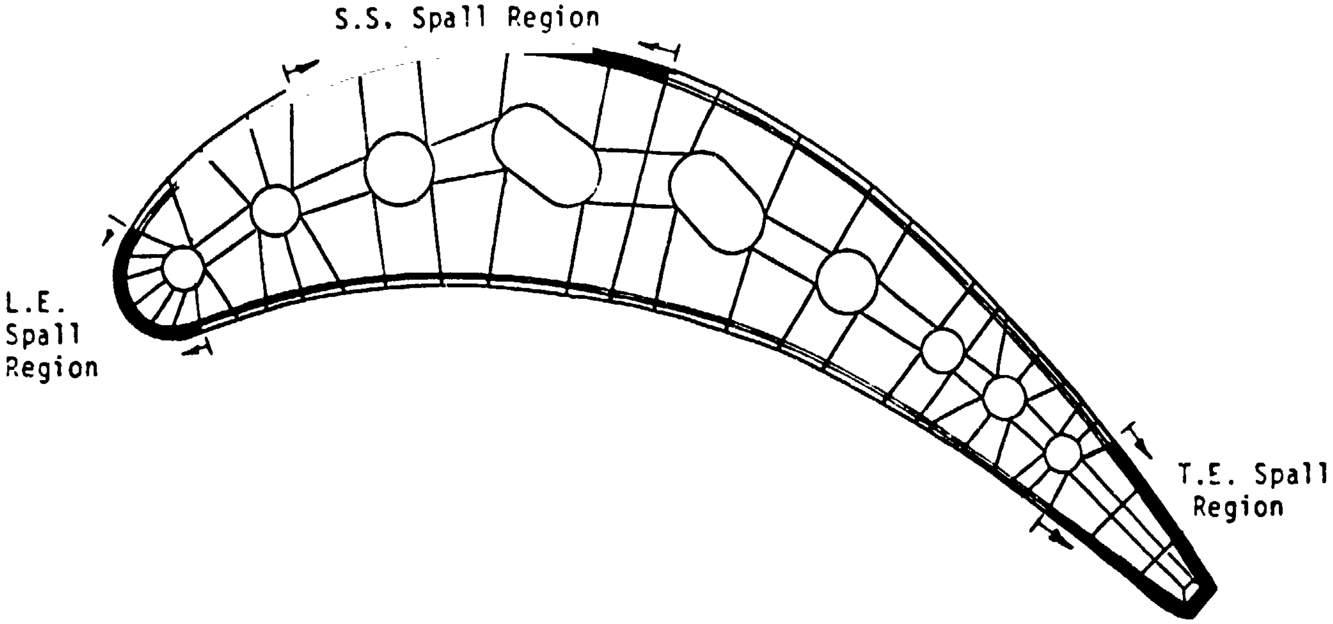

CASES STUDIED

	L.E.	T.E.	L.E.&T.E.	S.S.
Steady State	X	X	X	X
Transient Cycle			X	

Figure 55 Areas of spallation used for the spallation studies of thermal barrier coated CF6-50 stage 2 HPT blades. (L.E. is leading edge, T.E. trailing edge, and S.S. suction side).

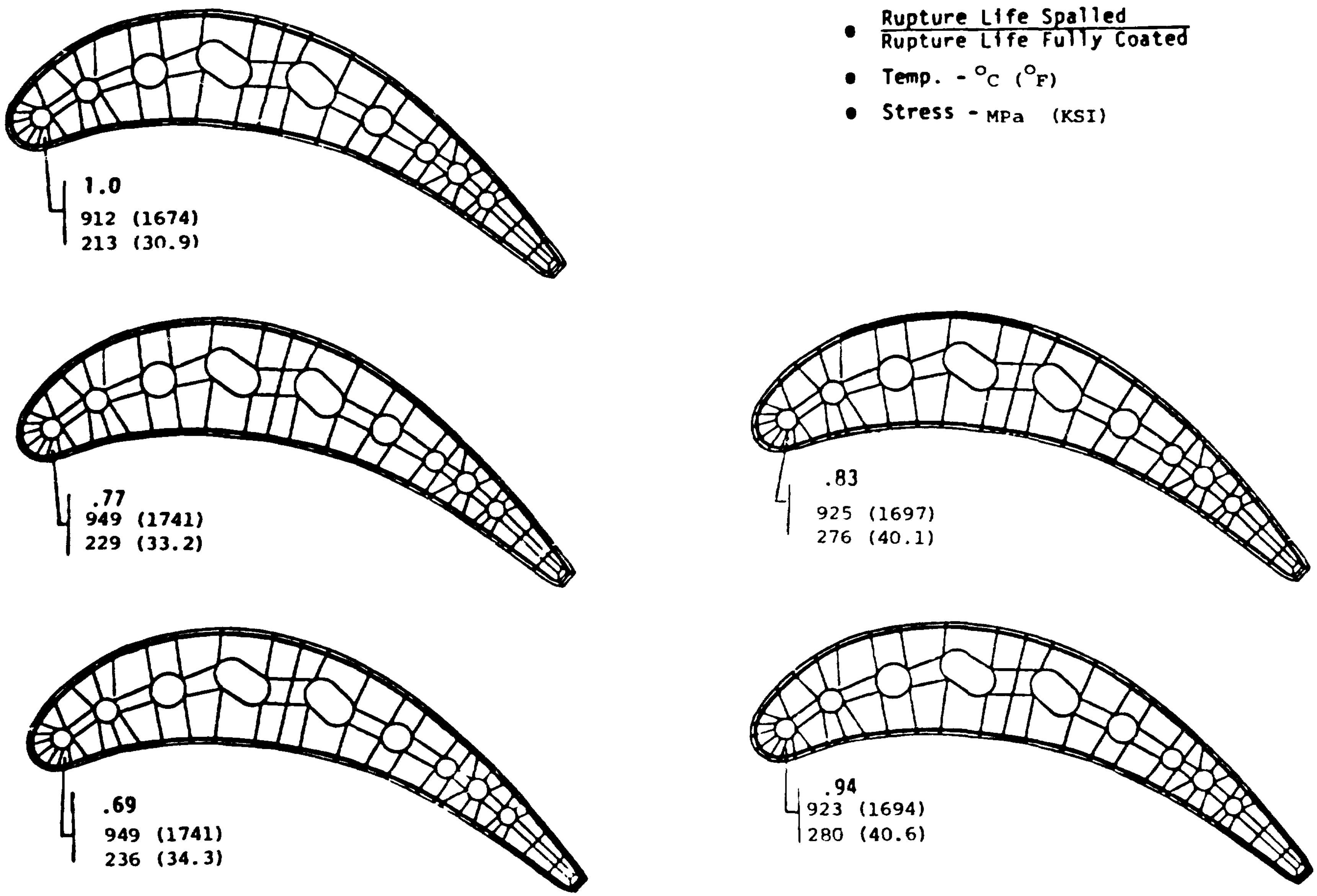

Figure 56 Pitch section rupture life comparison for various local spallation cases of thermal barrier coated CF6-50 stage 2 HPT blade (L.E. is leading edge, T.E. trailing edge, and S.S. suction side).

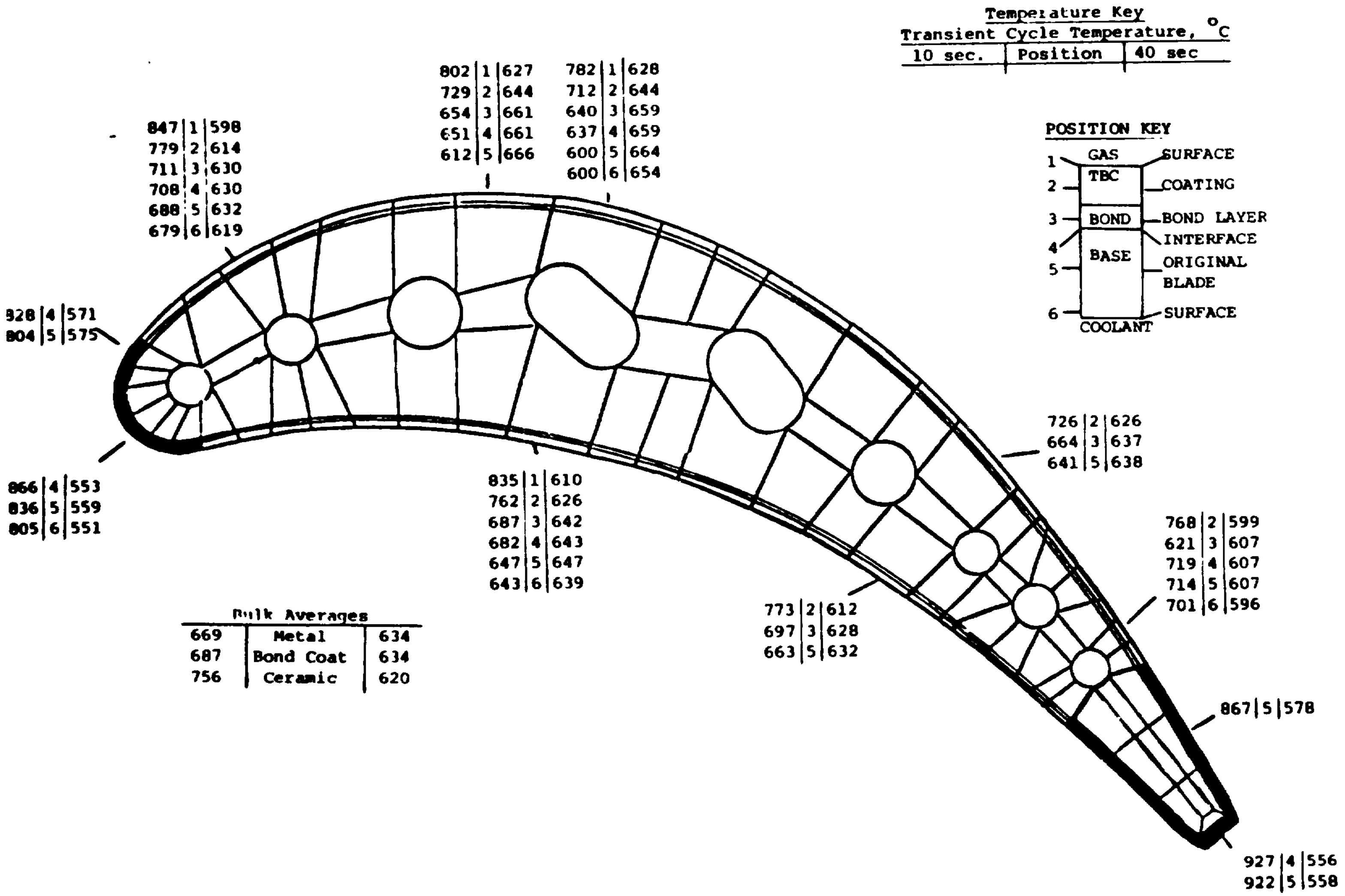

Bulk Averages

669	Metal	634
687	Bond Coat	634
756	Ceramic	620

Figure 57 Temperature distribution during a transient cycle for spallation of the leading and trailing edge regions of a thermal barrier coated (0.102 mm bond coat, 0.254 mm ceramic top coat) CF6-50 stage 2 HPT blade.

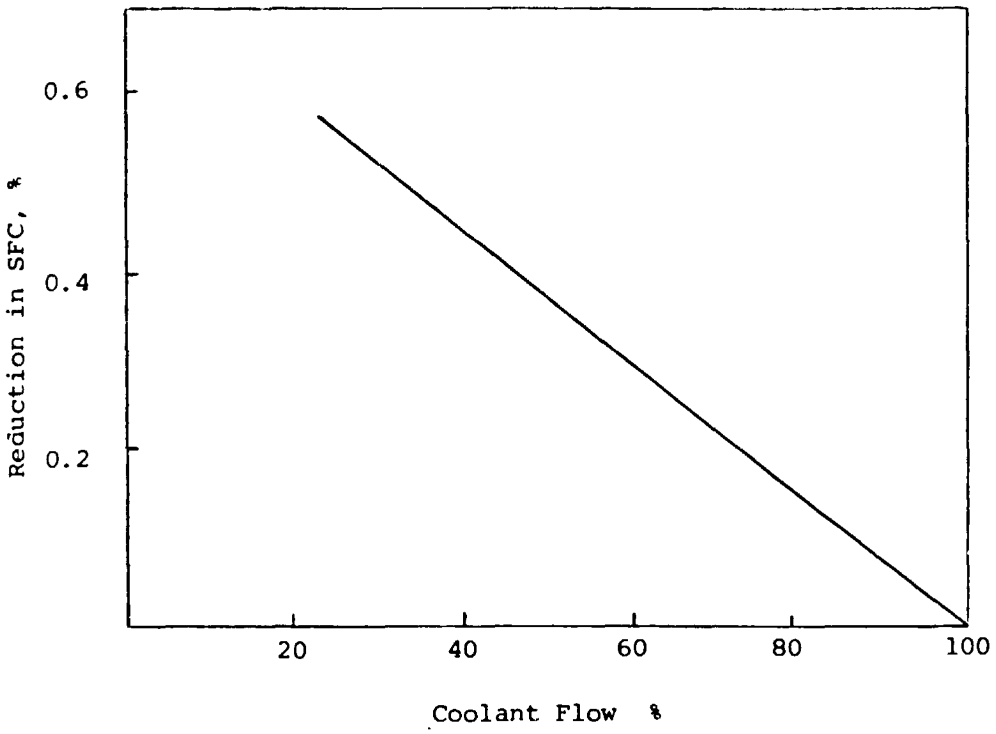

Figure 58 Reduction in specific fuel consumption (SFC) with lowered percent coolant flow for the CF6-50 stage 2 HPT blade coated with 0.25 mm (0.010 inch) oxide.

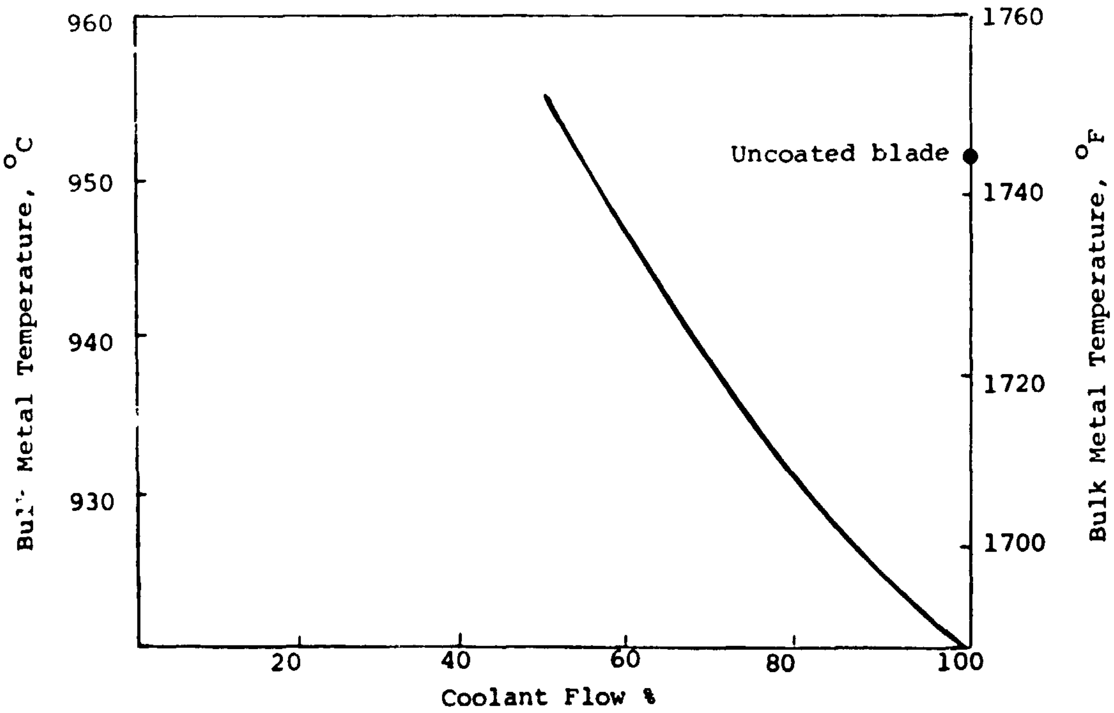

Figure 59 Variation in bulk metal temperature with percent coolant flow for a CF6-50 stage 2 HPT coated with 0.25 mm (0.010 inch) oxide.

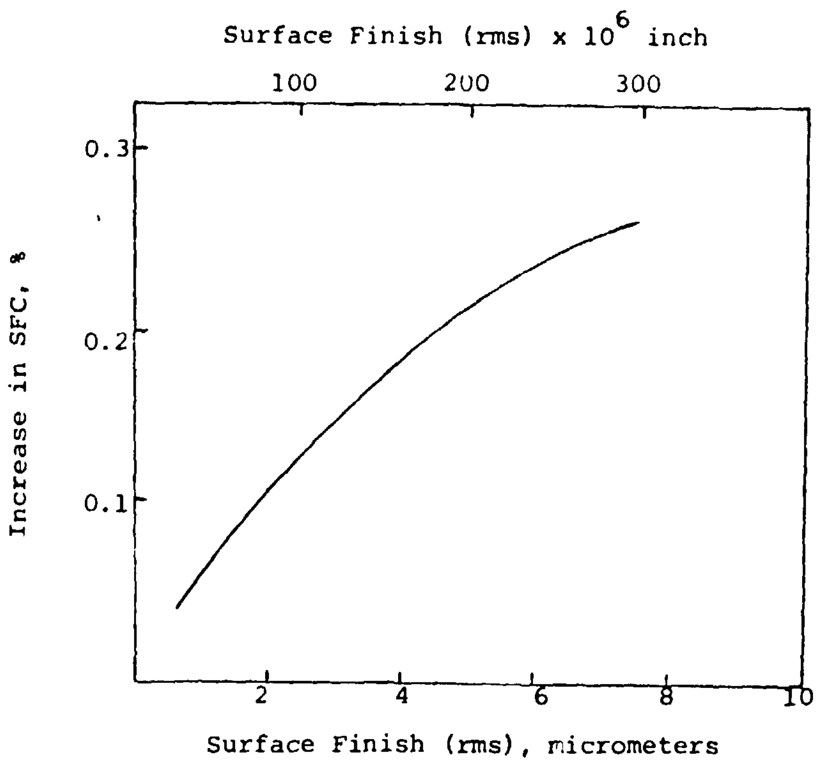

Figure 60 Effect on specific fuel consumption (SFC) of the surface finish of the CF6-50 stage 2 HPT blade.

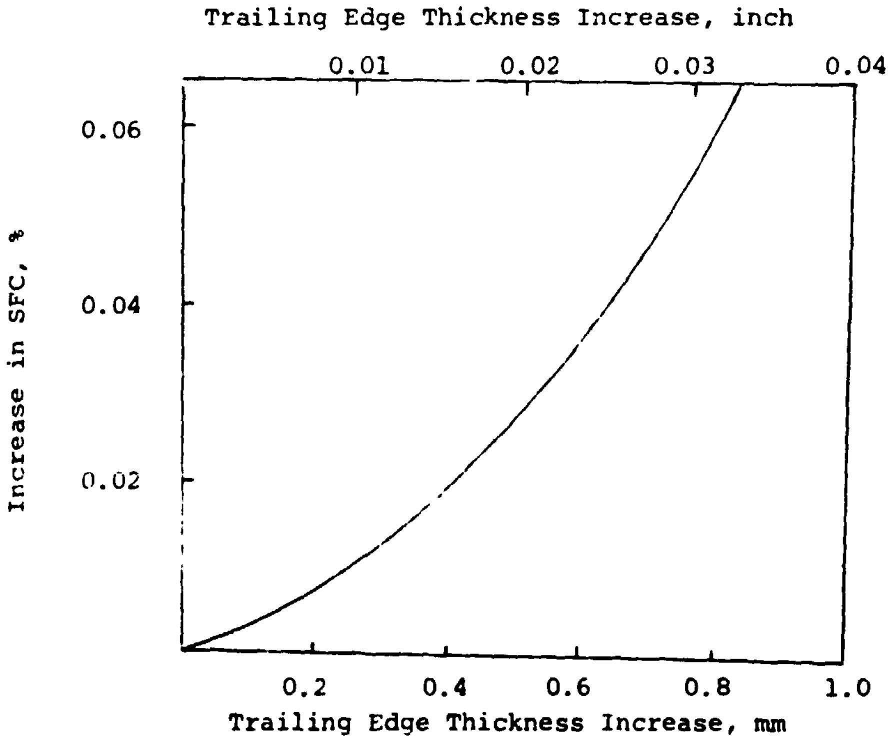

Figure 61 Effect on specific fuel consumption (SFC) of increasing the thickness of the trailing edge of the CF6-50 stage 2 HPT blade.

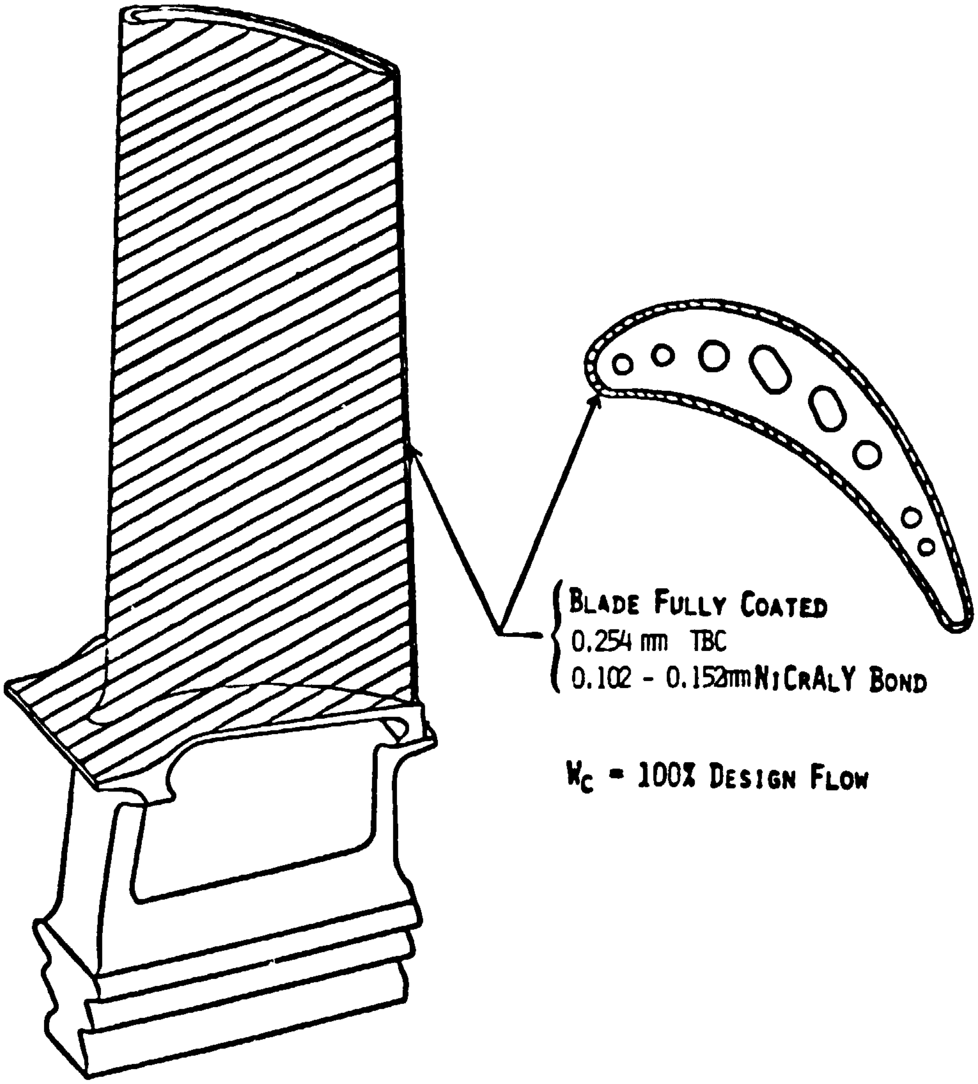

Figure 62 Recommended thermal barrier coating configuration for the engine testing of TBC'd CF6-50 stage 2 HPT blades.

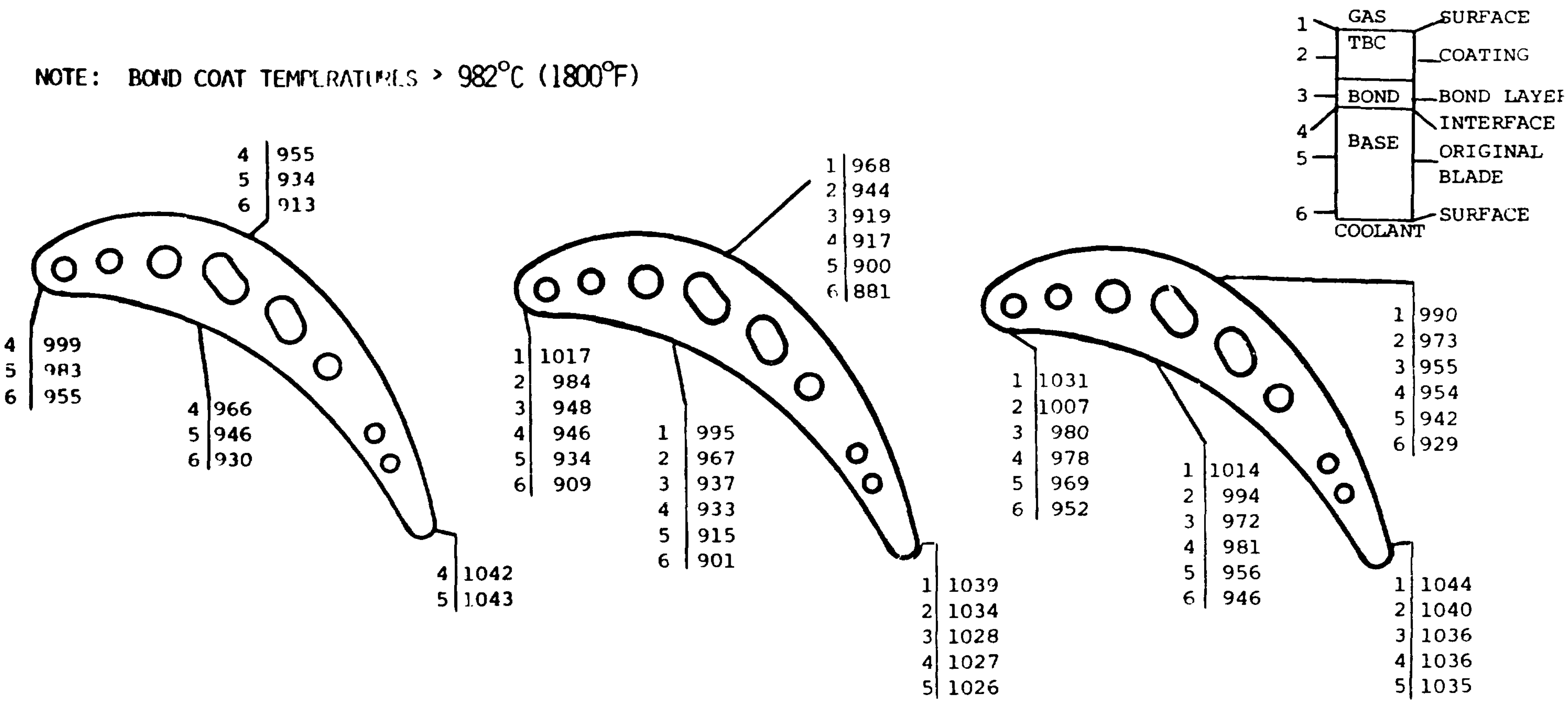

	Uncoated	Coated	Coated
Percent Coolant Flow	100%	100%	50%
Bulk Metal Temperature	951°C (1744°F)	919°C (1687°F)	955°C (1751°F)

Figure 63 Comparison of the temperature distribution for the CF6-50 stage 2 HPT blade with and without 0.25 mm (0.010 inch) TBC and with varying coolant flows.

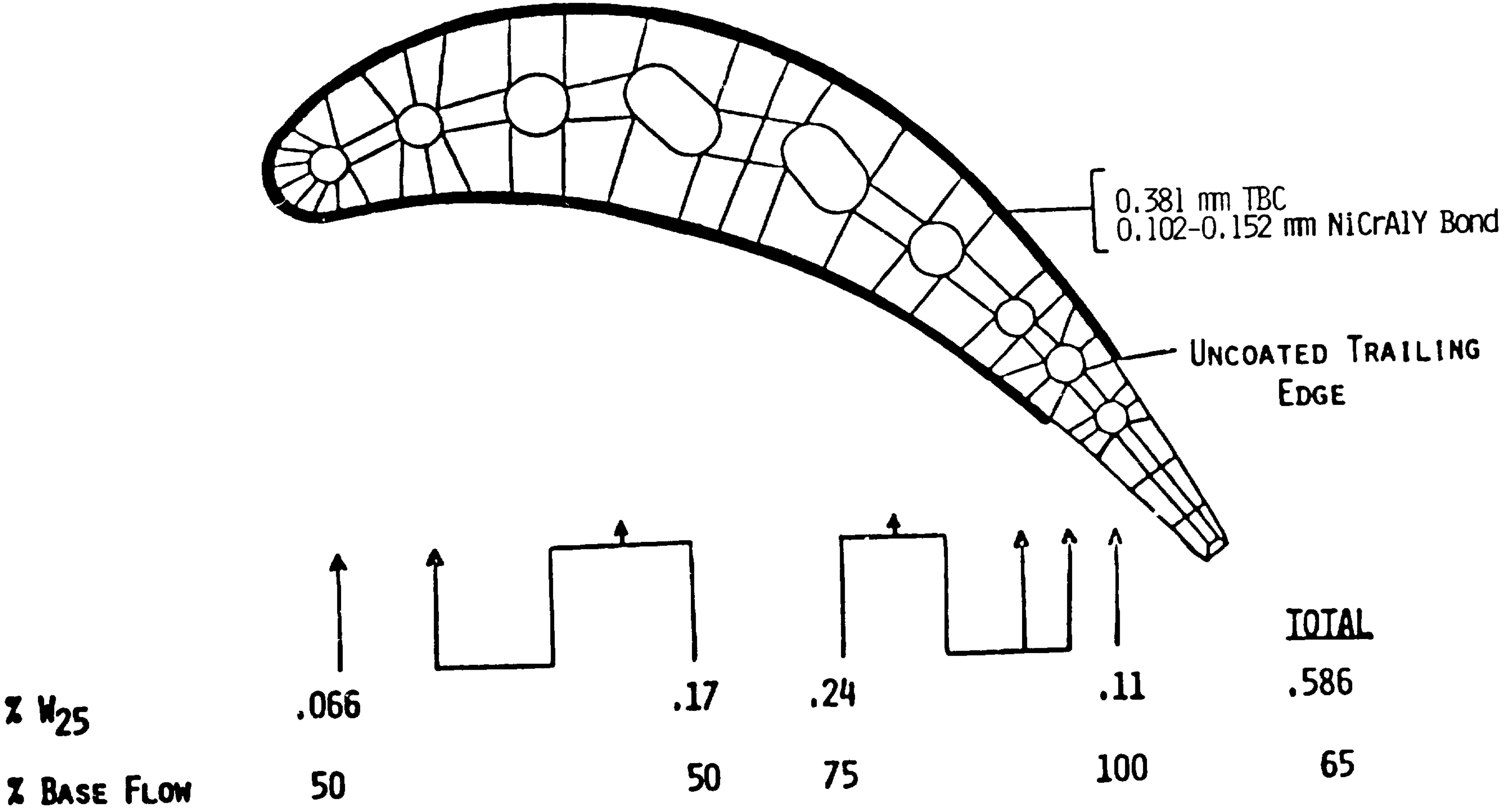

Figure 64 Study I results: Best thermal barrier coating configuration utilizing the current CF6-50 stage 2 HPT blade casting and an assumed bond coat temperature limit of 982°C (1800°F).

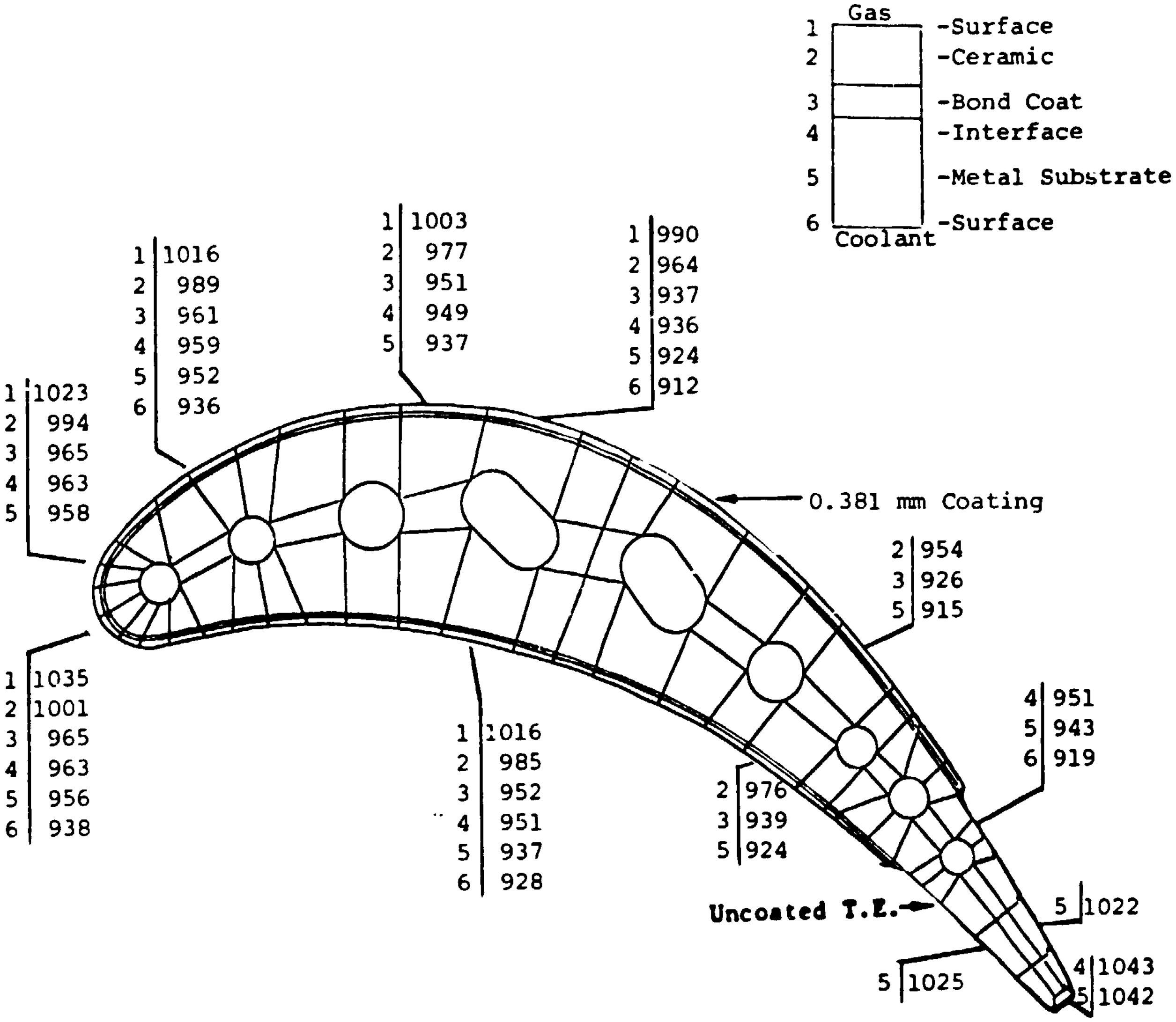

Average Temperatures
Metal - 937°C (1718°F)
Bond Coat - 944°C (1732°F)
Ceramic - 976°C (1788°F)

Figure 65 Temperature distribution for the CF6-50 stage 2 HPT blade with the TBC configuration developed in Study I but retaining production blade substrate structure.

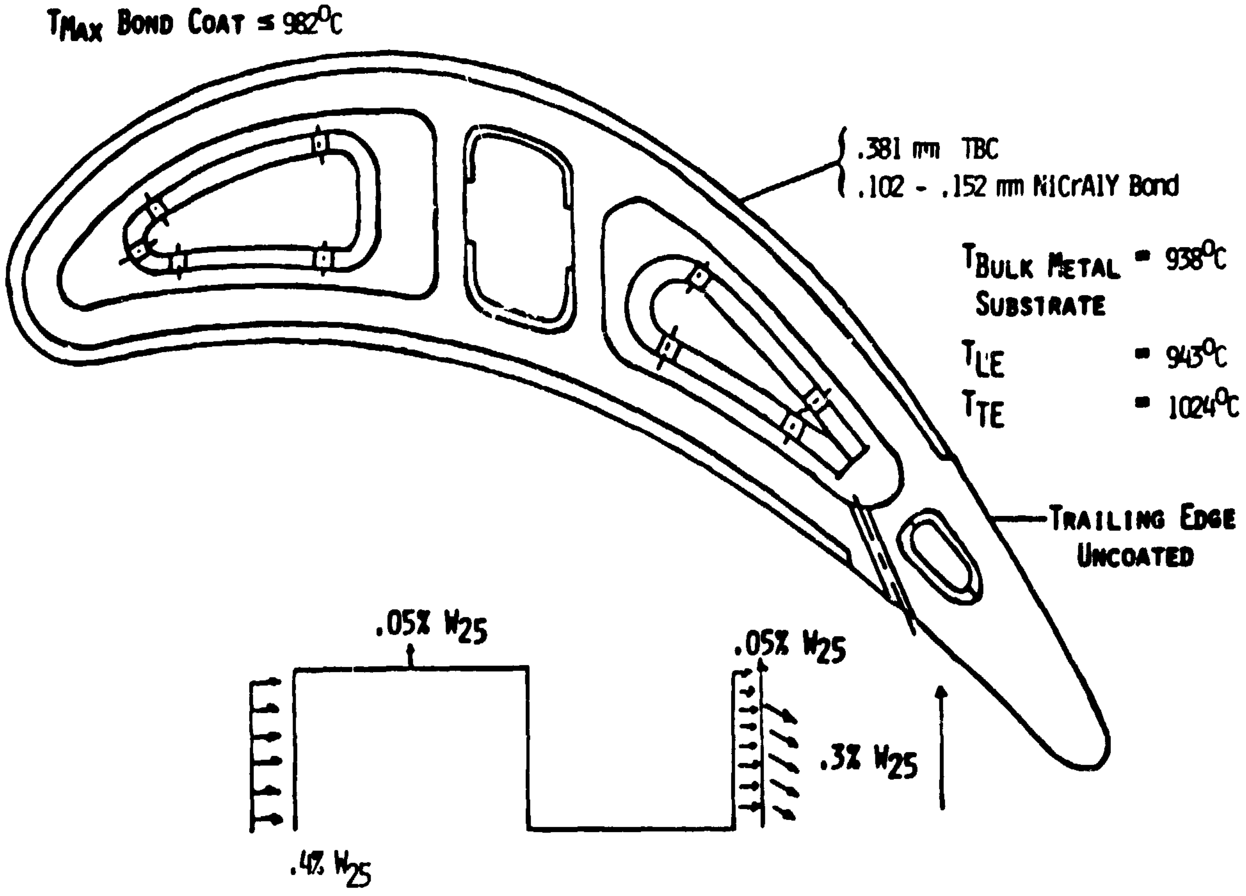

Figure 66 Advanced concept design for a thermal barrier coated CF6-50 stage 2 HPT blade developed in Study II.

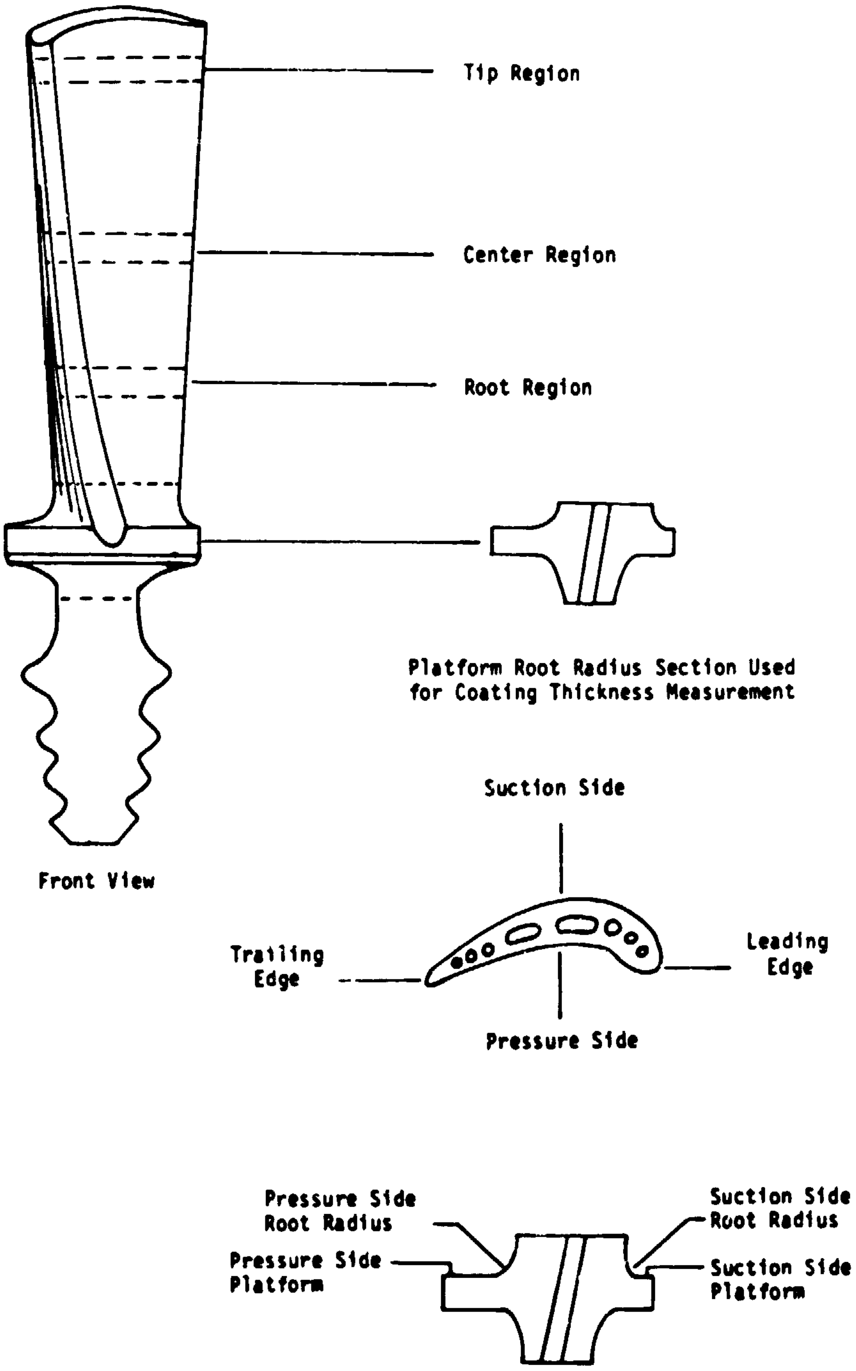

Figure 67 Diagram of blade areas cross sectioned where NiCrAlY coating thicknesses were determined.

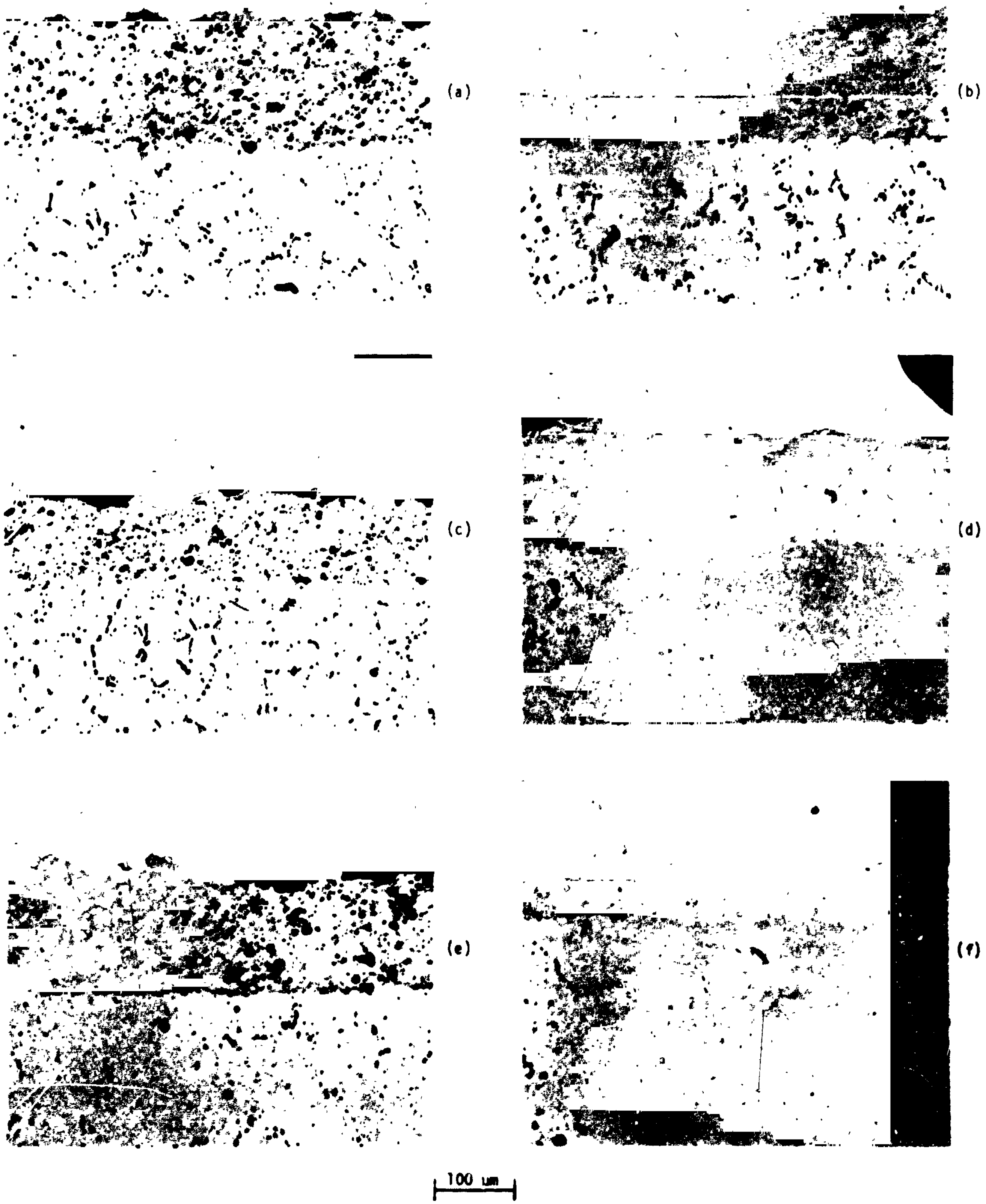

Figure 68 Photomicrographs of Ni-22Cr-10Al-1Y NiCrAlY deposited by the LP/HV process on Rene'80 CF6-50 stage 2 HPT blade. (a) Pressure side, tip cross section; (b) Suction side, tip cross section; (c) Pressure side, center cross section; (d) Suction side, center cross section; (e) Pressure side, root cross section; (f) Suction side, root cross section.

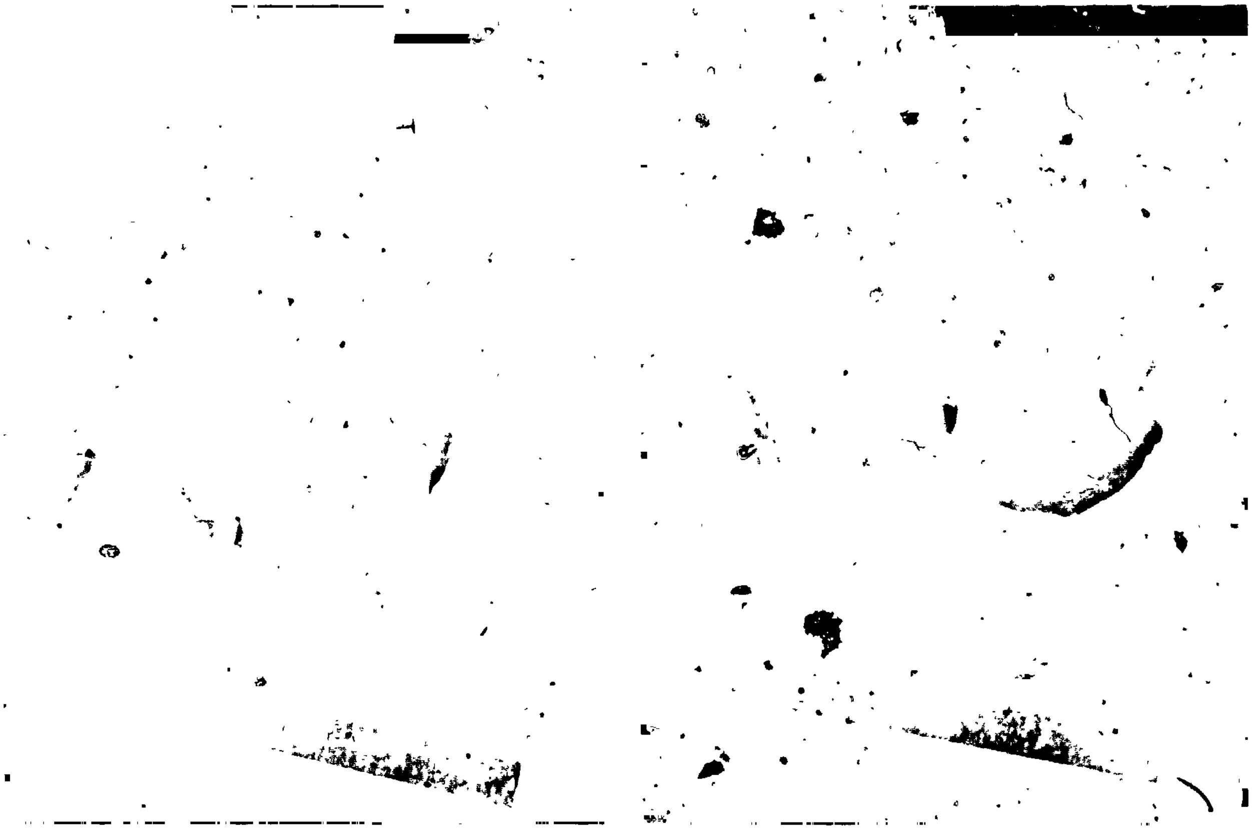

(a) (b)

Figure 69 Photograph of air sprayed Ni-22Cr-10Al-1Y NiCrAlY and air sprayed 8 w/o Y_2O_3-ZrO_2 on aluminided CF6-50 stage two blade after 168 cycles of furnace testing between 1100°C and 140°. (a) Pressure side: (b) suction side.

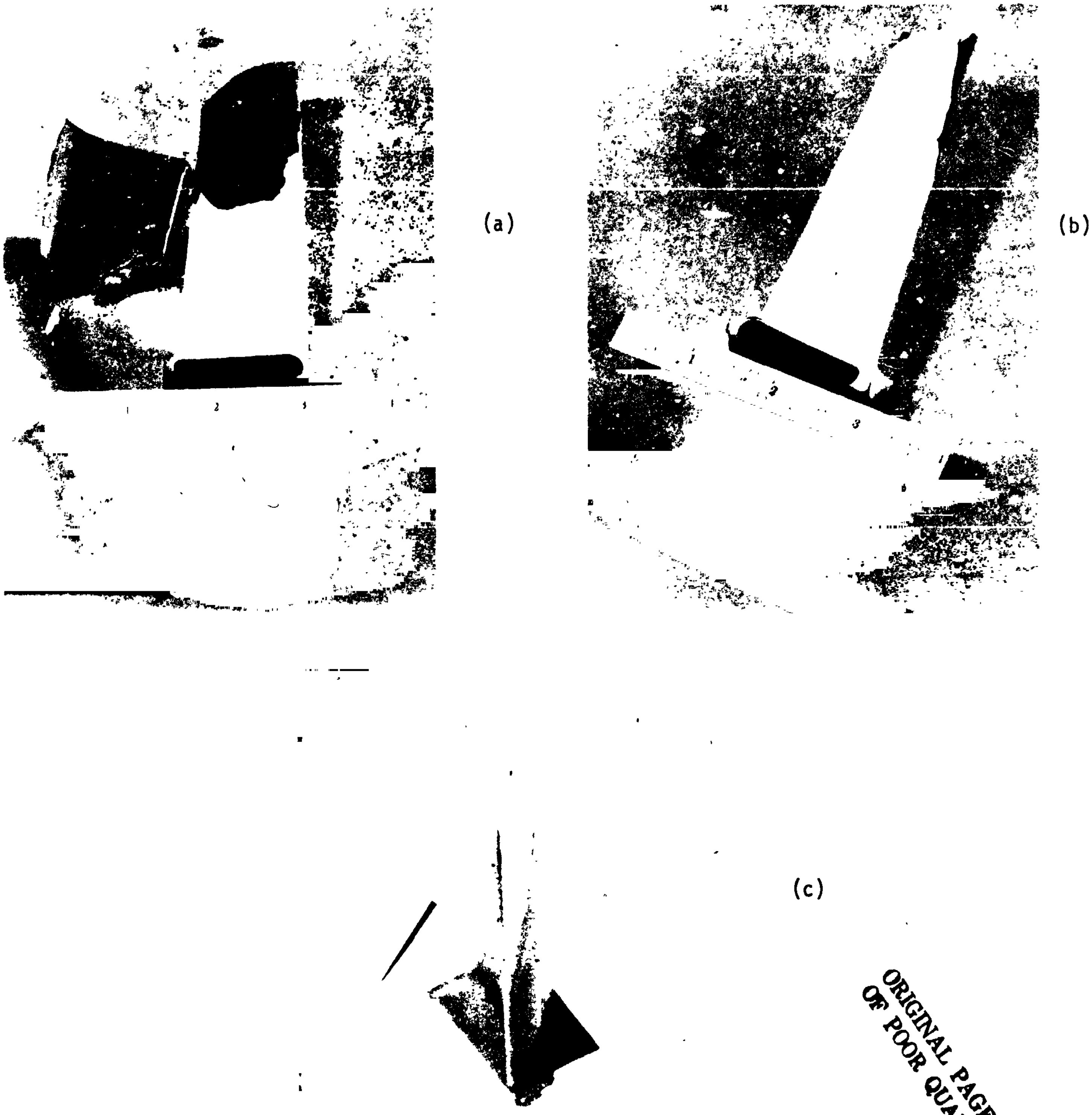

Figure 70 Photograph of air sprayed Ni-22Cr-10Al-1Y NiCrAlY and air sprayed 8 w/o Y_2O_3-ZrO_2 on aluminided CF6-50 stage two blade after 160 cycles of furnace testing between 1100°C and 140°C. (a) Suction side of No. 1 blade; (b) pressure side of No. 1 blade; (c) trailing edge view of No. 2 blade.

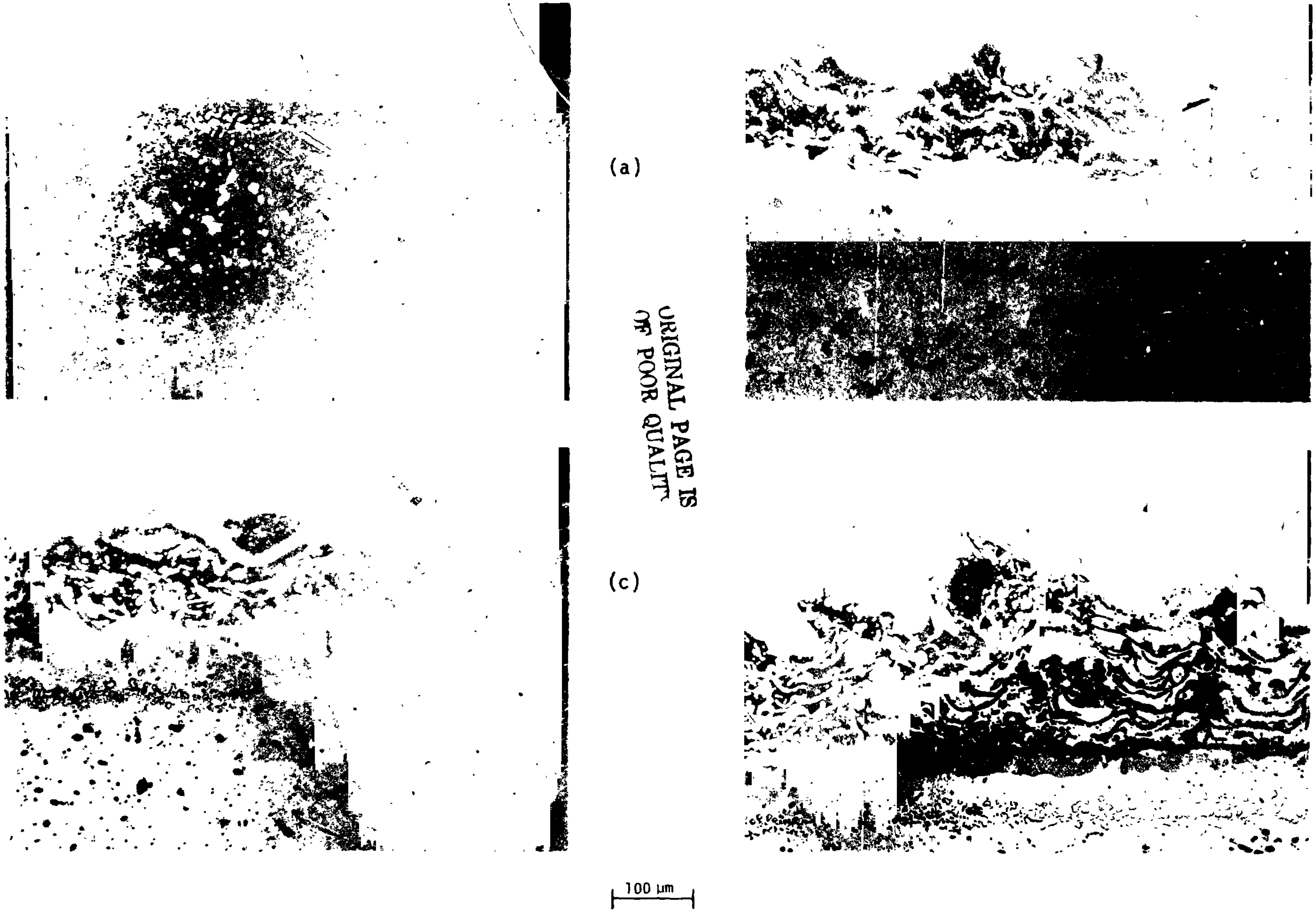

Figure 71 Optical micrographs of air sprayed Ni-22Cr-10Al-1Y NiCrAlY and air sprayed 8 w/o Y_2O_3-ZrO_2 on aluminided CF6-50 stage two blade after 168 cycles of furnace testing between 1100°C and 140°C. (a) Area of total NiCrAlY/ceramic spallation; (b) area of partial NiCrAlY spallation; (c) area where ceramic spalled

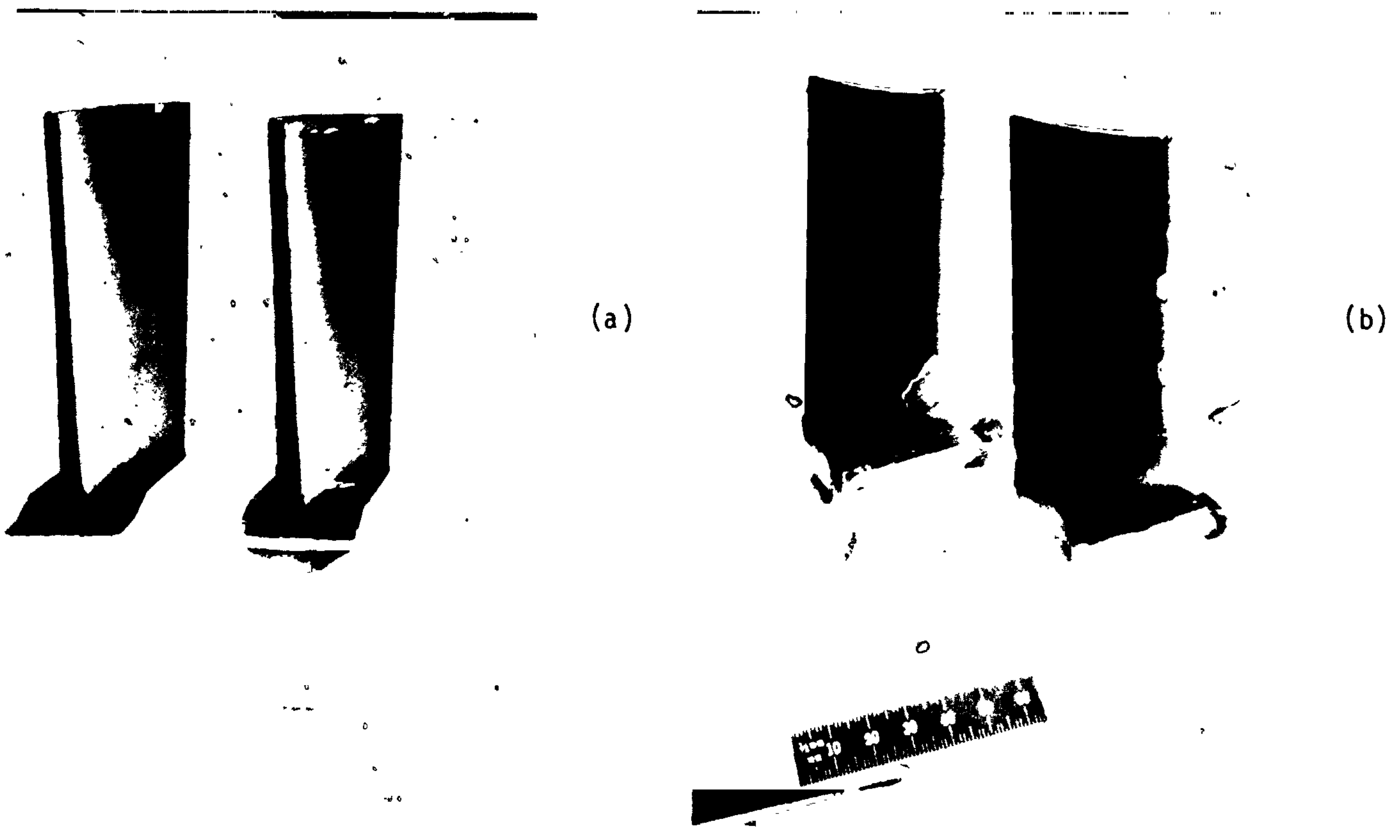

Figure 72 CF6-50 stage 2 HPT turbine blades coated with 0.13 mm Ni-22Cr-10Al-Y NiCrAlY deposited by the LP/HV process and 0.25 mm of 8 w/o Y_2O_3-ZrO_2 deposited by the air sprayed process. Right-hand blade has aluminide environmental coating between Rene'80 and NiCrAlY. Left-hand blade has no environmental coating. (a) Front view; (b) Rear view.

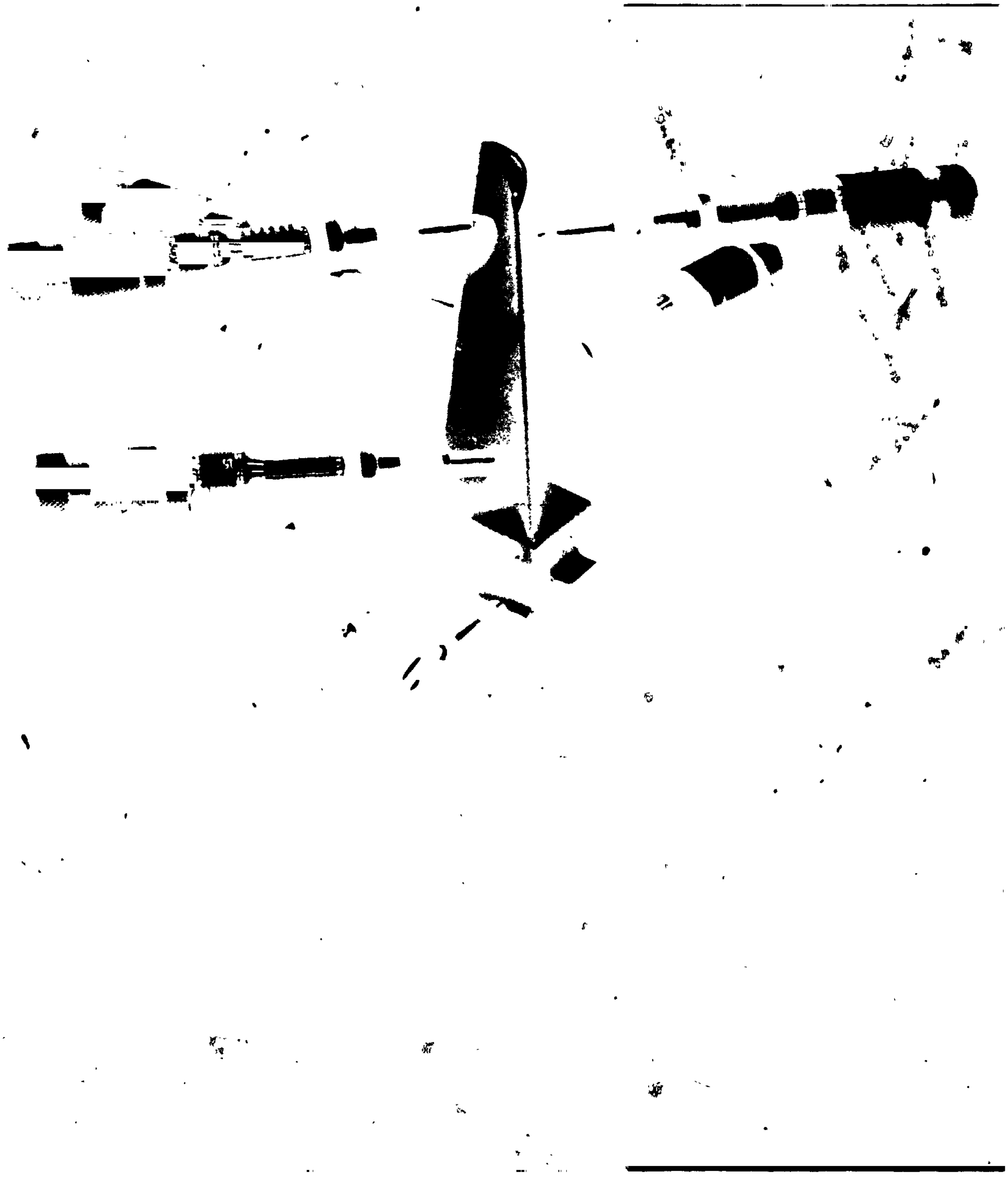

Figure 73 Micrometer array used for measuring coating thickness.

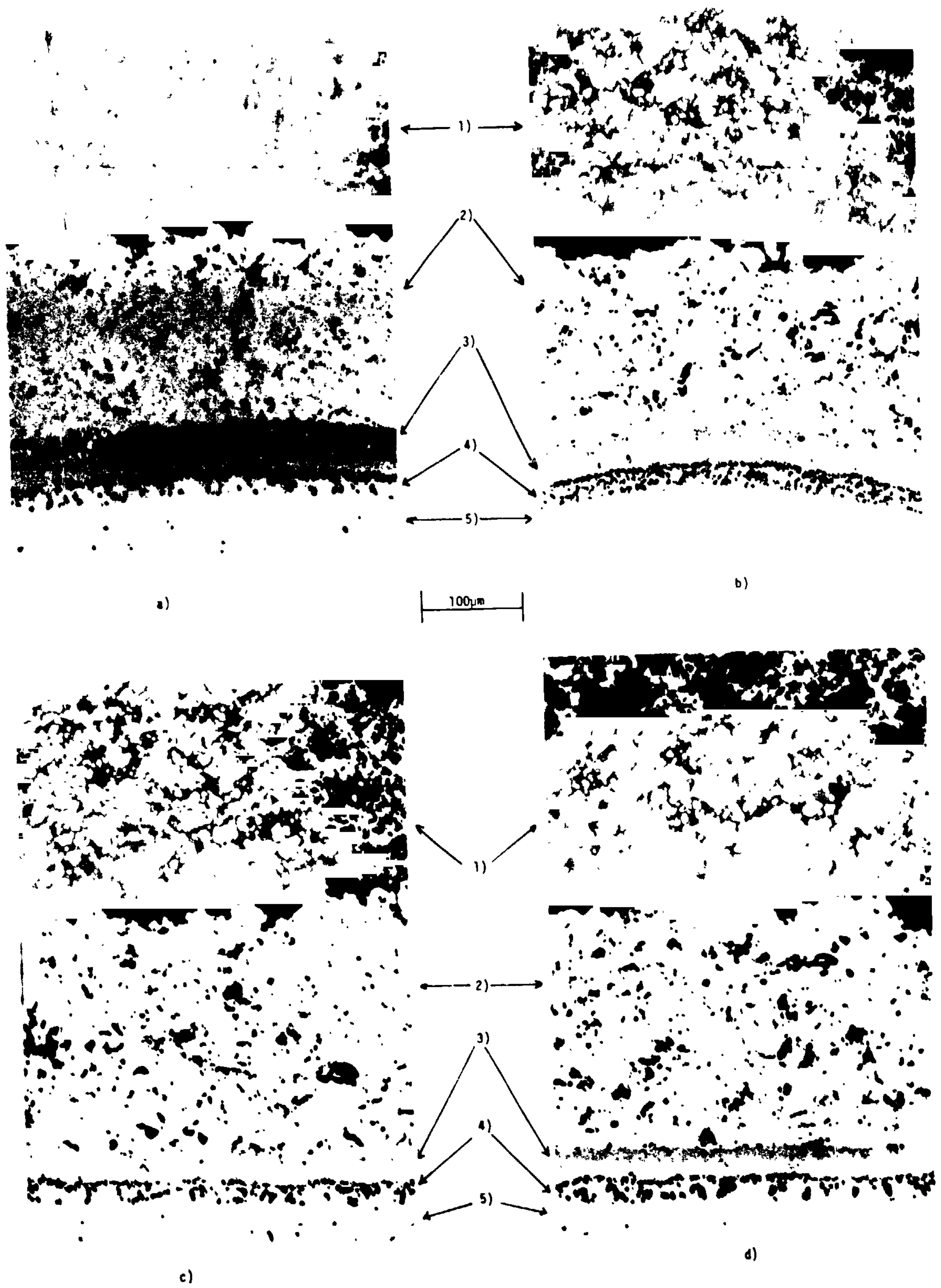

Figure 74 Micrographs of CF6-50 Stage 2 HPT blade (Serial No. L4870) near blade tip after coating with NiCrAlY and 8 w/o Y_2O_3-ZrO_2.

a)	Leading edge	1)	8 w/o Y_2O_3-ZrO_2
b)	Trailing edge	2)	Ni-22Cr-10Al-1Y NiCrAlY
c)	Pressure side	3)	Co-Dep aluminide layer
d)	Suction side	4)	Co-Dep/Rene'80 interdiffusion zo
		5)	Rene'80 blade

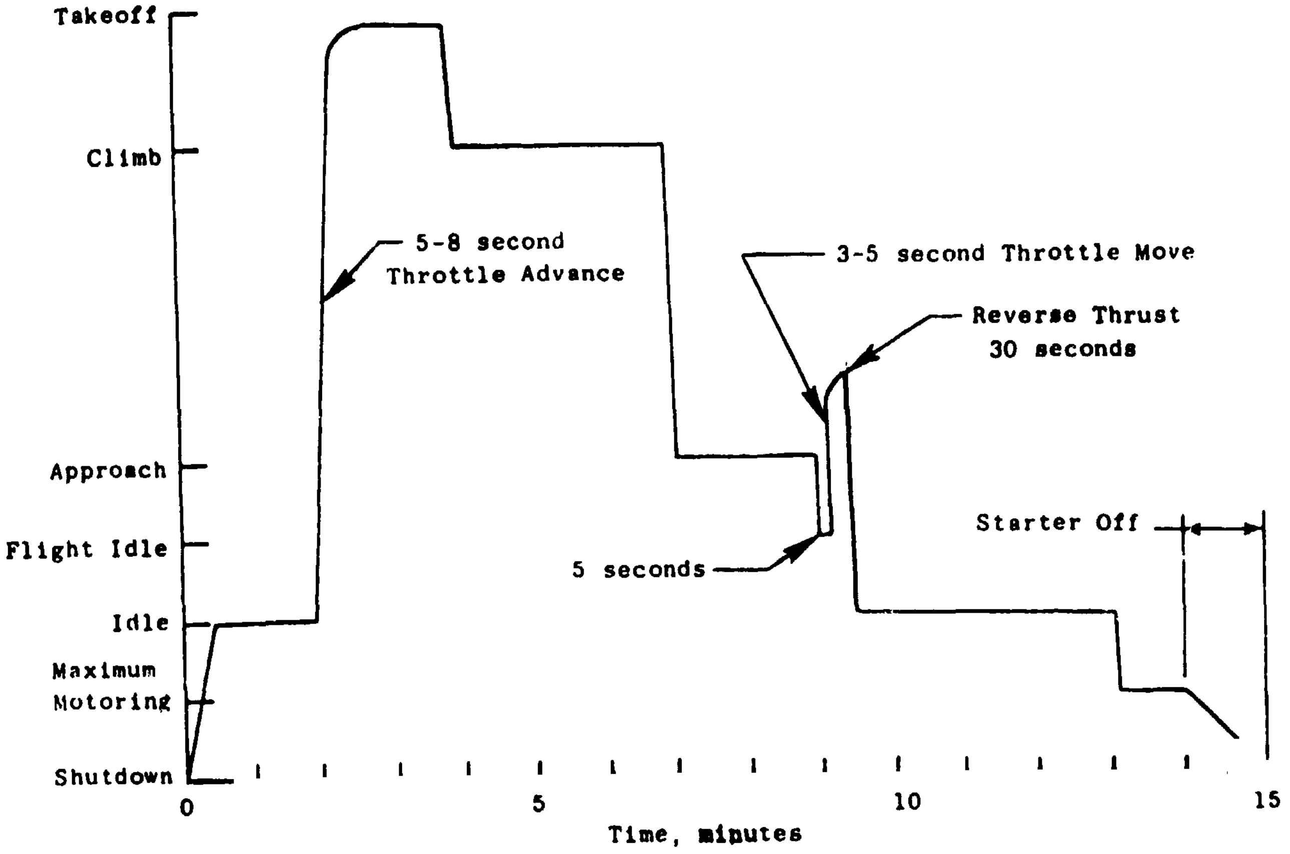

Figure 75 CF6-50 engine output versus time for endurance testing "C" cycle.

Figure 76 Photograph showing damage to leading edge of thermal barrier coated blade after 16 hours of engine check-out.

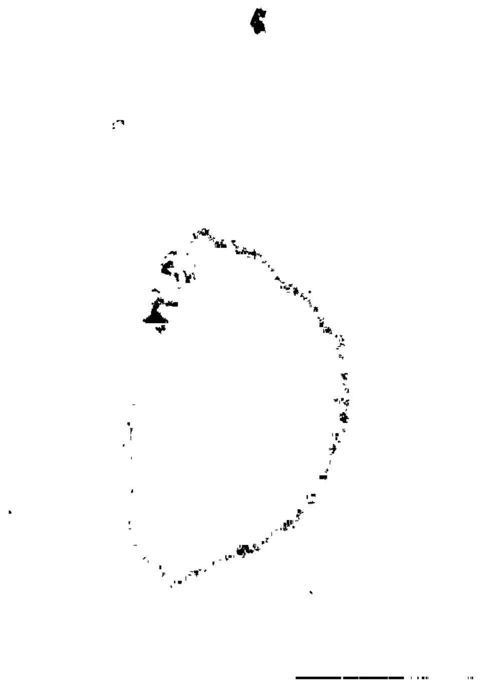

Figure 77 Photograph (taken through boroscope) showing extent of damage to leading edge of thermal barrier coated blade after 476 "C" cycles.

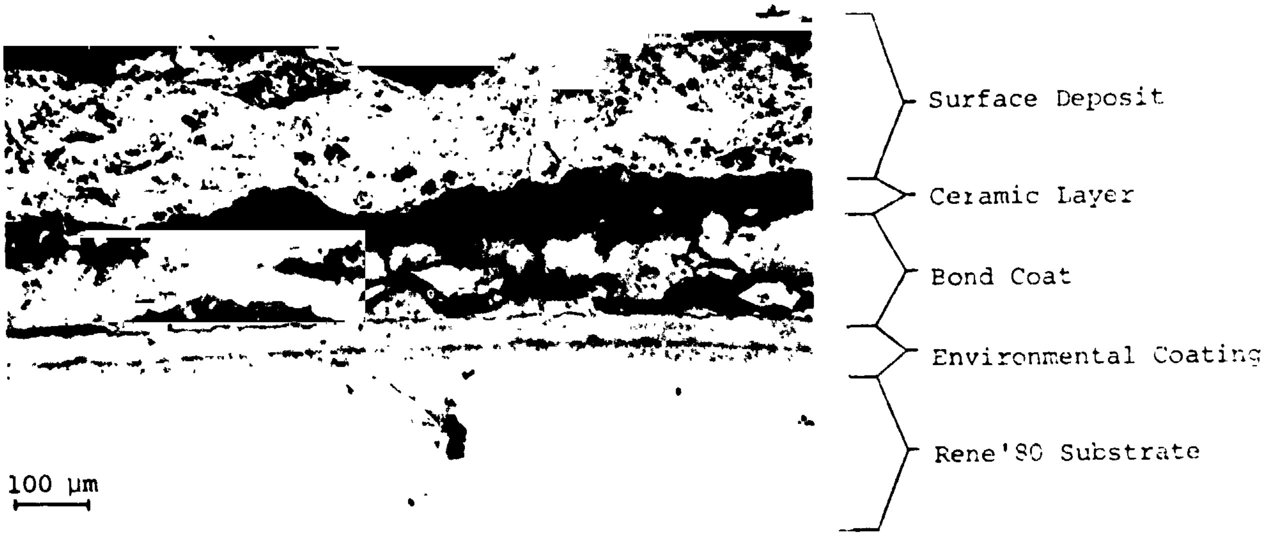

Figure 78 Engine-tested blade microstucture on the suction side near the leading edge where severe impact damage had occurred.

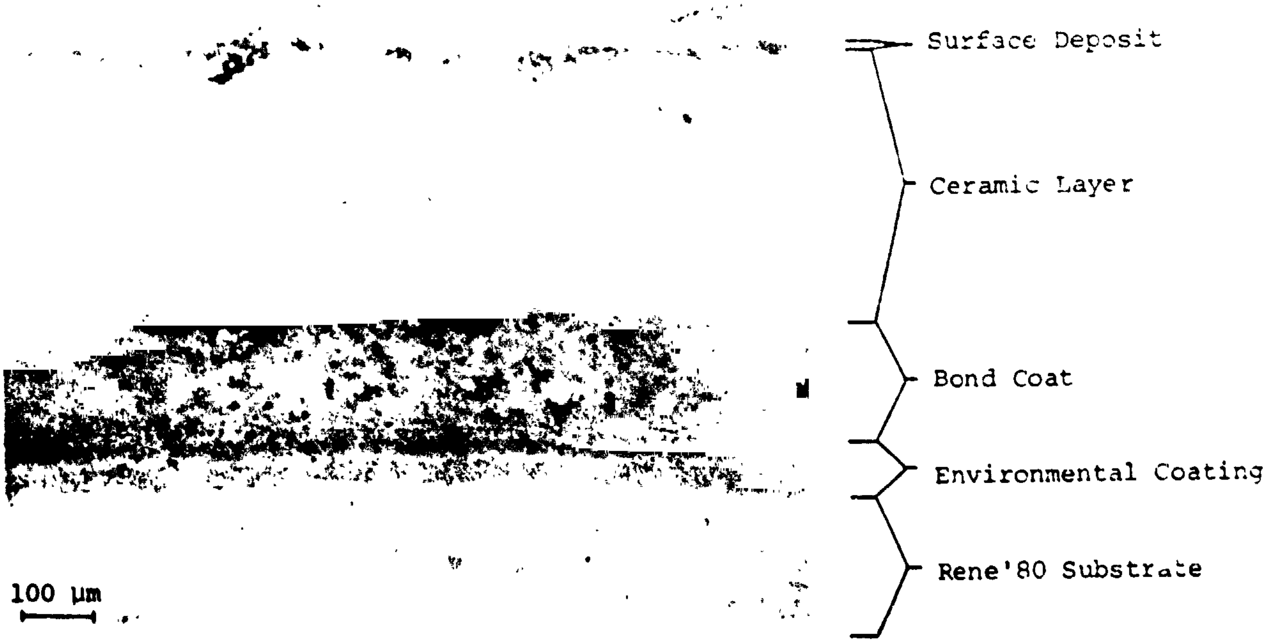

Figure 79 Engine-tested blade microstructure in the suction side mid-chord region where very little impact damage had occurred.

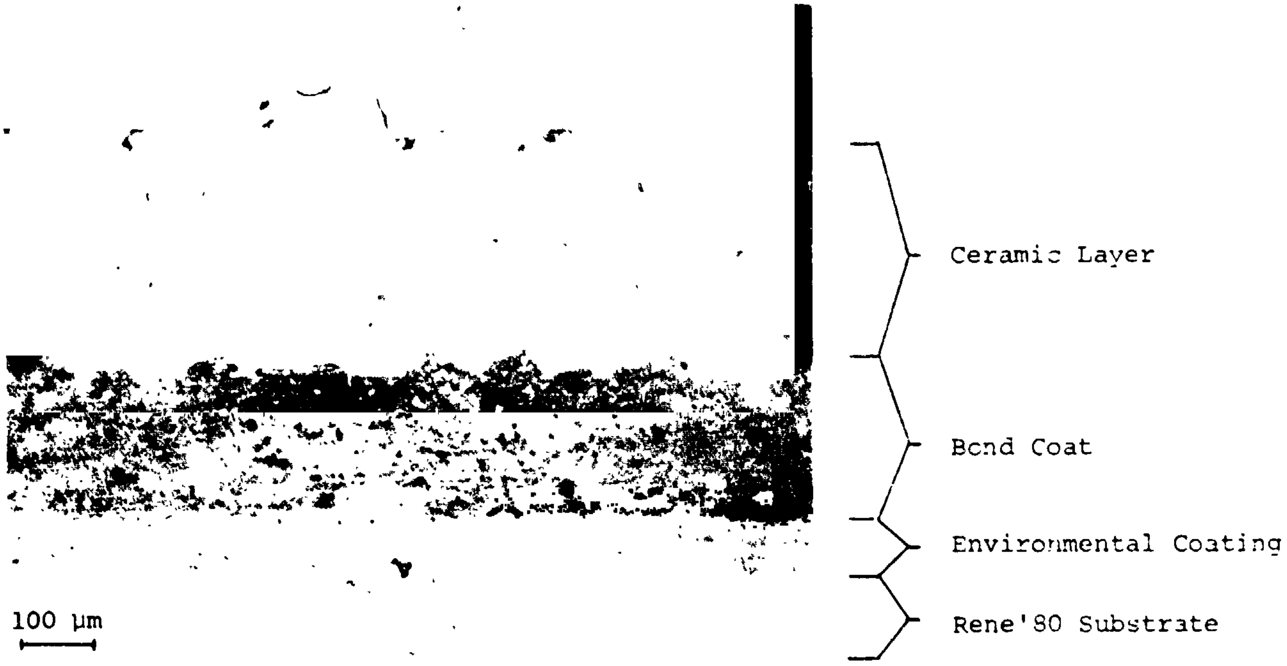

Figure 80 Engine-tested blade microstructure on the pressure side near the blade tip.